UNIVERSITY OF THE WESTERN CAPE

DOCTORAL THESIS

Test of Traditional Vibrational Wisdom by 2 proton stripping onto targets of ^{108,110}Pd, ^{114}Cd, ^{115}In

---

Author:

Bongani G. MAQABUKA

Supervisor:

Dr. Peter M. JONES

Co-supervisor:

Prof. John F. SHARPEY-SCHAFER

A thesis submitted in fulfilment of the requirements

for the degree of Doctor of Philosophy

in the

Nuclear Physics

Department of Physics

November 2018

Declaration of Authorship

I, Bongani G. MAQABUKA, declare that this thesis titled, "Test of Traditional Vibrational Wisdom by 2 proton stripping onto targets of ^{108,110}Pd,^{114}Cd,^{115}In" and the work presented in it are my own. I confirm that:

- This work was done wholly or mainly while in candidature for a research degree at this University.

- Where any part of this thesis has previously been submitted for a degree or any other qualification at this University or any other institution, this has been clearly stated.

- Where I have consulted the published work of others, this is always clearly attributed.

- Where I have quoted from the work of others, the source is always given. With the exception of such quotations, this thesis is entirely my own work.

- I have acknowledged all main sources of help.

- Where the thesis is based on work done by myself jointly with others, I have made clear exactly what was done by others and what I have contributed myself.

Signed:
_____

Date:
_____

i

"If you cannot explain it simply, you don't understand it well enough"

Albert Eistein

Abstract

The cadmium nuclei have traditionally been regarded as among the best examples of spherical vibrational nuclei. However, advances in nuclear spectroscopy have begun to detail the properties of these nuclei at the two and three vibrational phonon levels, casting doubts on the vibrational assumptions. In particular, the properties of the excited 0_n^+ (for n $\geq$ 2) levels are key to any vibrational model. Excited 0^+ states can arise in nuclei in association with the nucleon pairing degrees of freedom, and in model spaces with collective shape degrees of freedom.

This thesis reports details of the excited 0_n^+ levels in the even-even nuclei ^{110,112}Cd and ^{116}Sn, and the excited $\frac{9}{2}^+$ states in ^{117}Sb, investigated using two-proton stripping reactions. The ^{108,110}Pd(^{3}He, $n\gamma$)^{110,112}Cd, ^{114}Cd(^{3}He, $n\gamma$)^{116}Sn and ^{115}In(^{3}He, $n\gamma$)^{117}Sb reactions were investigated using AFRODITE spectrometer in conjunction with a wall of 12 plastic scintillator detectors placed 2 m away from the target chamber.

UNIVERSITY *of the*
WESTERN CAPE
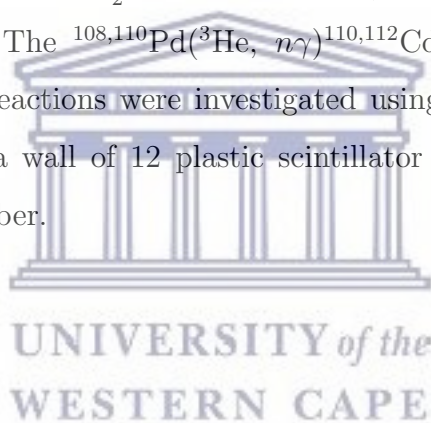
Acknowledgements

It is a great pleasure to acknowledge my sincere appreciation of Dr Pete Jones and Prof. John Sharpey-Schafer who supervised this project. I would like to thank Dr Pete Jones for his advice and guidance in the data analysis provided by his probing questions and suggestions. I am deeply indebted to Prof. John Sharpey-Schafer for the numerous invaluable discussions concerning this work, meticulously reading the manuscripts and pointing out errors therein. It was such a privilege to be under the guidance of such an experienced nuclear scientist like you. I would like to also extend a word of gratitude to iThemba LABS, who came through to help me financially in the hour of need. The financial support provided by National Research Foundation (NRF) throughout my post-graduate studies is very much appreciated.

I will always be extremely grateful to Prof. Simon Connell, who opened wide the doors of learning for us in the first group of MSONE, at UJ. For some of us, you gave a lifeline for us to re-define our life projection. A special word of thanks to my university UWC, the department of Physics; Prof. Nico Orce for the outstanding work, yearly organizing the nuclear physics taste workshops, bringing some of the best nuclear science researchers to ensure that we get the best training. Kudos to you, the underdog team coach! A special tribute goes to my schools in the rural hinterland of Eastern Cape, Mtakatye J. S. S., Lwandile J. S. S. and Nogemane High School, which moulded me into who I am today; you laid the first foundation.

Lastly, I would like to thank my family. To my late father Charles who could not live to see the fruits of his immense sacrifices. My mother, Nokhaya and my siblings, the Maqabuka and Maliwa families at large, thank you a lot for never questioning my seemingly endless pursuit of education. To my beloved wife Buntu, absolutely none of this would have been possible without your love, patience and encouragement. May the almighty God bless you all abundantly!

iv

Contents

List of Figures

List of Tables

This work is dedicated to my father **Charles Makwedinana Maqabuka** *(R.I.P.).*
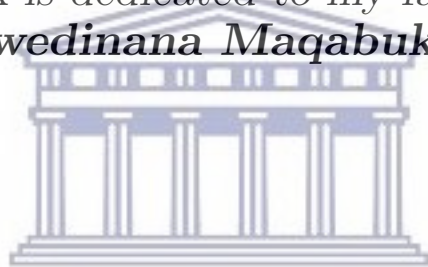
Chapter 1

INTRODUCTION

The (^{3}He, n) two-proton stripping reaction has been used to study low-spin excited states which are characterised by high proton pair correlations in their microscopic structure. Transfer reactions with light particles, investigated in high-resolution experiments, give very specific and selective information on the properties of nuclear levels. In particular, the two-proton transfer reactions are very sensitive probes for studying pairing correlations in the overlap between initial and final states. Pair correlations have been extensively studied by the two-neutron transfer (t, p) and (p, t) reactions on nuclei near closed shells, on deformed nuclei and in the transition region between spherical and deformed nuclei, using magnetic spectrometers. However, there is paucity of experimental data on two-proton stripping reactions. A few measurements, performed using the (^{3}He, n) two-proton stripping time-of-flight technique, date back to more than 30 years [2, 14–22]. Reactions where protons are stripped off the beam nucleus, so that the outgoing particle is a neutron, are difficult to do due to challenges in obtaining good neutron energy resolution. The two-proton transfer data may be integrated with those coming from other nuclear reactions, each one characterized by its specific selectivity in the population of the excited states. In these measurements, we utilize an array of high resolution ($\sim$3 keV) escape-suppressed HPGe γ ray detectors in coincidence with a wall of neutron detectors placed at forward angles to measure the strengths of two-proton pairing configurations in the $L = 0$ transfer states.

A pairing interaction is a short-range component of the nucleon-nucleon force. In even-even nuclei the strong attractive force acts on pairs of nucleons in time reversed orbits (with magnetic quantum numbers m and $-m$) to couple their angular

1

momentum to zero. The ground states of doubly even nuclei have this character and excited states with this structure may also arise, especially near a closed shell [23]. Aage Bohr proposed that the excited 0^+ states are associated with collective degrees of freedom, i.e. they have a vibrational character [24, 25]. However, some of these excited 0^+ have been established to be associated with the promotion of pairs of nucleons across major shell or sub-shell gaps to form *pairing vibrations* [26, 27]. It is believed that these extra 0^+ levels are even more deformed than those of the ground state. The pairing structure of these 0^+ states is naturally probed by two-proton, two-neutron and alpha transfer reactions.

1.1 Classical vibrating drop

A charged liquid drop model first proposed by George Gamow [28] is the simplest collective description for a nucleus; it models the nucleus as a drop of a macroscopic liquid. The resonant modes of these vibrations were first described by Lord Rayleigh [29] who determined that for a spherical incomprehensible liquid drop with radius R, the angular frequencies at which resonance occurs are given by

$$\omega^2 = \frac{\lambda(\lambda - 1)(\lambda + 2)\gamma}{\rho R^3}, \tag{1.1}$$

where λ is the mode number of frequency, γ is the surface energy per unit area due to surface tension, ρ is the density of the liquid, which is assumed to be constant throughout the drop. From equation 1.1, the frequency of a vibrating object depends on two properties, the inertial mass of the constituent particles and the restoring force, i.e. $\omega^2 \propto \frac{\gamma}{\rho R^3}$. The investigations of nuclear vibrations use much of the mathematical approach developed by Rayleigh, but, of course the oscillations are *quantized*. For a charged spherical nucleus, also assuming no viscosity and irrotational flow, the equation becomes [30]

$$\omega^2 = \frac{\lambda(\lambda - 1)(\lambda + 2)}{3} \frac{C_s}{R^2_A m_p} \frac{1}{A} - \frac{2\lambda(\lambda - 1)}{2\lambda + 1} \frac{e^2}{4\pi\epsilon_0 R^3_A m_p} \frac{Z^2}{A^2}, \tag{1.2}$$

where C_s is the surface energy term in the Weizsäcker semi-empirical mass formula ~ 18 MeV [31], $R_0 = R_A A^{\frac{1}{3}}$ is the radius of the nucleus, m_p is the mass of the proton, and A is the atomic mass number. Taking $R_A = 1.3$ fm and the excitation energy of the vibration as $E_x = \hbar\omega$ gives $E_x = 3.3$ MeV at A = 110 for quadrupole
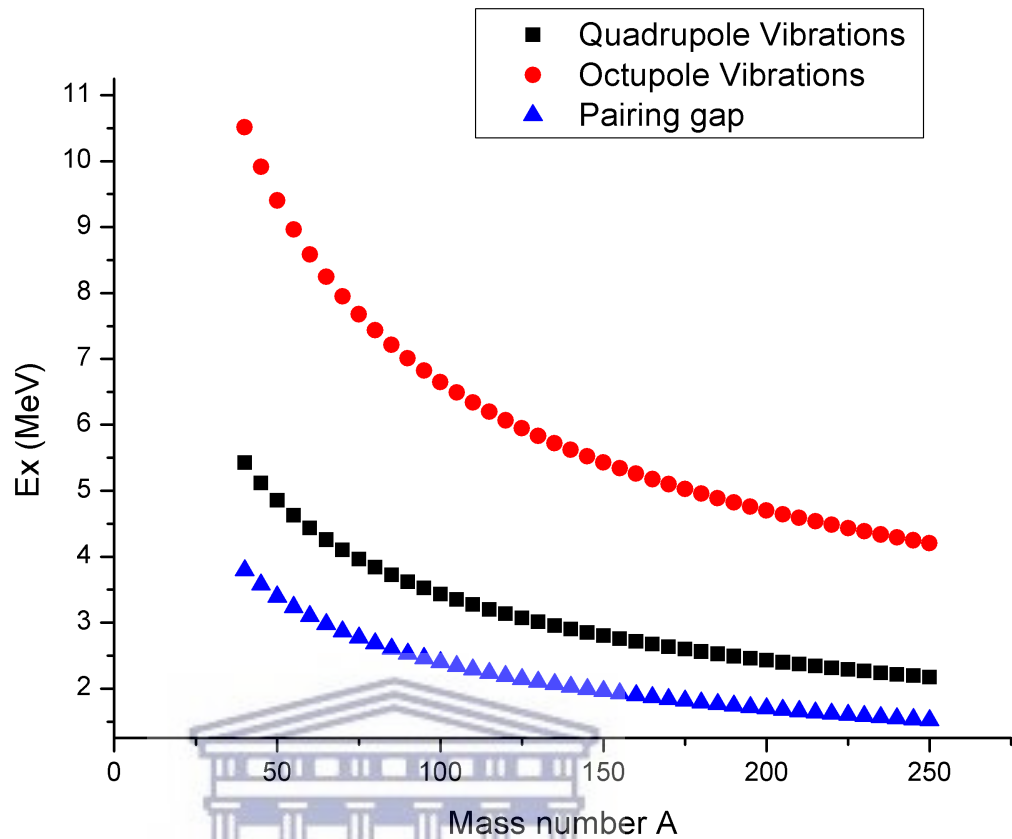
FIGURE 1.1: Plot of the Classical Vibrational energies E_x of an incompressible liquid drop assuming irrotational flow using the first term in Equation 1.2. The surface energy is taken from the Weizsäcker Mass Formula $\sim$18 MeV and it is assumed that the radius constant $R_A = 1.3$ fm. It is assumed that the energy can be quantised using $E_x = \hbar\omega$. The pairing gap is calculated using $\Delta \sim \frac{12}{\sqrt{A}}$ MeV from [1].

vibrations ($\lambda = 2$). For octupole vibrations with $\lambda = 3$, $E_x = 6.3$ MeV. The behaviour of E_x with nuclear mass number A is plotted in Fig. 1.1 for both quadrupole and octupole vibrations. The second Coulomb term in equation 1.2 is of the order of 100th of the first term and makes little contribution at all values of A. A similar calculation by Flügge can be found in [32].
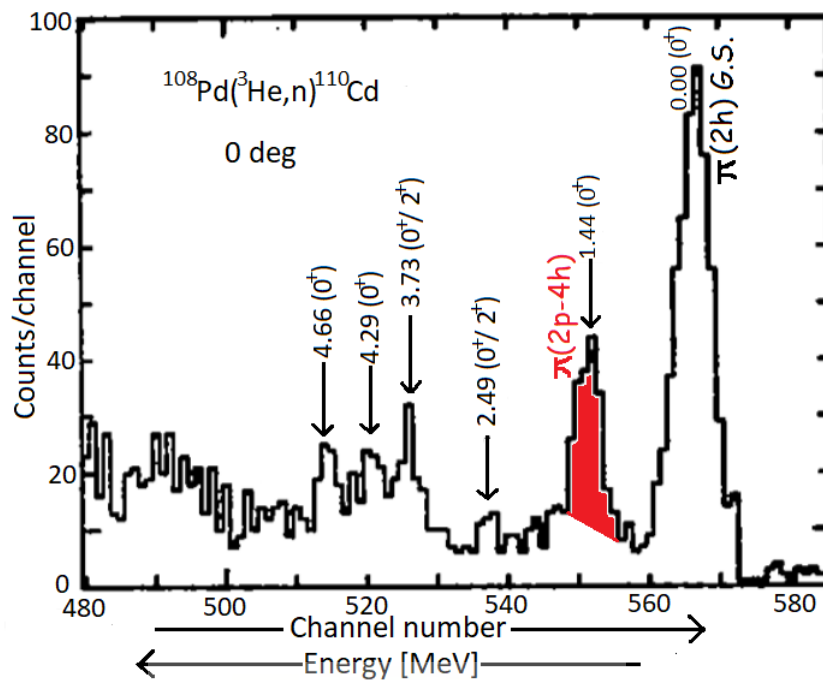
FIGURE 1.2: A time-of-flight spectrum from Fielding *et al.* [2] generated during the ^{108}Pd(^{3}He, n)^{110}Cd reaction.

1.2 Spectroscopy of 0_n^+ states in ^{110,112}Cd and ^{116}Sn

The Cd isotopes have been considered as classical examples of near harmonic vibrators [33]. The two isotopes we have studied are characterised by the presence of the expected two-phonon triplet of levels with spins 0^+, 2^+, 4^+ (the only possible vector addition of two 2^+ spins) at the requisite energy level. Similar states with spin-parity 0^+, 2^+, 4^+ that lie close in energy are also found in ^{116}Sn [13] . Previous measurements of ^{108,110}Pd(^{3}He, n)^{110,112}Cd time-of-flight experiments at a 25 MeV beam energy were done in the mid 1970s by Fielding *et al.* [2]; they used a 9 m time-of-flight baseline and could achieve a resolution of $\sim$400 keV, Fig. 1.2 & 1.3. Reported excited 0^+ states in this reference are given in Table 1.1, they are compared with excitation energies of the known 0_n^+ states. Fielding interpreted the excited states they observed in terms of pairing vibrations. In ^{116}Sn this state has been assigned to be the band head of the proton 2p-2h deformed band, see Fig. 1.4. These states are discussed in Section 1.3.

In this study, we probe these excited 0^+ states with high resolution using the (^{3}He, $n\gamma$) reaction with targets of ^{108,110}Pd and ^{114}Cd. The nuclei we are dealing with
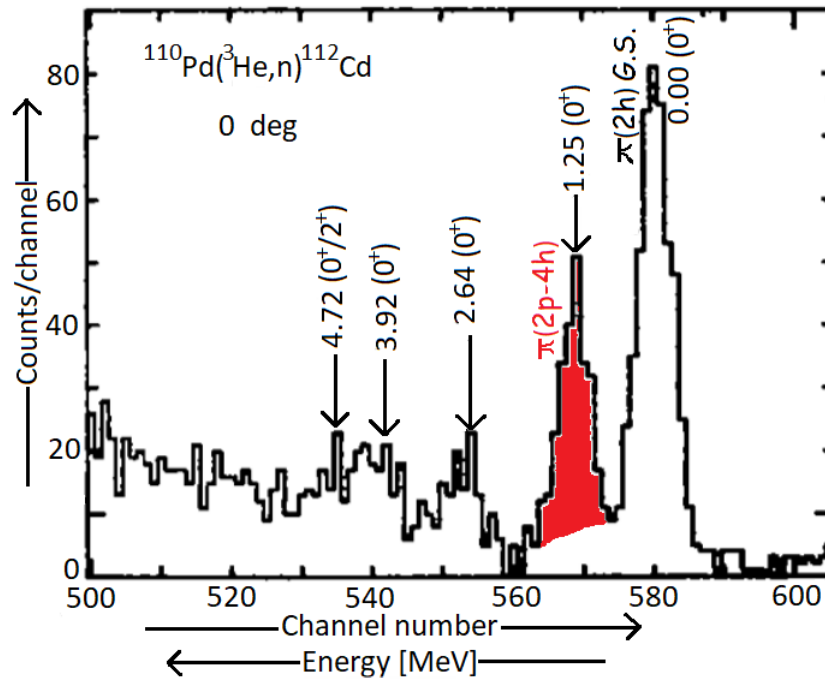
FIGURE 1.3: A time-of-flight spectrum from Fielding *et al.* [2] generated during the ^{110}Pd(^{3}He, n)^{112}Cd reaction.

have proton numbers with Z = 48 and 50. The protons are distributed in the $1g_{\frac{9}{2}}$ orbital below the Z = 50 proton closed shell for the even-even cadmium and tin isotopes. The neutron number varies from 62 to 66 (mid-shell) and the neutrons outside the N = 50 neutron shell are distributed amongst the $1g_{\frac{7}{2}}$, $2d_{\frac{5}{2}}$, $1h_{\frac{11}{2}}$, $2d_{\frac{3}{2}}$ and $3s_{\frac{1}{2}}$ shell model orbitals. Reactions like ^{108,110}Pd(^{3}He, n)^{110,112}Cd can take place by transferring the two correlated particles into orbitals with energies below the Z = 50 shell closure or by transferring both particles to empty single-particle states above the closed shell. Thus, a two-proton stripping reaction on a four-proton hole target, allows the excitation of two proton hole states, or with the latter excitation mode, you could have two-particle four-hole (2p-4h) states [34].

For the odd Z = 49 ^{117}Sb, the target nucleus ^{115}In has one proton short of the closed shell in the $1g_{\frac{9}{2}}$ orbital. It has 66 neutrons, which are distributed in similar shell orbits above the N = 50 neutron closed shell. With this proton configuration in the target, a (^{3}He, $n\gamma$) reaction populates $\frac{9}{2}^+$ states similar to the ground-state spin of the target nucleus so that the excitation of two-particle one hole (2p-1h) states is achieved, Fig. 1.5.
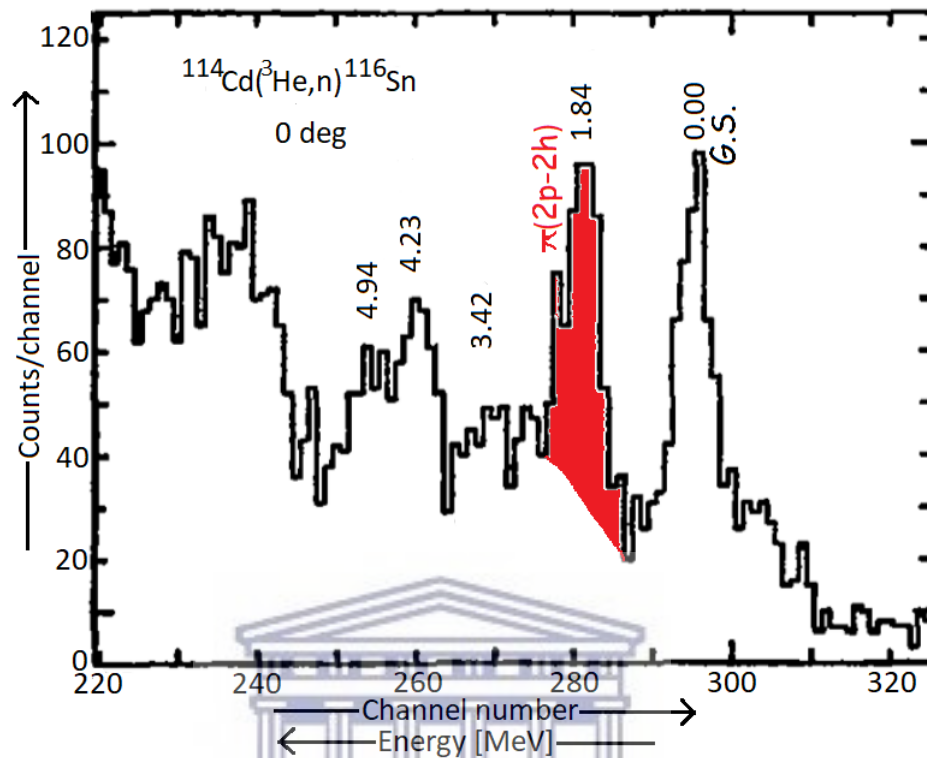
FIGURE 1.4: A time-of-flight spectrum from Fielding *et al.* [2] generated during the ^{114}Cd(^{3}He, n)^{116}Sn reaction.

TABLE 1.1: Excitation energies of 0_n^+ states in ^{110,112}Cd and ^{116}Sn. Level energies extracted from the National Nuclear Data Center (NNDC) [13] and (^{3}He, n) time-of-flight(t-o-f) data from Fielding *et al.* [2].

Excited 0^+ states	^{110}Cd Excitation (keV)	Fielding Excitation (MeV)	^{112}Cd Excitation (keV)	Fielding Excitation (MeV)	^{116}Sn Excitation (keV)	Fielding Excitation (MeV)
$0^+{}_2$	1473	1.44	1224	1.25	1756.86	1.84
$0^+{}_3$	1731		1433		2027.48	
$0^+{}_4$	2079		1871		2545.71	
$0^+{}_5$	2332	2.49	2301		2790.55	
$0^+{}_6$	2662		2650	2.64	3194.32	
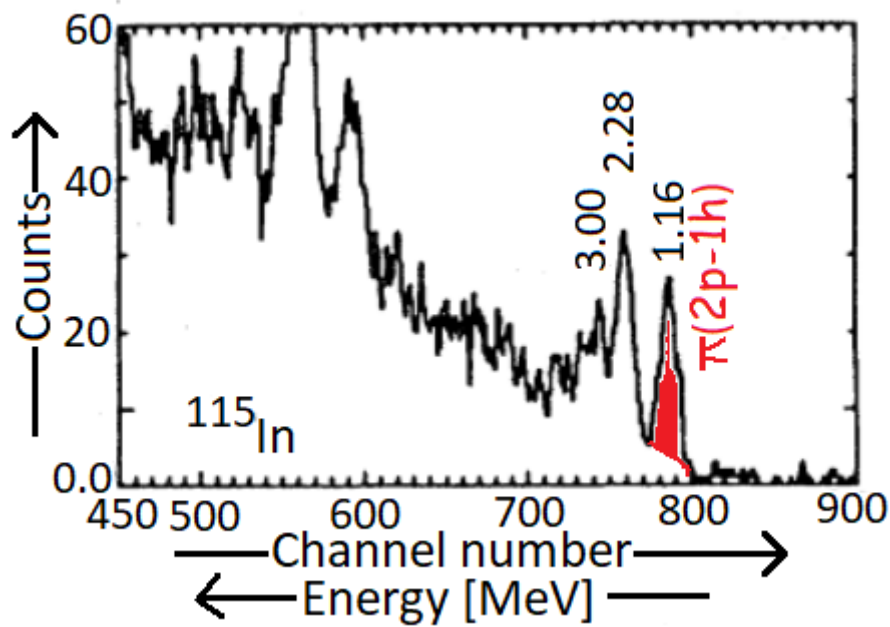
FIGURE 1.5: A time-of-flight spectrum from Alford *et al.* [3] generated during the ^{115}In(^{3}He, n)^{117}Sb reaction.

1.3 Known structures in ^{110,112}Cd, ^{116}Sn and ^{117}Sb

Nuclei adjacent to closed shells such as Z = 50, have been conventionally viewed as spherical and soft, and as such the first excited 0_2^+ states in such nuclei are regarded as two-phonon quadrupole vibration excitations [35]. However, with some nuclei the first excited 0^+ state is a deformed intruder state, while the second excited 0_3^+ state is the two-phonon state [35]. The *intruder* mechanism (further discussed in the next Chapter) in these nuclei is thought to be due to the interaction between the protons involved in particle-hole excitations across the Z = 50 shell gap and neutrons occupying the N = 50-82 shell [36, 37]. Intruder states are a common phenomenon in regions where one kind of nucleon is near a closed shell and the other is at a midshell. The intruder bands are almost certainly of rotational character having deformations larger than those of the ground states. The 0^+ band heads have a parabolic excitation as a function of neutron number and reach a minimum near the midshell. These characteristic features across the isotope chain of these nuclei have been used as evidence for the interpretation of these bands as intruder-bands.
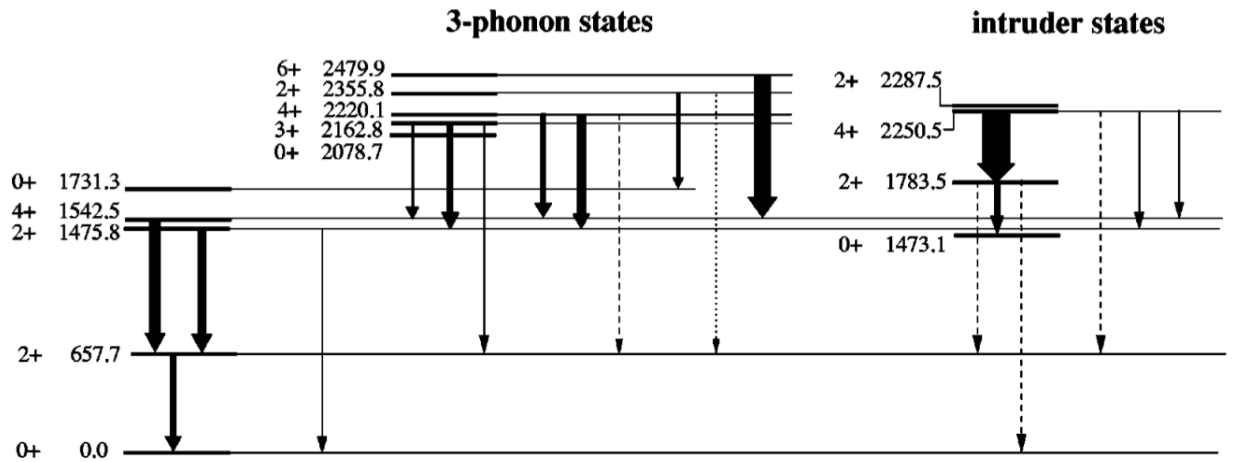
FIGURE 1.6: Low-lying levels in even-even ^{110}Cd isotope. On the right are the intruder states. The widths of the arrows are proportional to the reduced transition probabilities [4].

1.3.1 Excited 0^+ states in ^{110,112}Cd isotopes

The presence of low-lying intruder states in the Cd isotopes has been clearly demonstrated and their nature is reasonably well understood [38–42]. In ^{110}Cd, the excited $0_2{}^+$ state at 1473.1 keV is well established as the π(2p-4h) band head of the intruder band with the rotational band members 1783.5 keV 2^+ member, a 2250.5 keV 4^+ member and a 2877.0 keV 6^+ member [38, 39], see Fig. 1.6. The corresponding rotational intruder band members 0^+, 2^+, 4^+ and 6^+ in ^{112}Cd are at 1224, 1469, 1871 and 2571 keV, respectively [43–45]. Garrett *et al.* in [42] have identified $0_4{}^+$ as another possible candidate state of 4p-6h intruder band head and that its rotational band would be even more deformed than the 2p-4h excitation. These $0_4{}^+$ states display a decreasing excitation energy pattern as you increase the neutron number. Also, the reassignment of this $0_4{}^+$ level from a member of the three-phonon quintuplet to an intruder state is strengthened by the apparent lack of any transitions to the two-phonon states. The $0_4{}^+$ state has been identified at 2079 keV for ^{110}Cd, and at 1872 keV for ^{112}Cd.

1.3.2 Excited 0^+ states in ^{116}Sn

In ^{116}Sn the first excited $0_2{}^+$ state at 1757 keV has been identified as the proton 2p-2h intruder band head [5]. The properties of this state have been studied and are well established by [46–48]. The ^{116}Sn nucleus at the Z = 50 closed proton
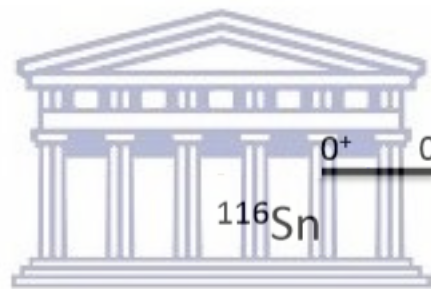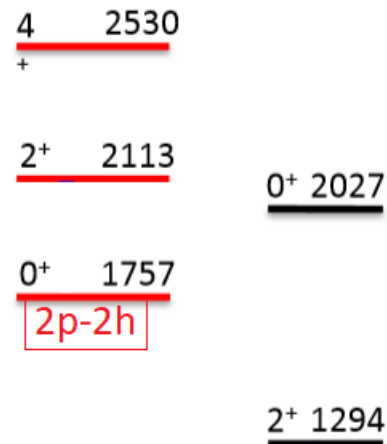
FIGURE 1.7: Spherical ground state and coexisting intruder states in ^{116}Sn [5].

shell, is exactly in the middle of the neutron shell halfway between the doubly magic ^{100}Sn and ^{132}Sn. This proton shell closure keeps the lowest energy levels in these nuclei spherical. But as soon as the proton closed shell is broken by the proton pair excitation, the neutron orbitals drive the nuclei to become deformed. Figure 1.7 shows the intruder band in ^{116}Sn, which closely resembles the level spacings of the ground state bands in the neighbouring isotones ^{112}Pd having four proton holes and ^{120}Xe four protons away from the Z = 50 shell closer. In a sense you have four valence protons interacting with the N = 66 neutrons.

1.3.3   Excited $\frac{9}{2}^{+}$ states in ^{117}Sb

The ^{117}Sb nucleus, has one proton beyond the Z = 50 closed proton shell and lies at the N = 66 neutron midshell is a particularly interesting nucleus to study. Table 1.2 shows excitation levels of the $\frac{9}{2}^{+}$ states taken from the NNDC. These

TABLE 1.2: Excitation energies of $\frac{9}{2}^+$ states in ^{117}Sb. Level energies have been obtained from the National Nuclear Data Center [13] and the (^{3}He, n) time-of-flight(t-o-f) data from Alford *et al.* [3].

Excited $\frac{9}{2}^+$ states	^{117}Sb Excitation (keV)	Alford Excitation (MeV)
$\frac{9}{2}^+_{\ 1}$	1160	1.16
$\frac{9}{2}^+_{\ 2}$	1311	
$\frac{9}{2}^+_{\ 3}$	1488	
$\frac{9}{2}^+_{\ 4}$	1537	
$\frac{9}{2}^+_{\ 5}$	1761	
$\frac{9}{2}^+_{\ 6}$		2.28
$\frac{9}{2}^+_{\ 7}$		3.00
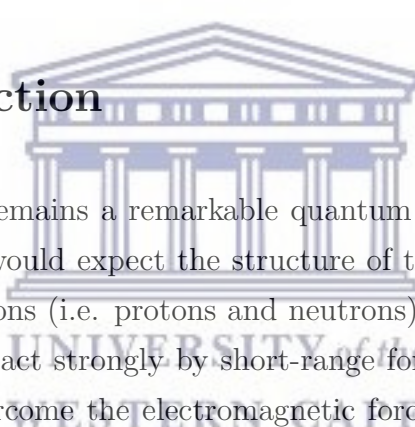
are compared with the (^{3}He, n) time-of-flight measurement taken from Alford and his co-workers [3]. The lowest excited $\frac{9}{2}^+$ is at 1160 keV, and has also been populated in the (^{3}He, n) time-of-flight data of Alford *et al.*. It is a deformed 2p-1h $[(\pi g_{\frac{7}{2}})^2 \otimes (\pi g_{\frac{9}{2}})^{-1}]$ band head. This $\Delta I = 1$ band is formed when one of the low-lying single-proton orbitals, $\pi g_{\frac{7}{2}}$, $\pi d_{\frac{5}{2}}$, $\pi h_{\frac{11}{2}}$, is coupled to phonon excitations of the $_{50}$Sn core [49, 50]. The next excited $\frac{9}{2}^+$ states at 1311 and 1488 keV are from the decay of $\Delta I = 2$ rotational bands. These bands are formed by coupling single proton states with the 2p-2h 0_2^+ states $[(\pi g_{\frac{7}{2}})^2 \otimes (\pi g_{\frac{9}{2}})^{-2}]$. These states are expected (for weak coupling) to be roughly equal to the excited states of the neighbouring even Sn nuclei. In the time-of-flight data of Alford *et al.*, the excited states at 2.28 and 3.00 MeV cannot be found in the NNDC tables.

Following this introduction, Chapter 2 describes the theoretical models which lay out the theoretical framework used in the description of vibrational structures for the ^{110,112}Cd, ^{116}Sn and ^{117}Sb nuclei. Chapter 3 describes the technical details of the four experiments carried out in this campaign. Data analysis and results are given in Chapter 4. Discussion of the results and conclusions are given in Chapter 5 and 6, respectively. The contents of Chapters 2 and 3 represents a compilation of knowledge from text books and prior publications by others. The author has no intention to claim these contents as his own ideas or his own work. These Chapters are given to provide the reader with the theoretical background based on which the present experimental results have been interpreted.

Chapter 2

THEORETICAL MODELS AND NUCLEAR STRUCTURE

2.1   Introduction

The atomic nucleus remains a remarkable quantum system, displaying a myriad of phenomena. One would expect the structure of the nucleus to be chaotic and disorderly. The nucleons (i.e. protons and neutrons) inside a nucleus are close to one another and interact strongly by short-range forces; a nuclear force which is strong enough to overcome the electromagnetic force between the protons. One of the important features of the nuclear force is that, it is *charge symmetric* and, more generally, *charge independent*. A nuclear model attempts to deliberately simplify our study of the system and focus on particular features of the system. For any theoretical model to be useful it must not only explain previously observed phenomena, but should also be predictive and provide insights into the system.

Nuclear models generally can be divided into two main extreme and opposite streams: these are the independent particle models (e.g. a spherical *shell* model) in which the nucleons are assumed, in the lowest order, to move nearly independently in a common nuclear potential created by an ensemble of nucleons, and the other, the strong interaction models in which the nucleons are strongly coupled to each other e.g. a *collective* model. Both of these, of course, have many variants. The shell model is most successful in light nuclei and nuclei near magic numbers, and the collective model for nuclei far removed from shell closures, see Fig. 2.1.

11
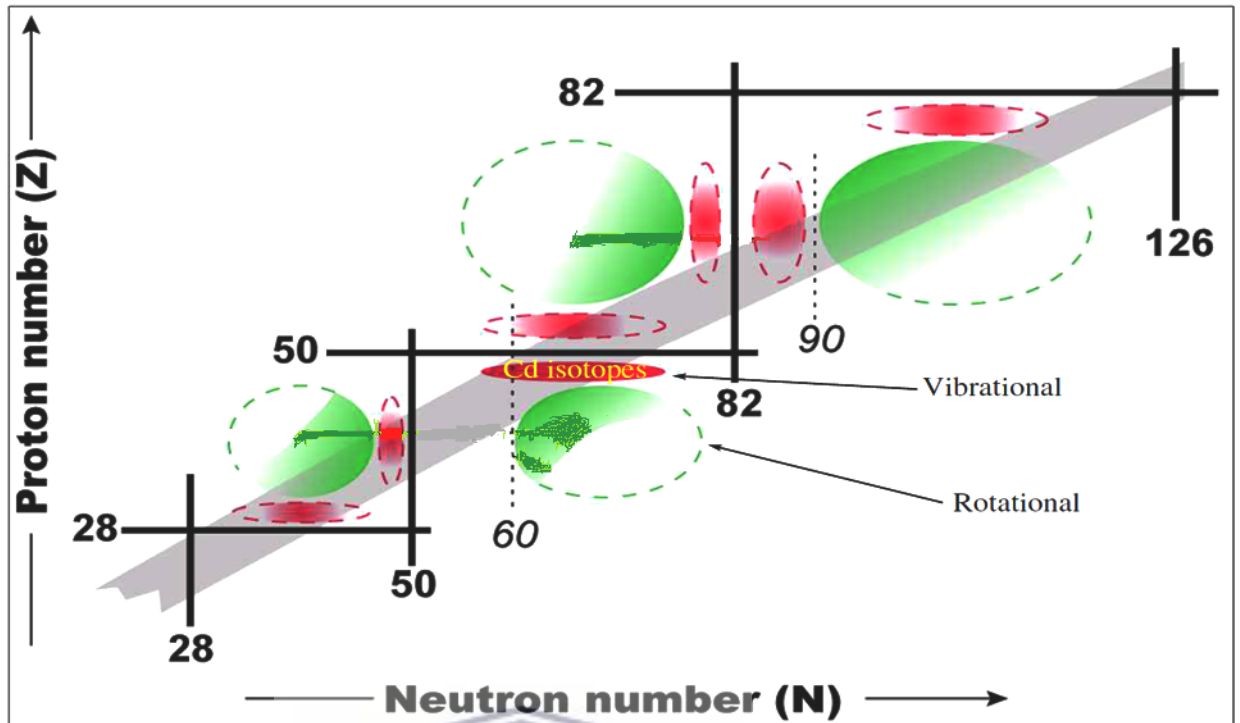
FIGURE 2.1: Collectivity in nuclear landscape.

2.2 The Nuclear Shell Model

The shell model is one of the most successful models in nuclear physics and it remains the standard comparison for all other models. The nuclear shell model shares many analogies with the atomic shell model. Just like the case of electrons in the atomic structure, nucleons are *fermions* (i.e. particles with intrinsic spin $s = \frac{1}{2}\hbar$) that sequentially fill discrete orbits of a central potential. The *Pauli exclusion principle* prohibits any possible collisions especially of the inner-shell nucleons, and that, no two fermions can have the same set of *quantum numbers* [51].

Each quantum state in a spherical shell model is identified by a unique set of quantum numbers *n, l, s, j* and *m*. The principle quantum number *n* represents the number of radial nodes in a nucleon's wavefunction. The orbital quantum number is given by *l, s* is the intrinsic spin angular momentum, $j = l + s$ represents the total angular momentum, and *m* is the magnetic substate of a nucleon (i.e. a projection of *j* onto an arbitrary *z*-axis). The *l* values are given by their historical, spectroscopic notation, Table 2.1.

TABLE 2.1: Spectroscopic notation for different values of orbital momentum, l

l value	0	1	2	3	4	5	6
l letter	s	p	d	f	g	h	i

In the case of the atomic shell model, electrons move in a central (spherically symmetric) Coulomb field created by a small internal, but relatively massive, and highly charged nucleus. The shell structure of nuclei is more complex than that; the central field in which nucleons move is self-generated. Atomic electrons are far apart and interact weakly by long-range electromagnetic forces, which are well understood. Nucleons inside the nucleus are close to one another and interact strongly by short-range nuclear forces that are relatively poorly understood. The mean field produced by the ensemble of nucleons creates a potential in which individual nucleons reside in quantized states with single-particle wave functions [52]. In the development of the *independent-particle* shell model a number of different forms for the potential are explored, and solved for state wavefunctions using the *time-independent* Schrödinger equation

$$\left\{ \frac{-\hbar^2}{2\mu}\nabla^2 + V(r) \right\} \Psi(r) = E\Psi(r). \tag{2.1}$$

In this Equation 2.1, Ψ is the wavefunction of the bound nucleon, and E is the energy eigenvalue of the state. The expression in the curly bracket is the kinetic energy of the nucleon and its energy due to the binding potential well of the nucleus; the two terms constitute the Hamiltonian operator ($\hat{H}$). For the potential $V(r)$, the first choice is an attractive, analytic, and manageable form: an *infinite square well* potential with radius R, described by

$$V(r) = \begin{cases} -V_0 & r \leq R, \\ \infty & r > R. \end{cases} \tag{2.2}$$

The square well, Fig. 2.2(a) however is an oversimplification as it has sharp edges, which do not approximate the nuclear charge and matter distribution. Also it does not reproduce the expected magic numbers. The *spherical harmonic oscillator* is another simple class of potential that may be applied. Its potential has the form

$$V(r) = \frac{1}{2}kr^2 = \frac{1}{2}mw^2r^2, \tag{2.3}$$
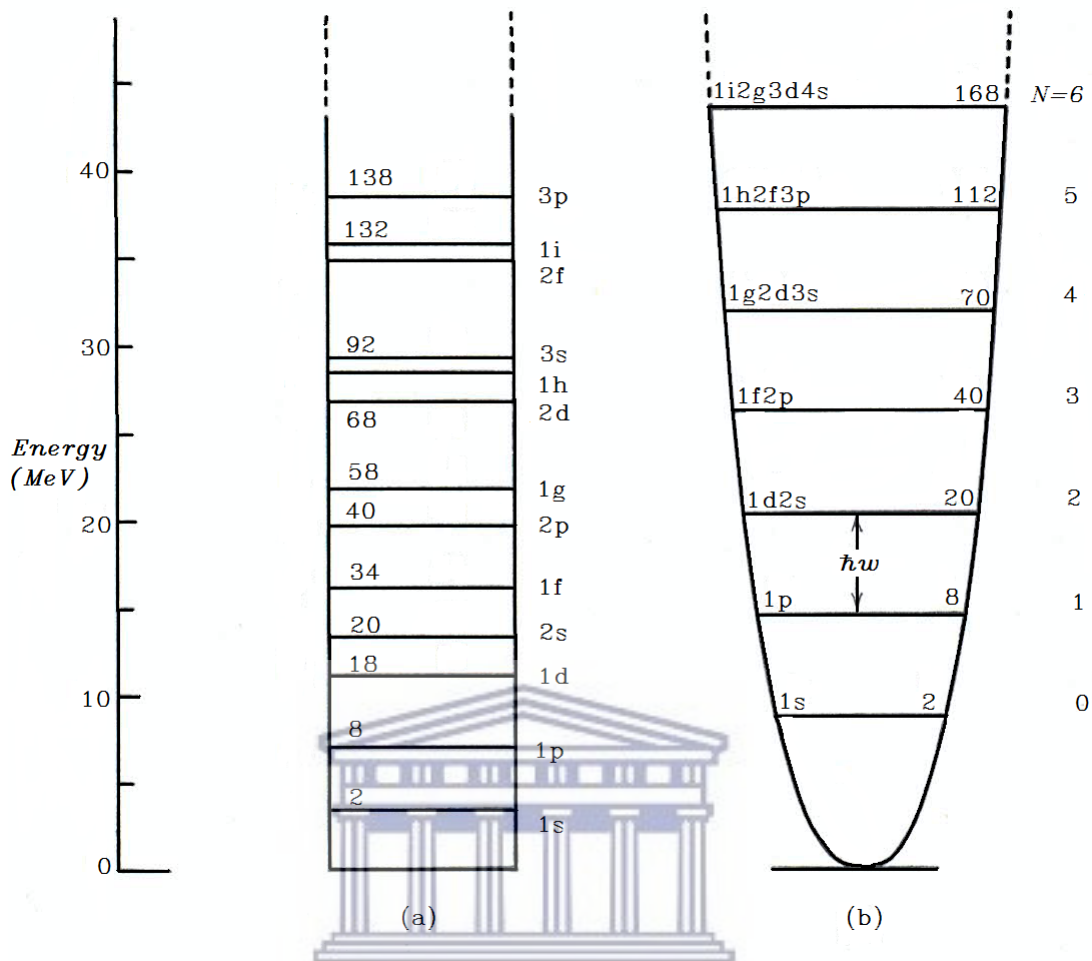
FIGURE 2.2: Level sequence for in a potential well showing spectroscopic classification of levels and total number of nucleons on each level. (a) Infinite square well potential, (b) Harmonic oscillator potential with uniform spacing of levels [6].

where m is the particle mass, r the distance of the particle from the centre of the nucleus in spherical coordinates, and ω is the angular frequency of the particle. The solution of the Schrödinger equation in an oscillator potential performs much better than those of the square well, see Fig. 2.2(b). The energy levels are occurring at particle numbers 2, 8, 20, 40, 70, and 112 as shells are filled. The first three values coincide with the known magic numbers but beyond that the real shell closures differ from the predicted ones.

$$V(r) = -\frac{V_0}{1 + e^{\left[\frac{r-R}{a}\right]}} \tag{2.4}$$

A more realistic potential which resemble the nuclear density distribution is the

Woods-Saxon potential [53]. The shape of the potential can be parametrized as given by Equation 2.4, where a is the *diffuseness* of the potential, the radius of the potential $R = r_0 \times A^{\frac{1}{3}}$ where A is the mass of the nucleus and r_0 is the radius parameter. Unfortunately, single-particle orbitals obtained using this potential form do not completely match the experimentally measured shell gaps and occupancies. The potential is modified by the addition of a spin-orbit coupling force in analogy with atomic physics.

$$V_{so}(r) = V_{ls}\left[2\left(\frac{\hbar}{\mu c}\right)^2 \frac{1}{r}\frac{d}{dr}\left\{\frac{1}{1+e^{\left[\frac{r-R}{a}\right]}}\right\}\right]\vec{l}\cdot\vec{s}, \tag{2.5}$$

where V_{ls} represents the strength of the spin-orbit interaction. The spin-orbit operator $\vec{l}\cdot\vec{s}$ is given by

$$\vec{l}\cdot\vec{s} = \frac{1}{2}\left[j\left(j+1\right) - l\left(l+1\right) - s\left(s+1\right)\right]. \tag{2.6}$$

It was Goeppert-Mayer along with Haxel, Jensen and Suess [54–56] who introduced a spin-orbit interaction, which had the effect of splitting each angular momentum orbital, l, into non-degenerate levels of spin, $j = l \pm \frac{1}{2}$. The energy splitting increases with increasing l. The energy of a state with given l, excluding the s-orbital assumes two values depending on the spin orientation, $j = l - \frac{1}{2}$ for higher energy and $j = l + \frac{1}{2}$ otherwise. High-j orbitals are forced down in energy and as such reside amongst levels of the lower major oscillator shell as shown by lines highlighted in Fig. 2.3. The lower shell has opposite parity, therefore the *intruder* orbital does not interact with its opposite parity neighbours. The maximum number of protons/neutrons that each of these split levels can contain i.e. degeneracy, is equal to $(2j+1)$. The application of a Woods-Saxon potential coupled with this spin-orbit term yields the correct sequence of levels and experimentally observed magic numbers 2, 8, 20, 28, 50, 82, and 126, see Fig. 2.3.

The shell model is very successful in explaining nuclear excitation energies, their spin quantum numbers and transition probabilities between those levels. It works well in low mass regions, where most nuclei are close to completed shells, however, at higher mass values, the huge amounts of computer power needed makes the approach unfeasible. Independent particle models like the nuclear shell model tend to have more difficulty in describing the structure of nuclei away from closed shells
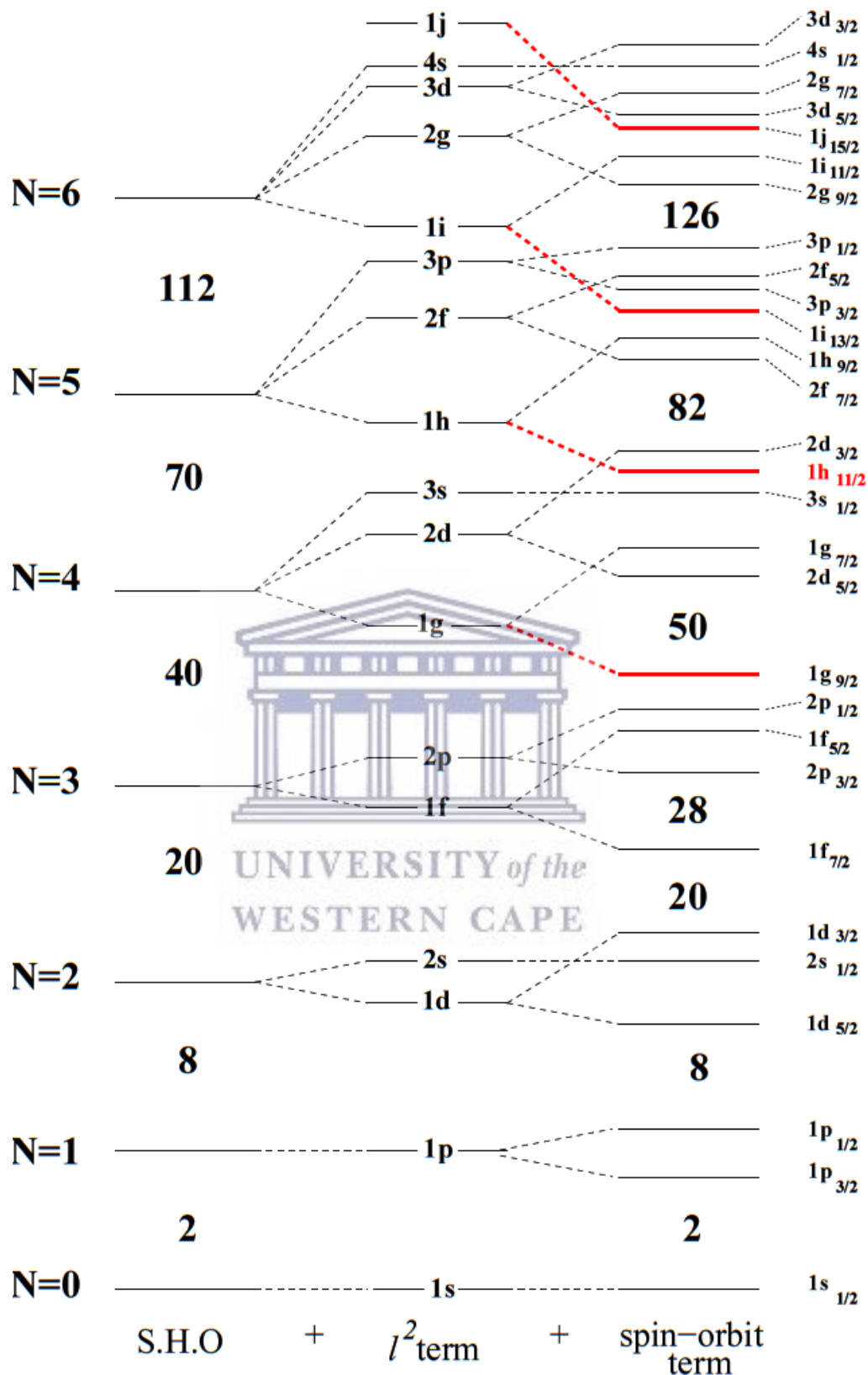
FIGURE 2.3: The evolution of single-particle energies from a *simple harmonic oscillator* (S.H.O.) potential (left) to a realistic *shell model* potential. The *Woods-Saxon* potential with spin-orbit coupling reproduces the observed magic numbers. *Intruder* states are illustrated by red lines.

where collective modes of excitation become more dominant. To describe these nuclei, macroscopic models are often used, which describe the global properties of the nuclear matter instead of the behaviour of individual constituents.

2.3   The Collective Nuclear Models

The shell model describes the magic numbers and many other properties such as single-particle ground state level spins fairly well, however, it has a number of failures far away from the closed shells. The most outstanding one is the fact that the observed experimental quadrupole moments are much larger than those of the single-particle predictions, suggesting the existence of collective nuclear motion which involve many nucleons. It fails to account for the enhanced $E2$ transition probabilities encountered in the study of heavy nuclei.

The development of nuclear structure in medium and heavy nuclei has followed two related paths: the *vibrational* model and *rotational* model. Such models are *collective* models because they attempt to describe the nucleus as a collection of nucleons moving coherently, rather than independently acting particles. The collective model first proposed by Bohr and Mottelson [1, 57] has had far reaching success in describing the static and dynamic properties of the low-lying nuclear states. The Bohr-Mottelson model pictures a competition between long and the short-range forces near nuclear surface that can result in vibrations of a spherical equilibrium shape or in a permanent deformed structure capable of undergoing rotational motion. For a nucleus of constant density, these oscillations have the character of surface waves. In the model the moving nuclear surface is described by an expansion in spherical harmonics of multipole order λ, with time-dependent shape parameters as coefficients:

$$R(\theta, \phi, t) = R_0 \left[1 + \sum_{\lambda=0}^{\infty} \sum_{\mu=-\lambda}^{\lambda} \alpha_{\lambda\mu}(t) Y_{\lambda\mu}(\theta, \phi) \right], \tag{2.7}$$

where $R(\theta, \phi, t)$ denotes the nuclear radius in the direction (θ, ϕ) at time t, and R_0 is the radius of the spherical nucleus which is realized when $\alpha_{\lambda\mu}$ vanish. The time-dependent amplitudes $\alpha_{\lambda\mu}(t)$ describe the vibrations of the nucleus with different multipolarity around the ground state. Terms of order $\lambda = 0$, the so-called *breathing* mode are ignored since they correspond to density changes of the nucleus

as a whole. This can occur, but only at very high energies ∼10-20 MeV. Similarly, $\lambda = 1$ (the *dipole* mode) terms are dropped since they correspond to the motion of the center of mass. The third term, with $\lambda = 2$, correspond to the *quadrupole* mode of deformation. Other deformation modes include $\lambda = 3$ the *octupole* mode and $\lambda = 4$ the *hexadecapole* mode which are beyond the scope of this work. The quadrupole mode is the main focus of this work.

2.3.1 Quadrupole vibration

The Hamiltonian for such a surface 2.7 corresponding to the $\lambda = 2$ mode of oscillation can be written as

$$
\begin{aligned}
H &= T + V \\
&= \frac{1}{2}\sum_\mu \left[B_2|\frac{d\alpha_{2\mu}}{dt}|^2 + C_2|\alpha_{2\mu}|^2 \right],
\end{aligned}
\tag{2.8}
$$

where B and C are the mass parameter and the effective surface tension (or "nuclear stiffness") in analogy with the mass and restoring force constant, respectively, of a simple harmonic oscillator. The sum over μ takes into account the five independent modes of vibrations which are possible for $\lambda = 2$. Transforming the above classically oriented description into the operator formalism of quantum mechanics yields an expression for the nuclear Hamiltonian

$$
H_{vibr} = E_0 + \hbar\omega \sum_\mu \left(\mathbf{b}^\dagger_{2\mu}\mathbf{b}_{2\mu} + \frac{1}{2} \right) + C \sum_\mu \left[\left(\mathbf{b}^\dagger_{2\mu}\mathbf{b}^\dagger_{2\mu}\right)^2 \left(\mathbf{b}_{2\mu}\mathbf{b}_{2\mu}\right)^2 \right],
\tag{2.9}
$$

where $\mathbf{b}^\dagger_{2\mu}$ and $\mathbf{b}_{2\mu}$ are creation and annihilation oscillator quanta (i.e. *phonons*) with spin 2 and parity $(-1)^\lambda$. Phonons have integral spin, so they obey *Bose* statistics. The characteristic angular frequency of the system is given by $\omega = \sqrt{\frac{C}{B}}$: E_0 corresponds to the zero-point energy. Quadrupole vibrations are created and destroyed by acting on a *vacuum* state like

$$
\psi_{ph} = \mathbf{b}^\dagger_{2\mu}|0\rangle,
\tag{2.10}
$$

and

$$\mathbf{b}_{2\mu}\left|0\right\rangle = 0, \tag{2.11}$$

respectively. In essence, the creation and destruction operators follow the usual operator rules

$$\mathbf{b}^{\dagger}{}_{2\mu}\left|n\right\rangle = \sqrt{n+1}\left|n+1\right\rangle \tag{2.12}$$

and

$$\mathbf{b}_{2\mu}\left|n\right\rangle = \sqrt{n}\left|n-1\right\rangle, \tag{2.13}$$

where $\left|n\right\rangle$ is a state with n phonons. Multiphonon excited states (of n quanta) can be obtained by operating on the vacuum with n-phonon creation operators. Solution of the oscillator equation gives energy eigenvalues of the nuclear states as

$$E = \hbar\omega_2(n + \frac{5}{2}), \tag{2.14}$$

where n is the number of vibrational quanta present. For an even-even nucleus, the ground state has $n = 0$ (number of phonons) and a J^{π} assignment of 0_1^+. The first quadrupole vibration produce a 2_1^+ state at an energy level $\hbar\omega$. To produce the next excitation ($n = 2$), the two quadrupole phonons are coupled together and this results in a degenerate triplet of states $0_2^+, 2_2^+, 4_1^+$ at an energy level $2\hbar\omega$. The states with spin 1 and 3 at the two-phonon level are forbidden by the requirement that the wave function of two identical bosons must be symmetric under exchange. An $n = 3$ excitation is fivefold degenerate with levels of spins $0_3^+, 2_3^+, 3_1^+, 4_2^+, 6_1^+$ at a level energy $3\hbar\omega$. This produces a pattern of equidistant energy levels as shown in Fig. 2.4(a). The degeneracy between the states (e.g. the triplets $0_2^+, 2_2^+, 4_1^+$) is lifted by residual p-n interactions. Since the quadrupole operator is a one phonon creation or destruction operator, transitions like $2_2^+ \rightarrow 0_1^+$ (i.e. crossover transitions from a two-phonon triplet state to ground state) are forbidden. The selection rule for transitions between vibrational states is $\Delta n = \pm 1$. Transitions between the states of the $n = 2$ triplet are equally forbidden. The reduced transition probabilities $B(E2; n+1 \rightarrow n)$ between higher states of the vibrational band are given as simple multiples of $B(E2; 2_1^+ \rightarrow 0_1^+)$. For an example the decay of the two-phonon quadrupole triplet (see Fig. 2.4(b)), the $B(E2)$ values are, in an obvious notation,
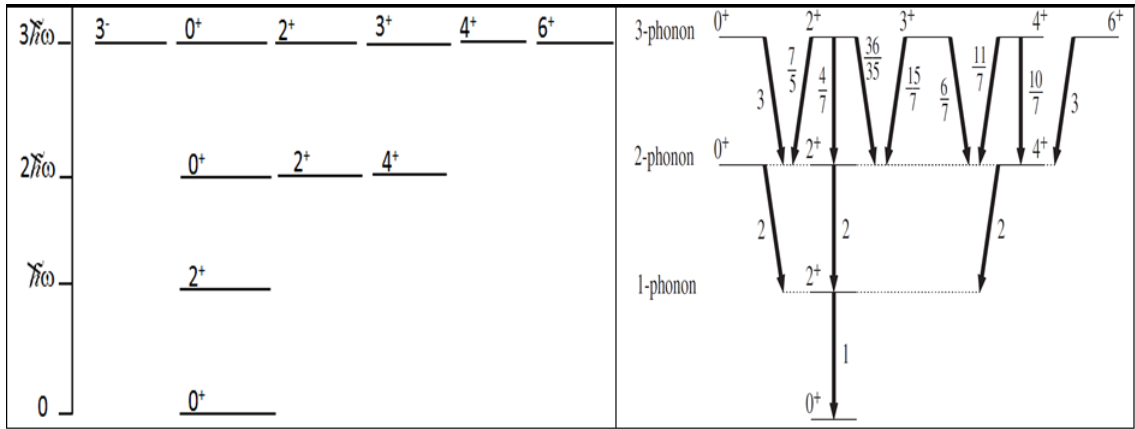
FIGURE 2.4: Low-lying levels from the quadrupole harmonic vibrator phonon model.

$$B(E2; 0_2^+, 2_2^+, 4_1^+ \rightarrow 2_1^+) = 2B(E2; 2_1^+ \rightarrow 0_1^+). \tag{2.15}$$

Generally, transition strengths are measured using the Weisskopf single-particle estimate (these will be discussed in detail in Subsection 2.4.2). Collective model predicts enhanced transition strengths, for the decay of the 2_1^+ state, with enhancement factors normally observed to be from 10 to 50, for vibrational nuclei

$$B(E2; 2_1^+ \rightarrow 0_1^+) = \frac{25Z^2\hbar}{8\pi\omega_2 B_2} B_{sp}(E2; 2 \rightarrow 0), \tag{2.16}$$

where $B_{sp}(E2; 2 \rightarrow 0)$ is single-particle estimate for the decay of the first excited 2^+ state to ground state given by

$$B_{sp}(E2; 2^+ \rightarrow 0^+) = \left(\frac{3}{4\pi} ZeR_0^2\right)^2 \frac{\hbar}{2\omega_2 B_2}. \tag{2.17}$$

Also notable in collective models, magnetic transitions like $M1$ are extremely inhibited in vibrational nuclei.

2.3.2 Quadrupole deformation

For a static deformed nucleus, the center of mass motion expansion coefficients $\alpha_{21} = \alpha_{2-1}$ are set to 0. The remaining coefficients are then parametrized in terms of *Bohr* coordinates, β which represents the quadrupole deformation and γ the axial asymmetry [58]
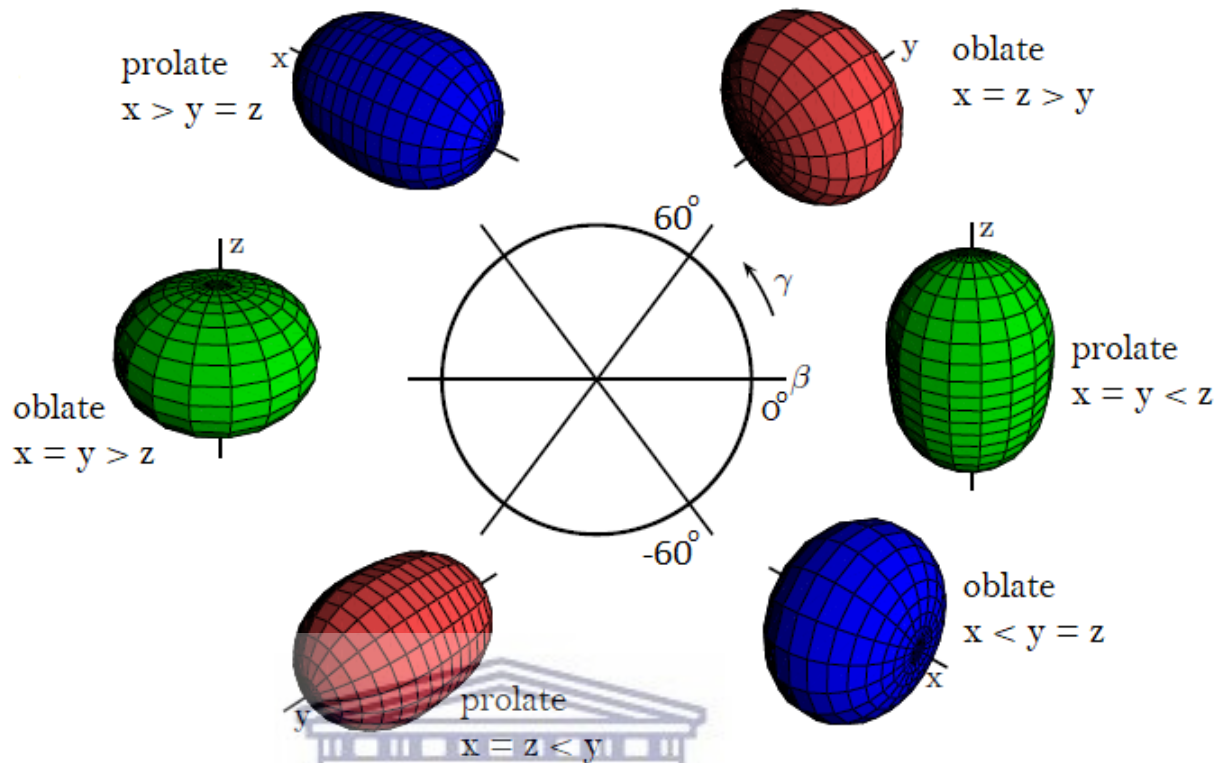
FIGURE 2.5: The quadrupole deformed shapes corresponding to $\beta > 0$ and $\gamma = \frac{n\pi}{3}$, with $n \in \mathbb{Z}$, two of the three semi-axes are of equal length [7]. Different colors have been used for different axes of symmetry (green for z, red for y and blue for x).

$$\alpha_{20} = \beta cos\gamma, \tag{2.18}$$

$$\alpha_{22} = \alpha_{2-2} = \frac{1}{\sqrt{2}}\beta sin\gamma. \tag{2.19}$$

In this formalism, β denotes the deviation of the nucleus from sphericity along an axis of cylindrical symmetry and β is always greater or equal to 0, while γ represents the degree of axial asymmetry. The parameter γ takes one of two limiting values: $\gamma = 0°$ or $\gamma = 60°$. If $\gamma = 0°$, then $\beta > 0$ corresponds to a nucleus with an elongated ellipsoidal or *prolate* shape. Conversely, $\gamma = 60°$ and $\beta > 0$ corresponds to a compressed or *oblate* shape. A *triaxial* shape is formed when $\beta > 0$ and $0° < \gamma < 60°$ (i.e. x $\neq$ y $\neq$ z). This is shown in Fig. 2.5.

2.3.3 Collective behaviour in even-even nuclei with static deformation

As more nucleons are added to the nuclei beyond closed shells, nuclei become less rigidly spherical, they vibrate more slowly and eventually become unstable against assuming a deformed equilibrium shape. Rotational motion can be observed only in nuclei with non-spherical equilibrium shapes. A rotational Hamiltonian (for a deformed nucleus with ground state spin-parity $J^\pi = 0^+$) is expressed as

$$H = \sum_i \frac{I_i^2}{2\mathscr{I}_i}, \tag{2.20}$$

where $\mathscr{I}_i$ are the principal moments of inertia and I is angular momentum quantum number. The energy eigenvalues are then given by

$$E = \frac{I(I+1)\hbar^2}{2\mathscr{I}}. \tag{2.21}$$

Only even values i.e. $I = 0, 2, 4, ...$ are allowed since the wave function Ψ_{rot} vanishes for odd values [59, 60]. The characteristic quadratic $I(I+1)$ dependence of the energies of states in rotational bands is in fact a common observed phenomenon for many nuclei in mid-shell regions of the nuclear chart. A convenient way to characterise the extent to which a nucleus is rotational is by the ratio $E(4_1^+)/E(2_1^+)$, which should approximately equal to 3.33 for a rigid-rotor.

2.4 Electromagnetic Transitions in Nuclei

Nuclear excited states can be populated by a number of processes such as α decay, β decay and nuclear reactions like those detailed below in Section 2.8.1. A nucleus in an excited state may decay to a lower energy state in the nucleus via an emission of an electromagnetic transition; a γ ray or conversion electron. Note that there is no change in Z or A during this type of decay. Every electromagnetic wave consists of an oscillating *electric* and *magnetic* field. The oscillating electric field of the γ ray is caused by an oscillating electric charge whereas the oscillating magnetic field is caused by an oscillating electric current. The electromagnetic radiation is quantized into basic units of *photons*.
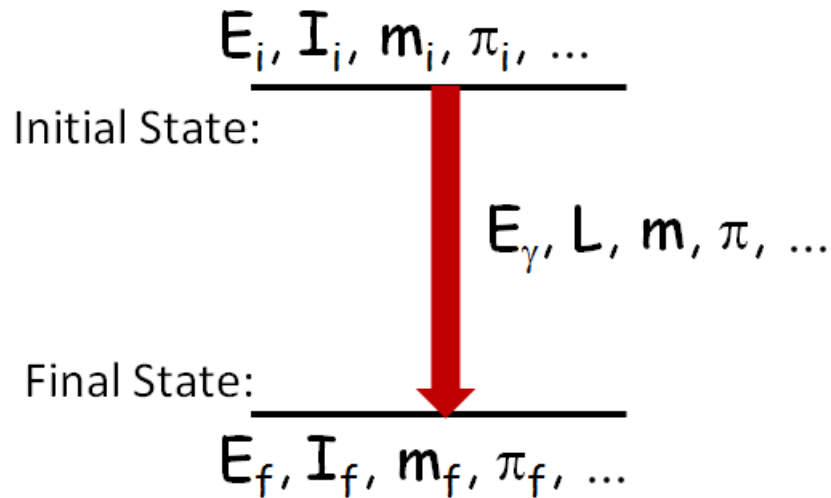
FIGURE 2.6: An electromagnetic transition from an initial state to a final state.

Gamma rays are one of the few direct observables that can be used to understand nuclear structure; using different techniques it is possible to determine energy, spin and parity of states with which one can begin to understand the evolution of structure in excited nuclei.

2.4.1   Angular momentum and parity selection rules for electromagnetic transitions

Consider an electromagnetic transition from an initial excited state $|\psi_i\rangle$ of energy E_i, angular momentum J_i and parity π_i to a final state $|\psi_f\rangle$ of energy E_f, J_f and π_f, see Fig. 2.6. The γ-ray energy released is given by

$$E_\gamma = E_i - E_f = \hbar\omega, \tag{2.22}$$

if the nuclear recoil energy is neglected. The emitted photon carries a *total angular momentum* L (of absolute magnitude $\sqrt{L(L+1)}\hbar$). Since angular momentum is a conserved quantity in electromagnetic interactions, it follows that in the nuclear transition, a closed vector triangle relation applies such that

$$\mathbf{J}_i = \mathbf{J}_f + \mathbf{L}. \tag{2.23}$$

This constitutes an *angular momentum selection rule*, which restricts the permitted range of multipolarity L to within limits

$$|J_i - J_f| \leq L \leq J_i + J_f. \tag{2.24}$$

The electromagnetic radiation represented by the rank L has multipolarity 2^L, e.g. a rank $L = 1$ radiation has multipolarity 2^1 designated as *dipole*, $L = 2$ radiation has multipolarity 2^2 a *quadrupole*, and so on. The multipolarity of the photon is a quantification of the amount of angular momentum carried away by the photon. Note, rank $L = 0$ radiation with multipolarity 2^0 (a *monopole*) are forbidden to take place by electromagnetic radiation as they are *Bosons* and have an intrinsic spin $s = 1\hbar$. The only way in which electromagnetic decays can participate in $0 \rightarrow 0$ transitions is through second-order processes such as a double-γ emission or by the emission of a conversion electron. However, the probability for these processes to take place is relatively low. Transitions in which L takes on the value $L = J_i - J_f$ are referred to as *stretched*, otherwise they are known as *folded* transitions.

The selection rules for *parity* change in the transition is given by the

$$\Delta\pi(EL) = \pi_i\pi_f = (-1)^L \tag{2.25}$$

for an *electric* transition of order L, and is

$$\Delta\pi(ML) = \pi_i\pi_f = (-1)^{L+1} \tag{2.26}$$

for a *magnetic* transition so that radiation EL or ML for $\Delta\pi = 0$ parity is $M1, E2, M3, E4, ...$ and radiation EL or ML for $\Delta\pi = \pm 1$ parity is $E1, M2, E3, M4, ...$, a further illustration is given in Fig. 2.7. It is clear that more than one multipole of transition will satisfy these selection rules. In these cases, the lowest order multipole will usually dominate the transition and it has the largest transition probability [61].
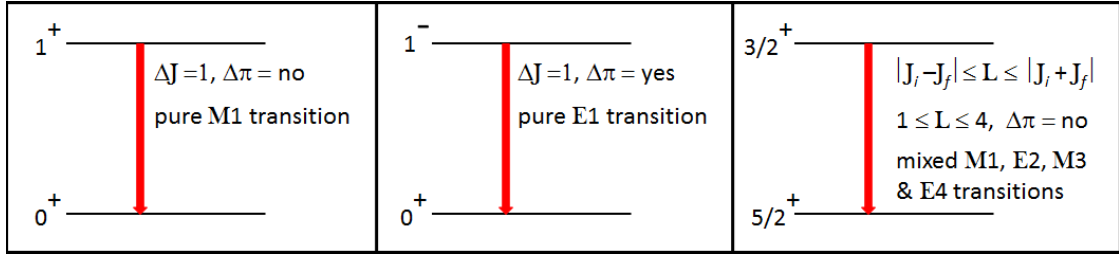
FIGURE 2.7: Examples of γ ray transitions which illustrate the application of selection rules.

2.4.2 Theory of electromagnetic transition probabilities

Measured γ ray transition rates are usually written in terms of reduced transition rates as follows [62]

$$T_{fi}(\lambda L) = \frac{8\pi(L+1)}{\hbar L\left((2L+1)!!\right)^2}\left(\frac{E_\gamma}{\hbar c}\right)^{2L+1} B(\lambda L : I_i \to I_f), \qquad (2.27)$$

where $B(\lambda L)$ is the reduced transition probability. The transition multipolarity λ represents electric (E) or magnetic (M), and it carries L units of angular momentum and E_γ is the energy (in MeV) of the emitted γ ray. The reduced transition probabilities for a transition of an electric (or magnetic) λ-pole transition from an initial state $|I_i\rangle$ to a final state $|I_f\rangle$ are given by the following expression

$$B(\lambda L : I_i \to I_f) = \frac{1}{2I_i + 1}|\langle I_f|\mathcal{M}(\lambda L)|I_i\rangle|^2, \qquad (2.28)$$

where $\mathcal{M}$ is the electric (or magnetic) multipole operator for a transition. It is basically the squared transition matrix element, averaged over initial states. The matrix elements contain information about the structure of the nucleus. Note that unlike the transition rates formula, reduced transition probabilities have no E_γ^{2L+1} energy dependence. Therefore, the $B(\lambda L)$ value is often quoted to compare decay rates between different nuclei. From Section 2.3 it is clear that reduced transition probabilities can be used as an indicator of the collective excitation modes of the nucleus. Also, for a statically deformed nucleus, $B(E2)$ values can be helpful for extraction of the quadrupole deformation parameter, β from the relationship

$$B(E2 : 2_1{}^+ \to 0_1{}^+) = \frac{1}{5}\left[\frac{3}{4\pi}ZeR_0{}^2\beta\right]^2, \qquad (2.29)$$

where $R_0 = 1.2A^{\frac{1}{3}}$ fm.

Weisskopf single particle estimates

In order to quantify whether a transition is relative weak or strong, one often gives the $B(\lambda L)$ value in "*single-particle units*" or *Weisskopf units* [63]. The Weisskopf unit is an estimate of the strength that would be observed for a given transition assuming that it is due to only a single-particle (a proton or neutron) moving between spherical orbits, and how it depends upon mass. This is particularly true near closed shells, where the nucleus is spherical to first order. Also only a few nucleons are significantly involved with the excited states. By convention it is defined by

$$B(EL)_{W.u.} = \left(\frac{1}{4\pi}\right)\left[\frac{3}{(3+L)}\right]^2 (1.2A^{\frac{1}{3}})^{2L} \tag{2.30}$$

for electric transitions in units of $e^2[\text{fm}]^{2L}$ and

$$B(ML)_{W.u.} = \left(\frac{10}{\pi}\right)\left[\frac{3}{(3+L)}\right]^2 (1.2A^{\frac{1}{3}})^{2L-2} \tag{2.31}$$

for magnetic in units of $\mu_N^2[\text{fm}]^{2L-2}$, where μ_N is the nuclear magneton and A the atomic mass number. The most commonly used are:

$$B(E1)_{W.u.} = 0.0645A^{\frac{2}{3}}e^2\text{fm}^2, \tag{2.32}$$

$$B(E2)_{W.u.} = 0.0594A^{\frac{4}{3}}e^2\text{fm}^4, \tag{2.33}$$

and

$$B(M1)_{W.u.} = 1.790\mu_N^2. \tag{2.34}$$

If a transition is observed to have a strength which is comparable to the single-particle estimates given above, it can be taken as an indication that single-particle degrees of freedom may be appropriate to describe the nuclear behaviour. However, for measured strengths that are higher than the Weisskopf estimates by many orders of magnitude, that can be an indication that the nucleus has a structure

characteristic of a collective behaviour. The transition strength is directly related to the overlap of the wavefunctions of the states involved in the transition; they provide insight into the configuration of the nuclear states. In this way, the structure of the nuclear states can be discussed even without detailed theoretical information.

2.5 Pairing in Nuclei

The importance of the pairing forces in nuclei has been recognized for many years [64]. The pairing was introduced to recreate the observed nuclear data such as binding energies, neutron and proton separation energies, angular momentum of nuclear ground states and the low density of states at low excitation energy in even-even nuclei. A deeper understanding of pairing phenomena was obtained when the theory of Bardeen, Cooper and Schrieffer [65], developed to describe the behaviour of electrons in superconductors, was extended to nuclear physics. Immediately after that Bohr *et al.* [23] recognized that these concepts could provide a basis for analyzing the pair correlations and observed pairing effects in nuclei. Indeed, the pairing force creates specific excitations in nuclei near or at a closed shell, which are referred to as *pairing vibrations* which have previously alluded to in Chapter 1.

The pairing force in nuclei couples nucleons in time-reversed orbits to states of zero angular momentum. The phenomenon is strongly favoured in nuclei with two neutrons or two protons outside of doubly closed shells. In even-even nucleus, all of the nucleons "pair off" in this fashion and is responsible for the fact that the ground state spin is always $I^\pi = 0^+$. It takes an energy of more than 1 MeV to break a $J = 0$ coupled proton pair [66]. One of the most dramatic features of pairing interactions is the occurrence of an energy gap in the spectra of even-even nuclei in contrast to the neighbouring odd-mass nuclei. Particles interact through a pairing force with a strength that is small relative to the magnitude of the gap. The pairing model assumes the existence of a large number of states above and below an energy gap. For the case of two particles in a single j orbital, the pairing interaction is given by

$$V_{pairing} = -G \sum_{i,j>0} a_i{}^+ a_{\bar{i}}{}^+ a_{\bar{j}} a_j = \frac{1}{2} \Delta \sum_i (a_i{}^+ a_{\bar{i}}{}^+ + a_{\bar{i}} a_i), \qquad (2.35)$$

where G is the strength of the pairing interaction ($G_p = \frac{17}{A}$ MeV for protons and $G_n = \frac{23}{A}$ MeV for neutrons [8]) and Δ is the pairing gap. In this description the operator $a_i{}^+ a_{\bar{i}}{}^+$ can be replaced by $a_i{}^+ b_{\bar{i}}$, describing annihilation of a hole in the time reversed state i, and creation of a particle in a state i. The operator $a_{\bar{i}} a_i$ can be replaced by $b_{\bar{i}}{}^+ a_i$ describing annihilation of a particle in state i and creation of a hole in a time-reversed state $\bar{i}$.

2.6   Intruder States at the Z = 50 Closed Shell

The cadmium nucleus has Z = 48 and there are two proton holes relative to the closed Z = 50 shell, which interact with the valence neutrons. This configuration gives normal states. If two protons are promoted to the next higher 50-82 shell, there are now 2 valence protons and 4 valence proton-holes, which may interact with the valence neutrons. With this configuration, another set of states are created which are identified as *intruder states*. In this configuration, there are six valence protons, whereas the normal states only had two valence protons available to interact with the same number of valence neutrons, see Fig. 2.8. The additional number of valence protons increases the attractive forces between the nucleons i.e. the $p - n$ interactions. A higher number of $p - n$ interactions correspond to a "*softer*" nucleus; this causes the intruder levels to be more deformed than the normal states and the intruder state excitation energies are lowered. The varying deformed shapes of the intruder and normal levels are due to the different mean square radii associated with each configuration. The states with different deformations can coexist in one nucleus at the same time. This is a well known phenomenon in nuclear physics which is known as *shape coexistence*.

2.7   Shape Coexistence

This is the phenomenon where multiple shapes coexist in a narrow energy region at relatively low-lying levels of the nucleus. This is a widespread phenomenon across the nuclear chart [37, 67]; it is due to the residual pairing correlations, which cause protons and neutrons to separately form $J = 0$ Cooper pairs. These nuclei have a 0^+ spherical ground state and multiple excited 0^+ states, which are band heads for deformed rotational bands.
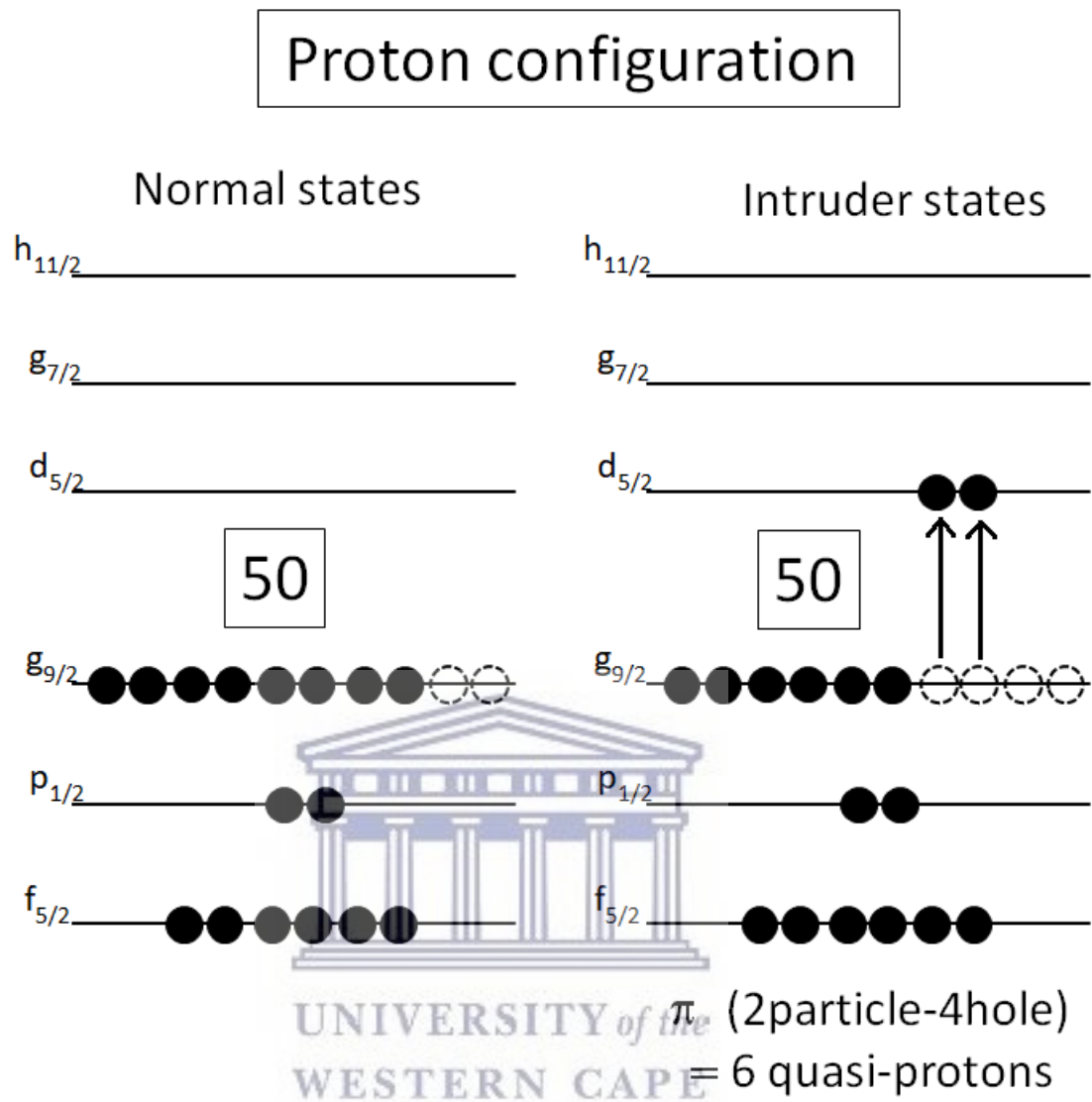
FIGURE 2.8: Schematic diagram showing intruder excitations and normal states in Cd. Adapted from [8].

When a nucleus exhibits shape coexistence, it is possible that mixing between intruder states and normal states will occur. States of the same spin and parity can mix which would alter the level energies and electromagnetic strengths. Due to this mixing of the states, it is often the case that transition rates in nuclei with quadrupole vibrational character will not agree with those predicted in the model. Electromagnetic transitions between normal and intruder states are normally forbidden. However, if such transitions do occur due to mixing, the strength from an "allowed" transition may be mixed with that of a forbidden one.

2.8   Reaction Mechanisms

Different types of reactions can take place during a nuclear collision. Basically, two extremes have been recognised when two nuclear systems collide; (i) the beam and target may coalesce to form a highly excited compound system, a *compound* nuclear reaction, (ii) the other (which is of interest in this work), a beam particle may make just glancing contact with the target and immediately separate, a *direct* nuclear reaction.

2.8.1   Direct Nuclear Reactions

Direct reactions are peripheral reactions that occur in time-scales of the order of the transit time of the projectile across the target, 10^{-22} s. Very few nucleons are involved in the reaction process, and to first order, all of the remaining nuclei within the target can be considered as passive "spectators". Direct nuclear reactions directly connect the initial and final states in a reaction without the formation of an intermediate compound system. A consequence of this is that the observed cross-section in a direct reaction varies slowly with incident beam energy. This is in contrast to compound nuclear reactions, which involve the formation of an intermediate nucleus with many stages of deformation, excitation and decay, whose lifetimes may be 10^4 or more times greater than the basic transit times [68]. Another spectroscopic feature of direct nuclear reactions is that the angular distribution of the emitted particle from a direct reaction will tend to show forward-peaked angular distributions of a diffractive character resulting from strong absorption first observed by Butler *et al.* [69, 70].

Direct nuclear reactions, generally can be divided into two classes, the *stripping* reactions in which part of the incident projectile is "stripped away" as it enters the target nucleus thereby creating a residual nucleus in a *particle state*, on the contrary, the *pickup* reactions in which the outgoing emitted particle is a combination of the incident projectile and one or more of the target nucleons thereby leaving behind a residual nucleus in a *hole state* [71]. The picked-up nucleon is removed from an occupied quantum state and the emerging ejectile (the incident projectile + picked nucleon(s)) conveys some information about this state. Conversely, in stripping, the captured nucleon occupies one of the available quantum states in the target nucleus, and the other carries some information concerning this state. This

makes stripping reactions a useful tool to use to study unoccupied single-particle nuclear states and pickup to investigate occupied states. The shell structure of the nucleus can be directly observed in direct reactions.

Direct reactions are significant because of their tendency to populate low-lying states of nuclei. The low-lying levels are most closely related to the structure of the ground state; they involve minimum re-arrangement in the state of motion of the nucleons. This is the principal motive for using them in this study of the low-lying collective states. They give a very specific and selective information on the properties of nuclear levels. Due to their relatively simple nature, with no complications from a intermediate compound system, direct nuclear reactions are well suited to give information about the relationship (overlap) between the ground state of the target nucleus and the ground (or a particular excited) state of the residual nucleus, i.e. it is mainly states that have a large parentage based on the target in its ground state that are most favoured [72, 73]. Direct reactions are one-step processes that occur via a single degree of freedom. A direct reaction is therefore thought of in terms of a short duration interaction connecting the initial and final states by a comparatively simple mechanism. Direct and compound nuclear reactions are not mutually exclusive; both types of process may contribute to a given reaction leading to a particular final state.

2.8.1.1   Single-nucleon transfer reactions

A typical prototype of these reactions is the deuteron stripping $A(d, p)B$ in which a neutron is stripped from the projectile and transferred to the target. With this simple addition of one neutron in a particular shell model orbit, it is possible to learn to what degree a given residual nuclear state looks like the target ground state plus a neutron. This allows crucial information to be obtainable about the single neutron structure, and hence allow the extraction of quantities such as *spectroscopic factors* which are of great importance in nuclear spectroscopy. Theoretically, the spectroscopic factor can be viewed as the overlap integral between the initial and final state of the target nuclei [74]. From the spectroscopic factor, the occupation probabilities of the shell model single-nucleon states can be inferred. It measures the strength of the single-particle component in the final-state wave function. In the theory of shell model which was discussed in detail in the

previous Section 2.2, the valence nucleon in the nucleus is described as a single-particle state of a particular orbit, identified by a set of quantum numbers *n, l and j*. The spectroscopic factor is unity only in the limit of the noninteracting independent particle shell model for closed-shell target nuclei. The assumption that the nucleon occupies a pure single-particle state is an idealization. This situation is true only in few cases, especially those near closed shells in real nuclei. Residual interactions among other nucleons (especially with more valence nucleons away from closed shell) would cause the nuclear shell state to be spread over several, or even many nuclear states.

Single-particle transfer reactions are simplest to interpret when either the state of the target nucleus or of the final nucleus has spin zero. The spin and parity of the transferred nucleon in a direct single nucleon transfer reaction is simply the difference in the spin and parity of the initial and final nuclear states. The most striking feature of direct reactions is that the angular distribution of the outgoing particles reflects the transferred angular momentum and parity, and the *l*-value can be extracted easily. In a semi-classical treatment [75, 76], illustrated in Fig. 2.9, the relationship of the transferred angular momentum of the neutron ($\vec{\boldsymbol{p}}_n$) to the scattered angle of the proton θ (with $\vec{p}_d$ and $\vec{\boldsymbol{p}}_p$ the wave vector of deuteron and scattered proton, respectively) is given by conservation of momentum

$$\vec{\boldsymbol{p}}_n = \vec{\boldsymbol{p}}_d - \vec{\boldsymbol{p}}_p. \tag{2.36}$$

From the above equation, the magnitude of the transferred neutron can be determined using the cosine rule

$$\vec{\boldsymbol{p}}_n^2 = \vec{\boldsymbol{p}}_d^2 + \vec{\boldsymbol{p}}_p^2 - 2\vec{\boldsymbol{p}}_d\vec{\boldsymbol{p}}_p \cos\theta. \tag{2.37}$$

Indeed direct reactions are peripheral by their nature, the projectile interacting with the loosely bound surface nucleons of the target nucleus. The angular momentum transferred, $\vec{\mathbf{l}}_n\hbar$ must be less than $\vec{\boldsymbol{p}}_n R$, where R is the impact parameter at which the neutron capture is expected to take place. Hence

$$(l_n + \frac{1}{2})^2 \leq \vec{\boldsymbol{p}}_n^2 R^2, \tag{2.38}$$

$$\vec{\mathbf{L}}^2 = l(l+1)\hbar^2 = R^2\vec{\boldsymbol{p}}_n^2\hbar. \tag{2.39}$$
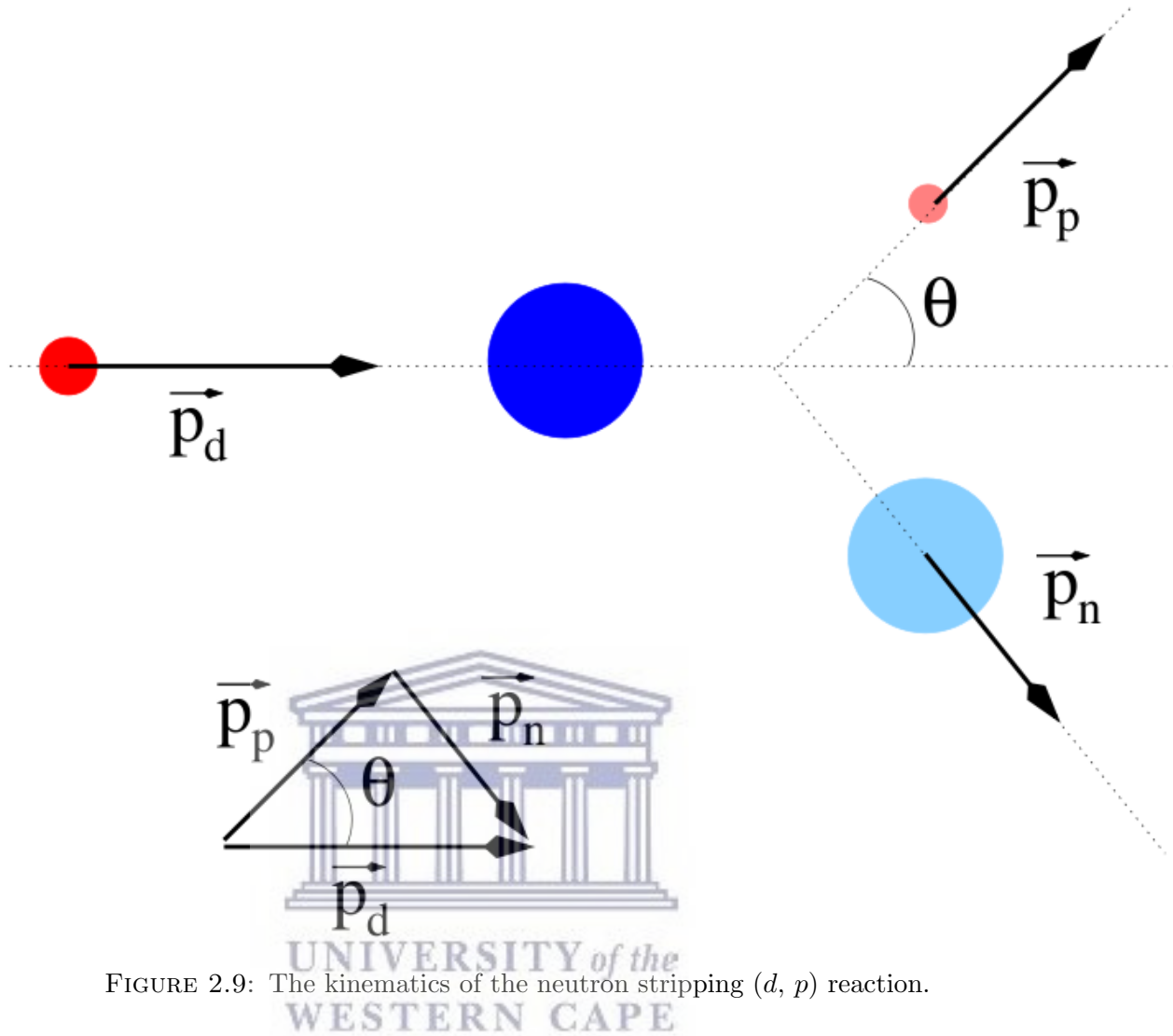
FIGURE 2.9: The kinematics of the neutron stripping (d, p) reaction.

The above equations imply a relationship between the angular momentum l transferred in the reaction and the angle of emission θ of the products

$$\frac{l(l+1)\hbar^2}{R^2} = \vec{\boldsymbol{p}}_d^2 + \vec{\boldsymbol{p}}_p^2 - 2\vec{\boldsymbol{p}}_d\vec{\boldsymbol{p}}_p \cos\theta. \tag{2.40}$$

Each orbital angular momentum transfer in the reaction can now be associated with a peak in the angular peak distribution. The angular distribution, however, is not sensitive to the value of the total angular momentum, j, transferred (i.e. it does not distinguish between the two possible values, $j = l \pm \frac{1}{2}$). To obtain that sensitivity in the (d, p) reaction, one needs to use a polarized deuteron beam and measure the asymmetry of the produced protons.

2.8.1.2 Two-nucleon transfer reactions

Direct reactions where two or more nucleons are transferred are potentially more useful as spectroscopic tools since they are sensitive to correlations in nuclear wave functions. Just like in the single-nucleon transfer, the angular distribution for two-nucleon-transfer reactions is characterized by the orbital angular momentum that is transferred. In this case, the angular momentum is carried by the pair of nucleons, and many different configurations of the two nucleons can contribute to a given angular momentum transfer.

The transfer of two nucleons depends not only upon the individual motions of the two nucleons but also upon the correlation between those motions. Large cross-sections can be produced if there is constructive coherent correlation between the two transferred nucleons and also if nucleons are transferred between similar states. For example, the two protons stripped-off in a $(^3\text{He}, n)$ reaction must be found close together, with their spins anti-parallel, in a relative space-symmetric $S = 0$ *singlet* spin state (because of the *Pauli exclusion principle*) and is in angular momentum $L = 0$ [71]. Also, assuming that you have a one-step transfer process. In such cases, only natural-parity states are populated in the residual nucleus. The J^π of the final states are unambiguously inferred by L-transfer identification, with $J_f = L$ and $\pi_f = (-1)^L$. However, two-nucleon transfer reaction mechanisms are not as simple as that: the strong Coulomb field will give strong excitations of low-lying states, for example of the 2^+ states in semi-magic nuclei. The strong Coulomb field will inelastically excite the 2^+ states but there are enhanced pair transfers with multipolarity 0 and 2 between these states and ground states.

Two nucleon transfer goes preferentially to states that exhibit strong pairing correlations in their wave functions. It was pointed out in 1962 that strong monopole pairing will concentrate almost all of the two nucleon transfer strength into the ground state of the residual nucleus [77]. Indeed, the study of these reactions is typically to investigate the strength of the correlations and pairings between nucleons in the single-states of the independent-particle shell model. There is a large amount of data already available for the stripping and pickup of two neutrons by use of (t, p) and (p, t) reactions. With regards to two-proton stripping by the $(^3\text{He}, n)$ reactions very limited data is available. There are almost no data of spectroscopic values for two-proton pickup, because of the experimental difficulties of the $(n, {}^3\text{He})$ reaction for light-ion reactions.

Direct transfer reactions are often analysed using the Distorted Wave Born Approximation (DWBA) method. In an example case of single-nucleon transfer in the previous Section, A(*d*, *p*)B a neutron is stripped from the deuteron projectile. The angular distribution of the outgoing proton is measured and compared with DWBA calculations to determine the orbital to which the stripped neutron has been placed. This is the case with two-nucleon transfer reactions also, except that the transferred angular momentum is carried by a pair of nucleons. The first step to model the collision of two nuclei would be to introduce a simple one-body potential, such as the *optical potential* [78] that describes some average features of collision, namely, the elastic scattering and the gross absorption of the incident flux into other, nonelastic channels. This provides a stepping stone upon which a more detailed description of the collision may be built, such as the Distorted Wave Born Approximation.

2.8.1.3 The Optical Model Potential

The basis of the *optical model* was established by Feshbach and his co-workers in 1953 [79]. The model has proved to be a successful way of describing elastic scattering of light nuclides from complex nuclei. In the model, the assumption is made that the complicated nuclear interaction between a scattered nucleon (or light nucleus) and a target nucleus can be approximated by a central complex potential representing the average interaction potential $U(r)$, with r being the distance between the center of mass of the two nuclei. This potential includes both an attractive real term and a negative imaginary term.

The model of elastic scattering is constructed by analogy with the scattering of light by a refracting and absorbing sphere. The collision then occurs as between a particle and a potential well; the real part of the potential refract the incident particle waves and the imaginary part represents an absorption of incident particles i.e. it accounts for the loss of flux during the actual scattering. In the case of a two-proton transfer, this approximation is equivalent to a proton pair being diffused with an absorbing well. The most widely used functional form for the optical

model potential is [80]

$$
\begin{aligned}
U(r) = & - V_r f_{\text{WS}}(r, R_0, a_0) - i W_v f_{\text{WS}}(r, R_w, a_w) \\
& - i W_s (-4 a_w) \frac{d}{dr} f_{\text{WS}}(r, R_w, a_w) \\
& - 2(V_{\text{SO}} + i W_{\text{SO}}) \left(\frac{-1}{r} \frac{d}{dr} f_{\text{WS}}(r, R_{\text{SO}}, a_{\text{SO}}) \vec{l} \cdot \vec{s} + V_C \right),
\end{aligned}
\tag{2.41}
$$

where

* V_r is real and represents a nuclear well depth, W_v and W_s represent the absorption effect or, in another way, the disappearance of particles from the elastic channel. W_v is responsible for the absorption in the whole volume of the nucleus whereas W_s, built from the derivative of the function f_{WS}, acts specifically in the region close to the nuclear surface;

* V_{SO} and W_{SO} are the real and imaginary part of the spin-orbit potential. The spin-orbit term enables the polarization of the scattered particle to be calculated;

* V_C is the Coulomb interaction if the incident particle is charged and is given by

$$
V_C(r) =
\begin{cases}
\frac{Z_P Z_T e^2}{r} & \text{if } r \geq R_C, \\
\frac{Z_P Z_T e^2}{2 R_C} \left(3 - \frac{r^2}{R_C{}^2} \right) & \text{if } r \leq R_C,
\end{cases}
\tag{2.42}
$$

where Z_P and Z_T are charge numbers of the projectile and target nuclei, respectively, R_C is the *Coulomb barrier radius* that separates the regions of nuclear and Coulomb forces; and

* f_{WS} is the Woods-Saxon form factor, given by the Equation 2.4.

2.8.1.4 The distorted wave Born approximation (DWBA)

In transfer reactions, the quantities of interest that are calculated are the angle integrated cross section σ_{tot} and the differential cross-section $\frac{d\sigma}{d\Omega}(\theta)$ for populating a specific state. The distorted wave Born approximation (DWBA) has been applied to the description of transmutation reactions induced by projectiles of low and medium energy. In the DWBA approach, the transfer reaction is treated as a low strength interaction acting on the incoming wave-function. The wave-functions for

the initial and final elastic scattering states are approximated by using the optical model. The differential cross section for the (τ^1,n) reaction, is given by [81, 82]

$$\frac{d\sigma}{d\Omega} = \frac{\mu_\tau \mu_n}{(2\pi\hbar^2)^2} \frac{k_n}{k_\tau} \frac{1}{(2S_\tau + 1)(2J' + 1)} \sum_{\sigma_\tau \sigma_n M M'} \left| T_{JM\sigma_n, J'M'\sigma_\tau} \left(\vec{k}_\tau, \vec{k}_n\right) \right|^2, \quad (2.43)$$

where $\mu_\tau(\mu_n)$ and $\vec{k}_\tau\hbar(\vec{k}_n\hbar)$ are the reduced mass and relative momentum in the entrance and exit channel, respectively. We are assuming that both the projectile and the target nuclei are unpolarized. So we sum and average over the contributions from different possible spin substates for the ^{3}He and neutron as well as the target and residual nucleus spin projections, M' and M, respectively. Also, we must average the cross-section over the spin of, the incident ^{3}He and target nucleus J', and also scale by some constants and phase space parameters, i.e. μ_τ and μ_n, and the wave numbers k_τ and k_n. The transition matrix $T_{JM\sigma_n, J'M'\sigma_\tau}\left(\vec{k}_\tau, \vec{k}_n\right)$ gives the probability amplitude for the reaction, and is written

$$T_{\beta,\alpha} = \langle \psi_\beta{}^{(-)} \Phi_\beta | V_{\beta,\alpha} | \Psi_\alpha(\xi_\alpha) \rangle, \quad (2.44)$$

where α contains the set of entrance channel quantum numbers of both the target and the projectile, as well as the kinematic factors in that channel. The $\Psi_\alpha(\xi_\alpha)$ (in the entrance channel) is the wave-function for ^{3}He + A-body target nucleus with ξ_α representing all possible coordinates such as the spin, energy, displacement of the projectile to the target, etc. In the exit channel, β contains the quantum numbers and kinematic factors present with $\psi_\beta{}^{(-)}$ the outgoing wave-function for the emitted neutron, including information regarding both its motion and its internal interactions. Φ_β represents the wave-function of the residual nucleus (A + 2) after the transfer of the two protons. Lastly, $V_{\beta,\alpha}$ is the interaction potential coupling the entrance and exit channels.

Unfortunately, some approximations need to be made as this is an exact many-body problem. Firstly, the assumption is that, for the $(^3$He, $n)$ reaction the two protons that are stripped-off the projectile are transferred into pure single-particle shell model states. Also, that the target nucleus is in its ground state and that the transfer takes place directly in a single-step from the elastic channel to the residual channel. This forbids other modes of excitation, such as collective modes, single-particle excitations, etc. during the transfer process. This gives

---

[1]τ is used to represent ^{3}He

the standard distorted-wave Born approximation for transfer reactions [83]. The following approximations are made for the entrance and exit channels:

2.8.1.5 Entrance channel α

$$|\Psi_\alpha(\xi_\alpha)\rangle \rightarrow \left|\Phi(A)_{J'M'}\sum_{\sigma'_\tau}\chi^{(+)}{}_{\tau\sigma'_\tau\sigma_\tau}(\vec{k}_\tau,\vec{r}_\tau)\phi_{\tau\sigma'_\tau}(\vec{\rho},\vec{r})\right\rangle, \qquad (2.45)$$

where $\Phi(A)_{J'M'}$ represents the wave-function of the target nucleus, A in its ground state. The $\chi^{(+)}{}_{\tau\sigma'_\tau\sigma_\tau}(\vec{k}_\tau,\vec{r}_\tau)$ is the *distorted* wave-function (plane plus spherical scattered waves, with the (+) superscript representing the incoming wave) for the projectile, ^{3}He with initial and final spin projections σ and σ'_τ. A distorted wave is a solution to the Schrödinger equation for a plane wave which has been scattered by an appropriate Optical Model Potential. The last function, $\phi_{\tau\sigma'_\tau}(\vec{\rho},\vec{r})$ is a wavefunction describing the internal structure of the ^{3}He with $\vec{\rho}$ and $\vec{r}$ its internal spatial coordinates. The ^{3}He internal wavefunction may be decomposed into the product of several uncoupled components;

$$\phi_{\tau\sigma'_\tau}(\vec{\rho},\vec{r}) = \sum_{\sigma'_n\sum_z}(S_n\sigma'_nS\sum_z|S_\tau\sigma'_\tau)\phi^{2p}(\vec{r})f(\vec{\rho})\phi_{n\sigma'_n}X_{p\sum_z}(S_1,S_2). \qquad (2.46)$$

In this function, $S_n, \sigma'_n, S, \sum_z, S_\tau$ and σ'_τ represents the spins and spin projections of the neutron, proton pair and helium respectively. The $\phi^{2p}(\vec{r})$ is the wavefunction describing the motion of the two protons relative to one another. The $f(\vec{\rho})$ is a wavefunction describing the motion of the neutron relative to the centre-of-mass of the proton pair.

2.8.1.6 Exit channel β

$$|\psi_\beta\Phi_\beta\rangle = \left|\Phi(A,1,2)_{JM}\sum_{\sigma'_n}\chi^{(-)}{}_{n\sigma'_n\sigma_n}(\vec{k}_n,\vec{r}_n)\phi_{n\sigma'_n}\right\rangle, \qquad (2.47)$$

where $\Phi(A,1,2)_{JM}$ is the wavefunction for the residual nucleus, with two-stripped protons, an (A+2)-body nucleus. The $\chi^{(-)}{}_{n\sigma'_n\sigma_n}(\vec{k}_n,\vec{r}_n)$ is the distorted wave-function for the outgoing neutron, and $\phi_{n\sigma'_n}$ is the wavefunction describing the internal structure of the neutron (i.e. its spin). An authoritative source on this Distorted Wave Born Approximation (DWBA) treatment for direct two-nucleon transfer reactions could be found in ref. [82].

2.8.1.7 The Coupled Channel Born Approximation (CCBA)

However, for collective nuclei the inelastic processes frequently are stronger than the interaction for transmutations. In such cases, a higher DWBA or coupled-channel calculation is necessary. The CCBA provides a more complete description of reaction processes for transitions between nuclei showing strong collective effects. The theory includes multi-step processes ignored by the DWBA treatment, by allowing reactions to be induced by projectiles scattered from inelastic states in the incident channel.

2.8.2 Compound Nuclear Reactions

The compound-nucleus hypothesis, first proposed by Neils Bohr [84] is probably the most often used concept for the description of nuclear reactions. In the model, Bohr divides a nuclear reaction in two steps; the formation of a compound nucleus (entrance channel) and its one-step decay process (exit channel). The two nuclei come into close contact and form an intermediate combined system, the compound nucleus, which is not stable on a macroscopic time-scale in which the nucleons interact strongly with each other. This can be written schematically as

$$a + A \rightarrow C^* \rightarrow B^* + b, \tag{2.48}$$
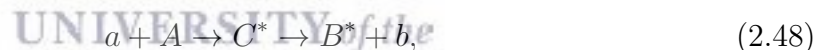
where a is the projectile, A the target nucleus, C^* is the excited compound nucleus, and b, B^* are the reaction products after the compound nucleus decay. The excited B^* nucleus will decay either through particle emission, if there is still sufficient excitation energy, or γ rays. The energy carried in by the projectile is shared more or less stochastically among many configurations. In this transit period, the system usually has a structure of compound states and are assumed to be in equilibrium with each other. The equilibrized system has a fairly long lifetime compared to the "fly-by time" of the projectile, in the absence of interactions. At this point, the system could either fission or evaporate light particles (such as n, p, *tritons*, etc.) to quench its excessive energy. The final break-up of the compound nucleus is considered to be independent of the mode of formation. It is assumed that the decay of the compound nucleus depends only on the excitation energy and other good quantum numbers of the compound nucleus. Therefore there exist definite probabilities of decay into each of the exit channels available,

regardless of how the compound nucleus was formed. Hence, being referred to as the *independence hypothesis.*

Neutrons are more favoured to pass through the Coulomb barrier than the charged particles. Unlike direct nuclear reactions, the angular distribution of the emitted particles exhibit a backward-forward isosymmetric distribution in the centre of mass system. However, the total angular momentum is conserved and cannot be "forgotten". The emitted particles carry away some small amount of kinetic energy 1-2 MeV, in addition to the average binding energy of about 8 MeV. The nucleus can also emit gamma-rays, but this decay branch is weak above particle thresholds.

Chapter 3

EXPERIMENTS
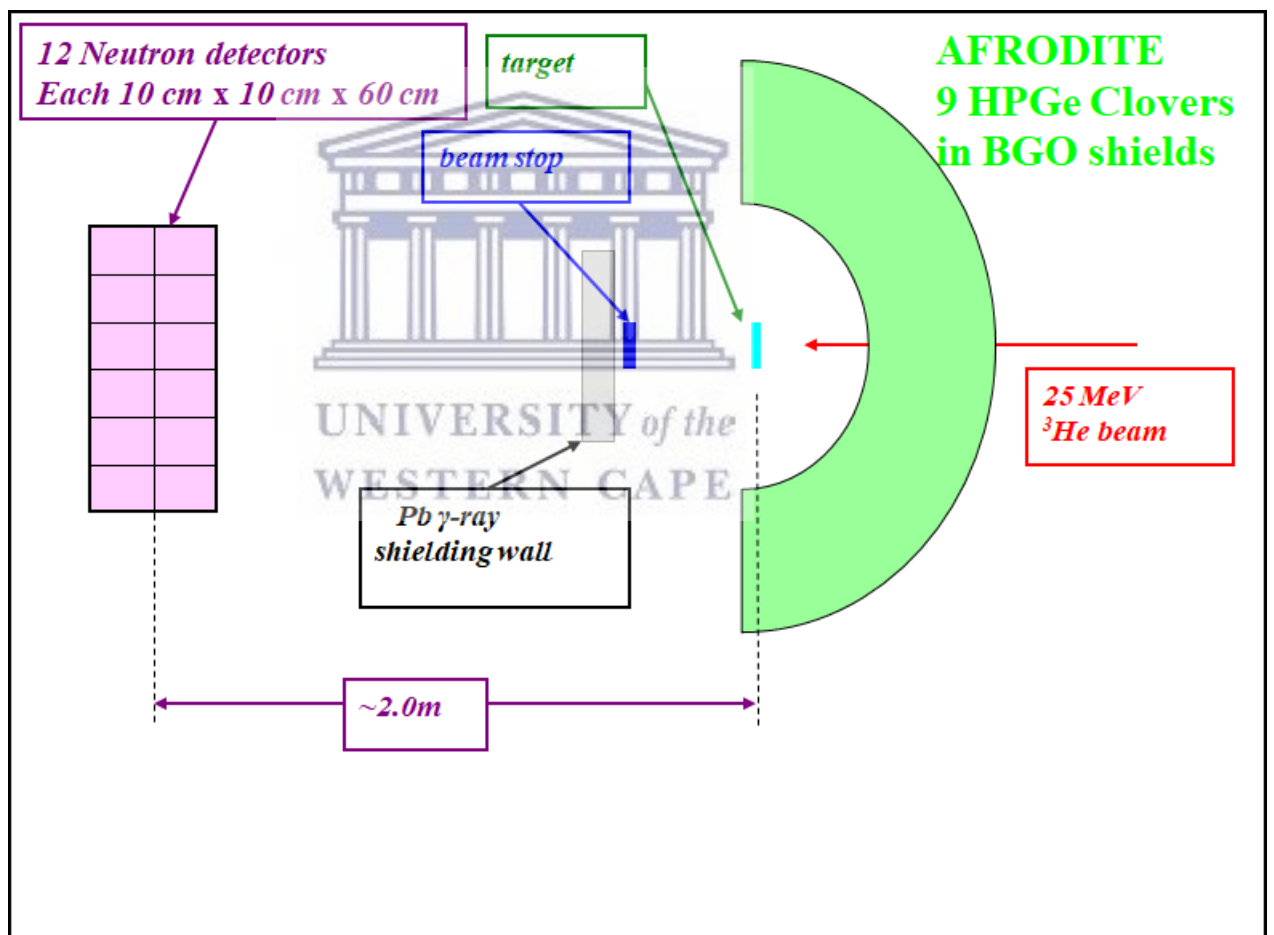
FIGURE 3.1: A schematic diagram of the AFRODITE coupled to the neutron wall.

The γ ray spectrometer, AFRODITE [85], was coupled with an ancillary neutron detector composed of a set of 12 plastic scintillator detectors, see the schematic

TABLE 3.1: Thickness of the 4 different targets used listed below.

Target	Thickness [mg/cm^2]
^{108}Pd	5
^{110}Pd	1.3
^{114}Cd	3
^{115}In	3.6

diagram Fig. 3.1. Using the *time-of-flight* (t-o-f) technique, this detector set-up allows us to detect γ rays as well as fast neutrons from a direct reaction channel. The measurements of the t-o-f technique make use of the fact that γ rays travel at the speed of light while neutrons do not. The time-of-flight method requires at least one detector if the detected radiation comes from a nuclear reaction induced by a pulsed beam on a thin target. Measuring the arrival time at the detector relative to the beam pulse enables the speed of the particles to be determined using the following relativistic equation,

$$E_0 = E_n \left(\frac{1}{\sqrt{1 - \beta^2}} - 1 \right), \tag{3.1}$$

$$\beta = \frac{v}{c} = \frac{d}{t} \cdot \frac{1}{c},$$

where d is the distance travelled by the particles, E_0 is the kinetic energy of the neutron and E_n is the neutron rest mass energy. In these experiments, a pulsed beam (pulsed at 350 ns) of ^{3}He particles at 25 MeV energy was used to strip two protons onto targets of ^{108,110}Pd, ^{114}Cd and ^{115}In nuclei. The thickness of each target used in the 4 experiments is given in Table 3.1. The set-up of the experiment was such that, an array of a double wall of twelve 0.6 × 0.1 × 0.1 m^3 of NE-102A plastic scintillators, were placed at 2 m distance from the target, which make a detector solid angle of $\Delta\Omega \approx 0.09$ sr at the target. Each of the scintillator blocks are viewed by photomultiplier tubes at both ends. Only the front wall was used in the analysis due to poor performance of the plastic scintillator detectors (being discoloured) in the second row of the wall.

The (^{3}He, n) reaction has positive Q-values ranging between 0 and 10 MeV, see Table 3.2. However, for reactions with more than 1 neutron emitted, the Q-values are negative. Thus for 25 MeV beams of ^{3}He on the various targets used, the direct reaction neutrons will have energies between 25 and 35 MeV. From Equation 3.1, this translates to a velocity of about 76 mm/ns taking about 27 ns

TABLE 3.2: Q-values for (^{3}He, n) reactions on the different targets listed below.

(^{3}He,n) on target	Q-value [MeV]
^{108}Pd	+7.687
^{110}Pd	+9.104
^{114}Cd	+8.371
^{115}In	+5.963

to travel a distance of 2.0 m. This separates the high flux of competing statistical neutrons with energies less than 6 MeV at mb of cross-section (see in Chapter 5 for PACE4 calculations for different reaction channels) from the direct reaction neutrons, which have energies greater than 10.0 MeV (at < 1b cross-section). As the velocity of neutrons is proportional to $\sqrt{E_n}$, it follows that the direct reaction neutrons have about twice the velocity of the statistical neutrons and may be separated from them by time-of-flight measurements over the relatively short distances of 2 m. With this detector set-up i.e. the neutron detectors positioned at less than 10° to the beam line, the geometry of the apparatus is designed to pick out $L = 0$ two proton transfers where the emitted neutron angular distribution is peaked around a scattering angle of 0°. This geometry helps the selection of direct reaction neutrons as the fusion evaporation neutrons are emitted isotropically in the centre-of-mass of the experiment. The spin of the final states populated will have the same spin as the target nucleus as the angular momentum transferred is $L = 0$.

In these reactions, the main fusion evaporation channel in ^{108,110}Pd(^{3}He, $3n\gamma$)^{108,110}Cd, ^{114}Cd(^{3}He, $3n\gamma$)^{114}Sn and ^{115}In(^{3}He, $3n\gamma$)^{115}Sb is at least 10^3 stronger than the (^{3}He, n) for the different target's direct reaction channels. So the energy of the neutrons and time-of-flight is the sensitive technique that has been employed to efficiently select the channels of interest, ^{108,110}Pd(^{3}He, n)^{110,112}Cd, ^{114}Cd(^{3}He, n)^{116}Sn and ^{115}In(^{3}He, n)^{117}Sb.

3.1 Particle-γ Coincidence Measurement

Beam instabilities, electronic jitters, delays in the electronic circuits, cable lengths, etc., can result in uncorrelated timing differences in the different crates of clover and neutron detectors. It is important that detectors are synchronised in time so that the information from all detectors, the AFRODITE and neutron wall,
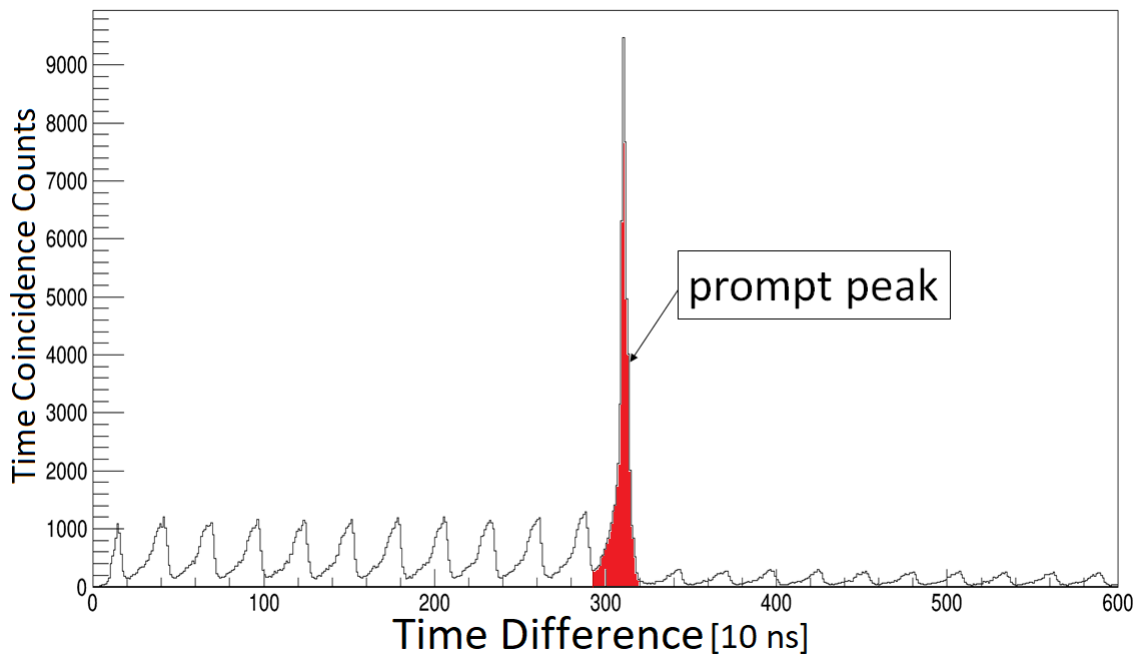
FIGURE 3.2: Time-correlated spectrum from time-stamp difference between RF and clover detectors, generated during the ^{108}Pd(^{3}He, n)^{110}Cd reaction.

is available for a given event. Further, synchronisation is crucial in calculating accurate times of flight. When two or more particles that originate from the same reaction vertex are detected simultaneously, a coincident measurement has occurred. Coincidence measurements are generally used to suppress experimental backgrounds and isolate exclusive reaction channels. Coincidence particles were identified by starting a time measuring device, a *Time-to-Amplitude Converter* (TAC) with a signal originating from the neutron detector and stopping it with the *Radio Frequency* (RF) cycle of the *Separated Sector Cyclotron* (SSC). The time-to-amplitude converter produces an output whose amplitude is proportional to the time interval between the start and stop signal and carries the neutron beam time-of-flight information. The TAC analogue pulse output produced is then sent to an *Analogue-to-Digital Converter* (ADC) in the 100 MHz 16-channel all-digital waveform PIXIE-16 module for data acquisition, see Fig. 3.4.

Initially, time-correlated spectra were generated by taking time-stamp differences between RF and clover, and neutron (see Subsection 3.4.3.1) detectors shown in Fig. 3.2 and 3.3, respectively. Plotting these time difference spectra, a clear correlation between γ rays emitted by the reaction partners (*prompt peak*) and those from random background can be seen. The γ ray spectra taken during the random time gate are then subtracted from those taken during the prompt time
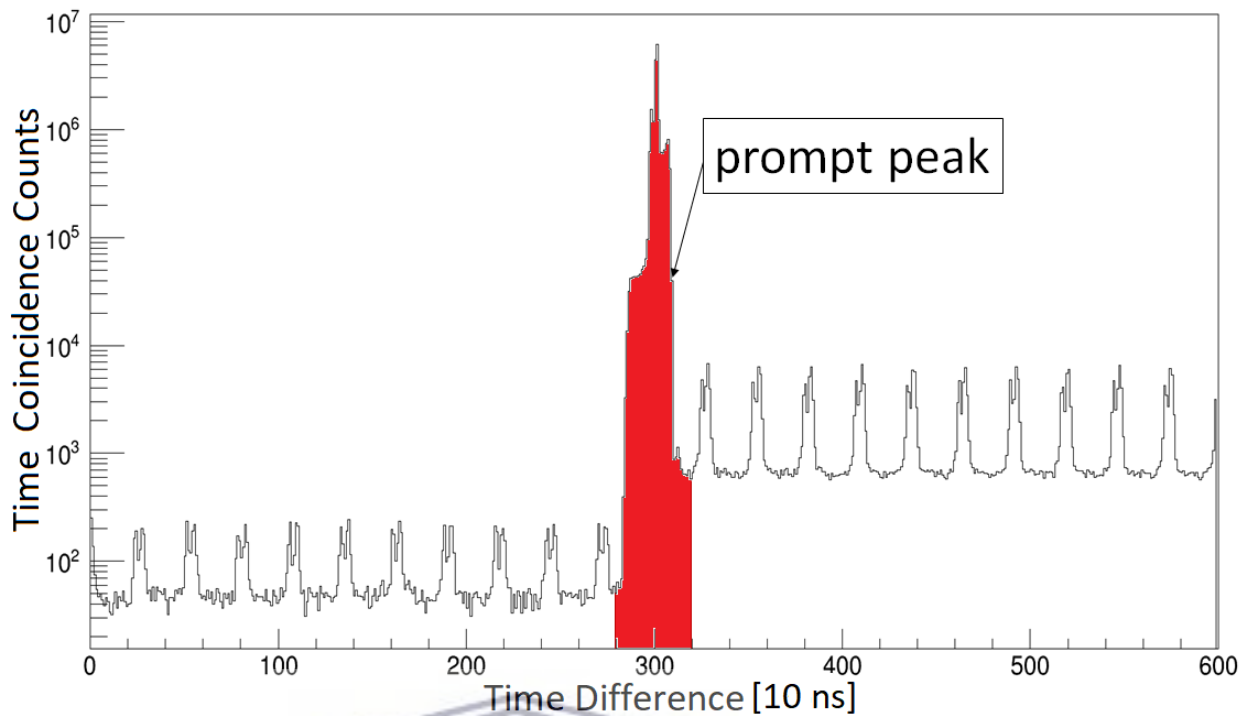
FIGURE 3.3: Time-correlated spectrum from time-stamp difference between RF and neutron detectors (y-axis in log-scale), generated during the ^{108}Pd(^{3}He, n)^{110}Cd reaction.

peak. Note that the random time gate is much longer than the prompt peak. The corresponding spectra will therefore be weighted with $\frac{t_{prompt}}{t_{random}}$ before subtraction.

3.1.1 Electronic set-up for the neutron wall

In Fig. 3.4, it is shown that the analog signal coming from the neutron detectors is split into two, one signal was sent directly to the PIXIE-16 module and the other was passed to the *Timing-Filter-Amplifier* (TFA) module. The TFA amplifies the signal to a reasonable level. It is also important for some additional signal shaping in order to achieve the best timing resolution. The output of the TFA is a bipolar pulse that was fed to the *Constant-Fraction Discriminator* (CFD). When an analog signal is passed to a CFD, the module outputs a logic signal only if the amplitude of the analog signal exceeds a user controlled value. In this way, low-amplitude signals caused by electronic noise and background radiation should be suppressed. From the CFD the analog signal is then passed to the delay box through a *Coincidence Unit* (CU). The coincidence unit is a device that can make a logical AND or OR of the input logic signals. In the OR mode, the CU gives an
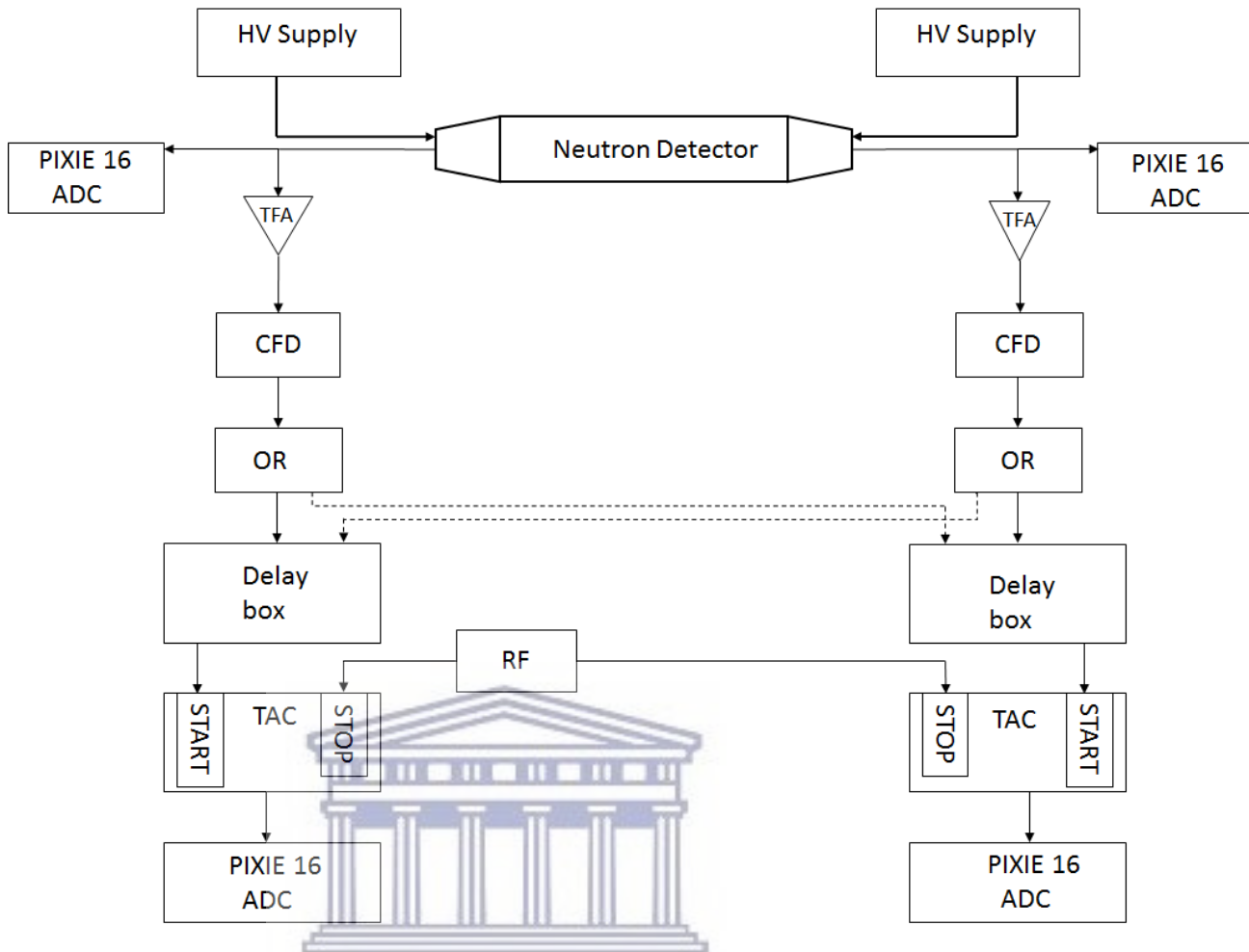
FIGURE 3.4: A schematic diagram of the electronic set-up for the neutron wall.

output signal as soon as any of the input signals is received. The delay box can be used to introduce a delay in the signal pulse. This is achieved easily by using cables of differing length. The analog signal from the delay box is then passed to the TAC module.

3.2   Neutron Detection

Neutrons are interesting not only as the particles themselves, but also as a useful tool for nuclear structure research, radiochemical analysis, nuclear medicine, neutron imaging (i.e. neutron radiography), and other applications. The property of the neutron (having no charge) makes it difficult to detect, as well as to determine its energy. They interact with matter mainly in two ways. Firstly through radiative neutron capture i.e. $n + (Z, A) \longrightarrow y + (Z, A + 1)$, especially the low-energy neutrons. Generally, the cross section for neutron capture goes approximately as

$\approx 1/v$ where v is the velocity of the neutron. Absorption is most likely, therefore, at low energies. Secondly, for fast and higher energy neutrons, the energy conversion process is elastic scattering with light nuclei (i.e. protons in hydrogen) in which case the energy of the neutron is (partially) transferred to the protons, which in turn can produce scintillation light. Using the above mentioned principle, fast and high energy neutrons can be detected in any organic (plastic or liquid) scintillator. Neutrons are classified as fast if they have energies between a few hundred keV and a few ten's of MeV and high energy if their energy is above 100 MeV.

Situations where neutrons can be detected free from any γ ray background are very rare due to the fact that reactions producing free neutrons tend to also produce γ rays. Both of these radiation types are highly penetrating since they are uncharged. Therefore, it is difficult to preferentially "shield" a neutron detector from γ rays. Hence, it is important to be able to distinguish the neutron signature from the γ ray signature in a detector. In practice, three methods are commonly used; "time-of-flight", "zero-cross-over (ZCO)" and "digital-charge comparison". A combination of these techniques may also be employed simultaneously. In this experiment, the time-of-flight method was used to separate the fast neutrons from the γ rays, and also from the slow fusion evaporation neutrons, see Fig. 3.5. In this scatter plot, the time-of-flight is plotted against the energy of the neutrons. The total energy deposited in the plastic scintillator is given by

$$E = \sqrt{E_L E_R},$$

(3.2)

where E_L and E_R are the photomultiplier tube (PMT) signals from left and right sides, respectively. The time-of-flight of neutrons and γ rays between the target and the detector segments is determined as the difference between the constant fraction discriminator time and a common time reference signal. The RF signal from the separated sector cyclotron beam pulsing system was used as the reference time. The RF period can be deduced from the time difference spectra, see Fig. 3.2 and Fig. 3.3; The beam burst separation is 270 ns.

3.2.1   Scintillators

The scintillation detector is one of the most versatile radiation and particle detection devices in nuclear and particle physics. It uses the fact that certain materials, when struck by a neutron, photon or charged particle, emit a small flash of light.
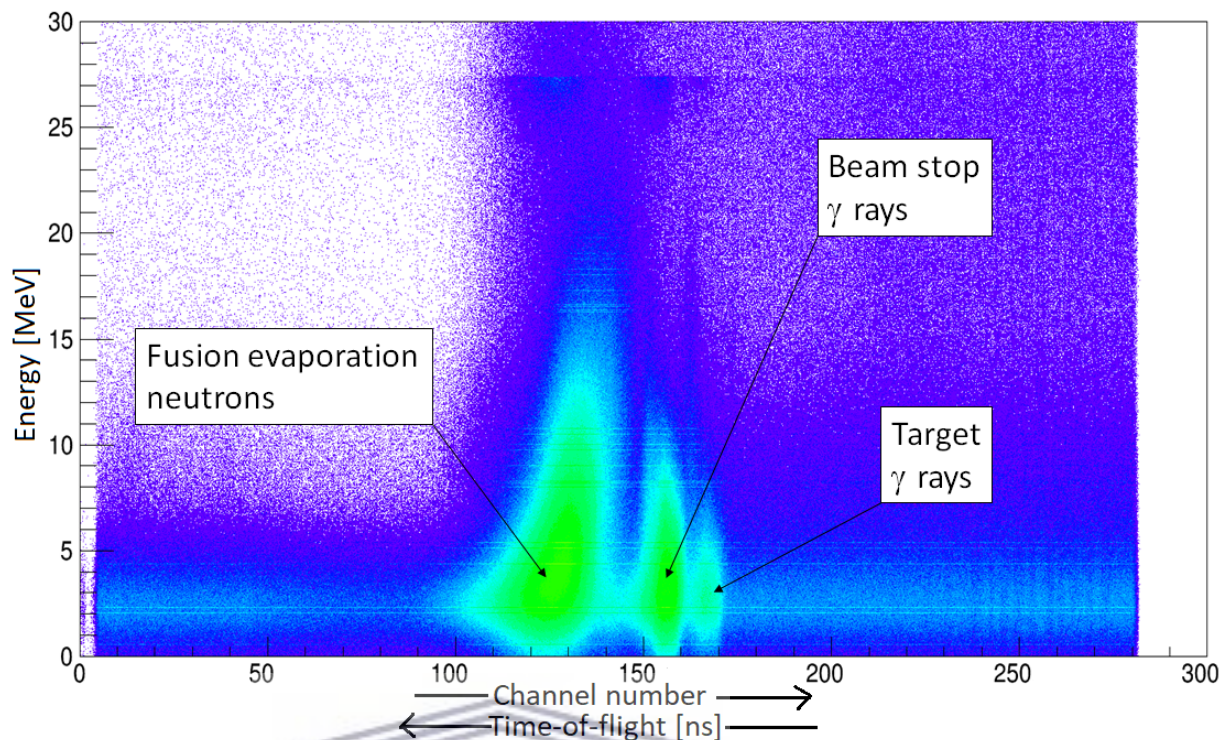
FIGURE 3.5: Scatter plot of the time-of-flight mapped against the energy of the neutrons and γ rays.

Dealing with such small signals is one of the main challenges in designing detectors and instrumentation for nuclear physics experiments. The light travels down the scintillator bar to the photomultiplier tubes, where it is converted into a usable signal. Each PMT on each bar outputs an energy and time signal. Direct coupling of a flat panel scintillator element to a circular photomultiplier is optically inefficient, hence a cone shaped light-guide made of plexiglass material was used to connect them, see Fig. 3.6. Generally, a good detector scintillator material should have the following features:

- The material must be transparent to the wavelength of its own fluorescent radiation and be free from turbidity or variations in the index of refraction.

- It must also have a high efficiency for conversion of exciting energy to fluorescent radiation.

- Its index of refraction should be near that of glass to enable efficient coupling of the scintillation light to the photomultiplier tube.

Plastic scintillators have a lower light output than most inorganic scintillators. They are characterised by fast decay time of about 2-3 ns of the light pulse.
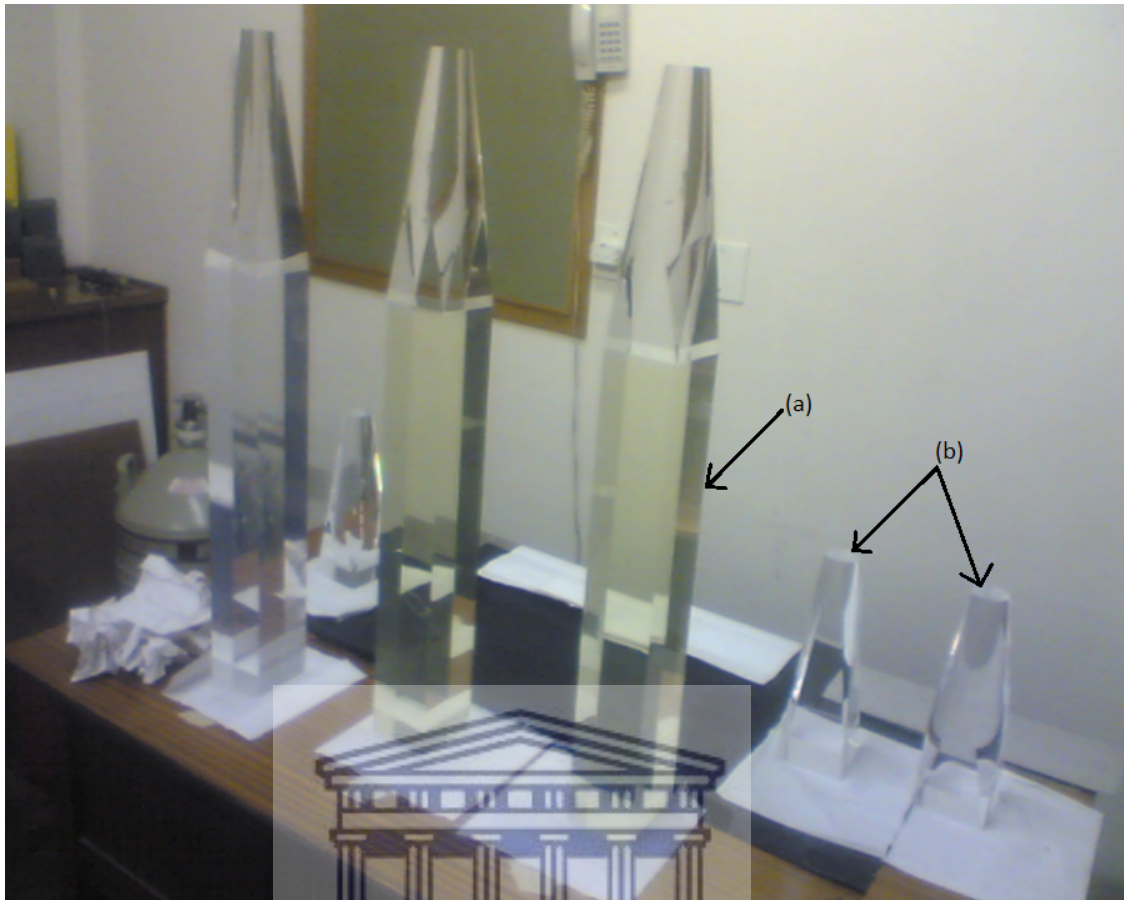
FIGURE 3.6: (a) Plastic scintillator detector, (b) light guide glass.

Another advantage is that plastic scintillators are non-hygroscopic and are easy to fabricate into any shape. However, with liquid scintillators, their lack of a solid structure makes them robust against radiation damage effects when exposed to intense radiation. Also, liquid scintillators are often cheap compared to other detectors.

3.2.2 Photomultiplier tubes

Scintillator detectors would not be useful without the device such as photomultiplier tube to convert the weak light of the scintillation pulse into a corresponding electronic signal. The light is collected on the front face of a multiplier tube, where the light photons are absorbed on a photocathode. The photons from the scintillator transfer their light energy to the electrons in the photocathode and free the electrons in the photo-emissive material. The electrons are then accelerated through a series of electrodes, the *dynodes* under a high potential difference
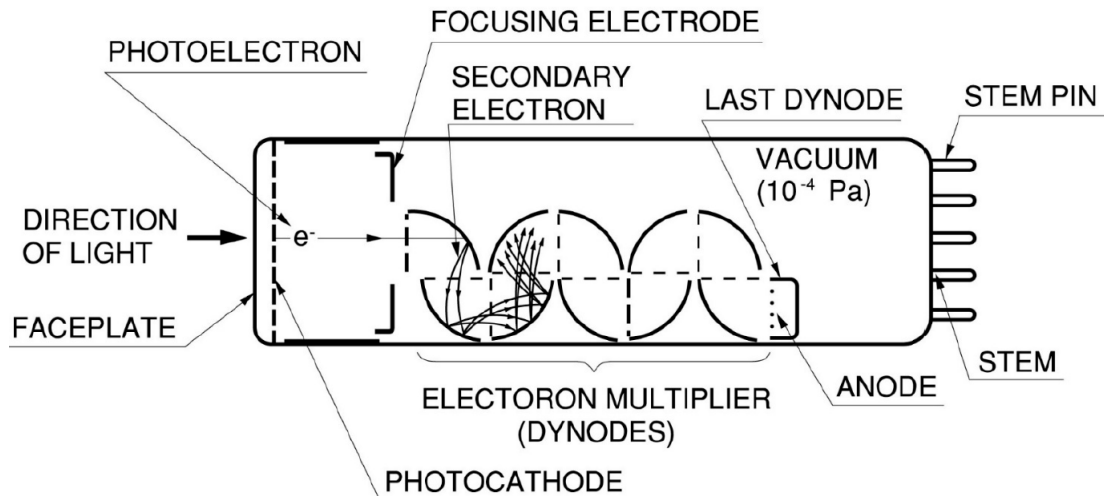
FIGURE 3.7: Basic design of a photomultiplier tube [9].

greater than the cathode potential. When electrons hit these dynodes, more and more electrons are released. This multiplication chain of electrons is necessary to create a detectable pulse at the final stage of the PMT. These electrons are collected as current at the *anode* and passed to the electrical connectors on the base. The light signals are converted into a current pulse without adding a large amount of noise to the signal. A graphical representation of a photomultiplier tube is shown in Fig. 3.7.

3.2.3 Cosmic-ray muons for calibration of detector

Cosmic-ray muons are produced by the interaction of cosmic rays with the Earth's upper atmosphere. The shower of particles produced is attenuated in the atmosphere, and only muons tend to survive at sea level. The average energy of muons reaching sea level is about 2 GeV [86].

Muons are charged particles and lose energy through Coulombic interactions as they traverse through matter. The energy is progressively absorbed by ionizing the matter it passes through. The average energy loss rate in matter for singly charged particles travelling close to the speed of light is approximately 2 MeV per g/cm^2 (the "interaction length" unit). Some of this deposited energy excites the electrons of the fluorescent molecules. Upon radiative de-excitation, light in the blue region of the electromagnetic spectrum is emitted with a typical decay time of a few nano-seconds.
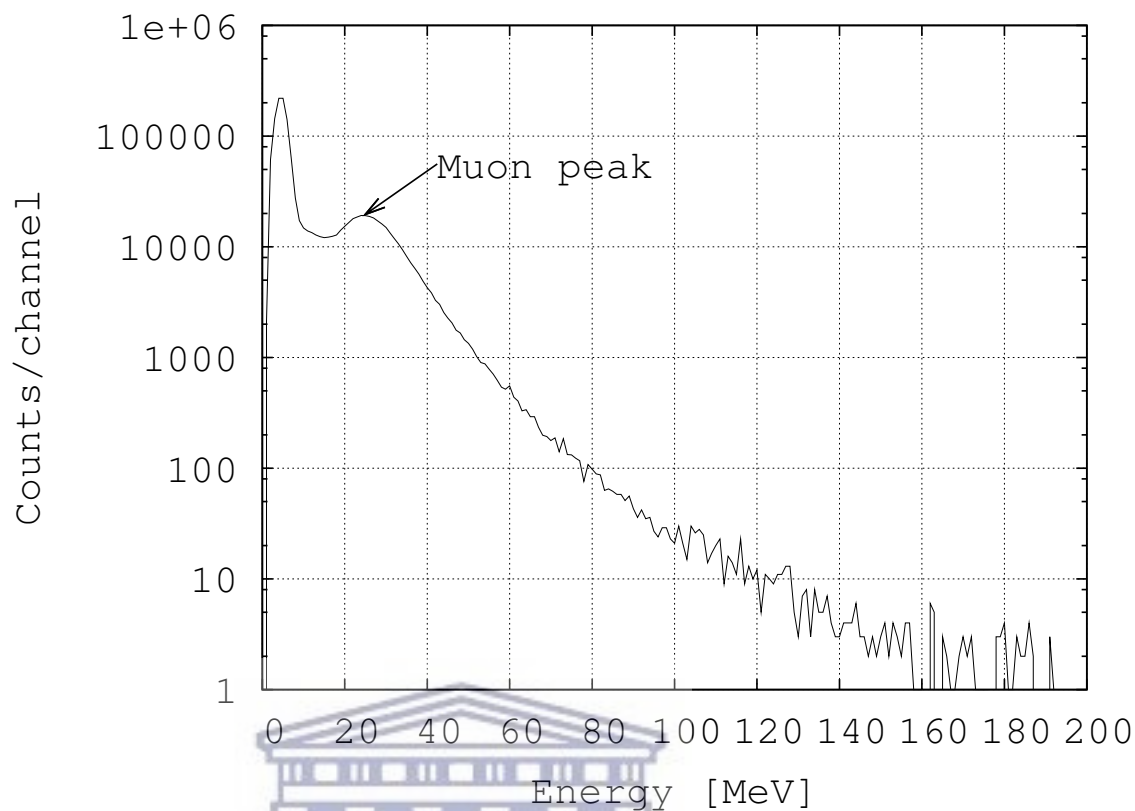
FIGURE 3.8: A calibrated neutron spectrum for a single PMT. The muon peak at 24 MeV is indicated in the figure.

3.2.4 Energy calibrations of the neutron wall

The PMTs in the neutron wall must be gain matched in order to account for differences in light collection and amplification. Cosmic-ray muons are an extremely useful calibration source.

Gain matching is normally done in two steps. The first step is to adjust the bias voltages on the PMTs until their signals are approximately equal. Fig. 3.8 shows an example histogram of the raw spectrum for a single PMT; the broad peak around 24 MeV is from muons interacting with the neutron detector. This peak is fit with a Gaussian for each PMT, and the voltage is adjusted to move the peak value to a same chosen arbitrary channel value for all the PMTs. After adjusting the voltages to approximately line up the muon peaks, further corrections to exactly match the peaks are applied using the sort-code. A linear slope and offset calibration are then applied to place the pedestal at zero and the centroid of the muon peak at 24 MeV.

FIGURE 3.9: A photographic picture of the liquid scintillator detector setup.

3.3 Development of the Liquid Neutron Detector

At the suggestion of Prof. Paul Papka, a 5 L volume neutron detector was developed, filled with the liquid scintillator to measure neutrons in-coincidence with γ rays for future coincidence measurement experiments at iThemba LABS. The detector was fabricated using an aluminum cylindrical housing of 1.2 m length and 0.073 m diameter, see Fig. 3.9. Two Hamamatsu R329 photomultiplier tubes were attached on each end of the pipe. These PMTs contain bialkali photocathodes sealed with borosilicate glass windows. The wavelength sensitivity of the PMTs is in the range 300 nm to 650 nm peaking at 420 nm with a maximum quantum efficiency of 23% in vacuum. The PMTs were operated with a negative voltage of 1500 V and the signals from the anodes were collected in the data acquisition system via a PIXIE-16 electronics module.

The inner surface of the cylinder was anodized with a reflective paint to reduce the amount of light lost by the pipe. The reflective paint makes scintillation photons scatter multiple times from the detector walls, which partially compensates for the relative poor PMT photo-cathode coverage. The detector was filled with the liquid scintillator, Ultima Gold Low Level Tritium (UGLLT) manufactured by
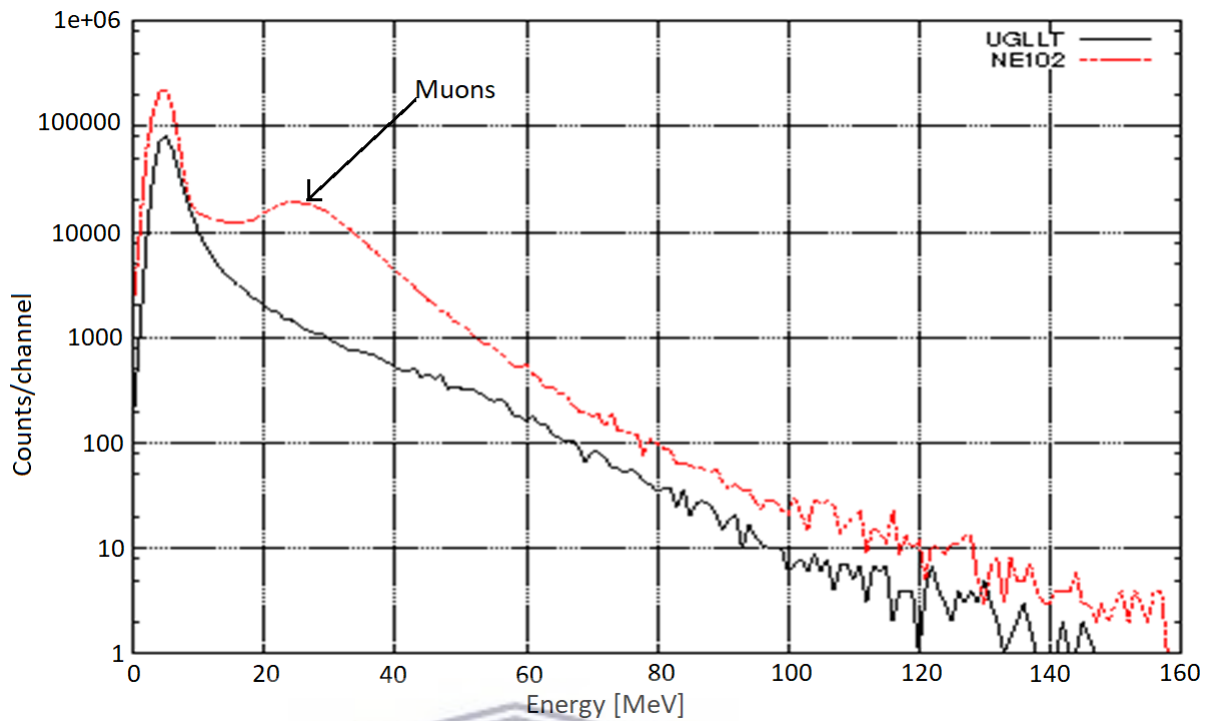
FIGURE 3.10: The calibrated energy spectra of the UGLLT (black) liquid scin-
tillator and NE-102A (red) plastic scintillator.

Perkin-Elmer Inc. [87]. The main solvent in UGLLT scintillator is Di-Isopropyl-
Naphthalene (DIN), which is a chemical compound that is characterized by its
low toxicity, low-vapour pressure and high-ignition temperature. This compound
is also bio-degradable, and is safe to transport and store.

3.3.1   Test results for the new detector

Tests were carried out for the performance of the new detector using muons with
energy of ∼24 MeV and also an americium-beryllium point source whose charac-
teristic neutron peak is at ∼5 MeV. To benchmark the liquid scintillator results,
the plastic scintillator detector NE-102A was used to compare the results. Fig.
3.10 shows the 1-dimensional muon spectra of signals captured by the 2 types of
detectors. The two diagrams show a marked difference with regards to the muon
peak. The muon peak is clearly visible at ∼24 MeV with the plastic scintillator
but not in the liquid scintillator.

A two-dimensional plot of the 2 PMTs for each scintillator is shown in Fig. 3.11.
In Fig. 3.11(a), light attenuation in the liquid scintillator is high. Only events
near the edge of the scintillator bar are able to reach the nearer PMT and light
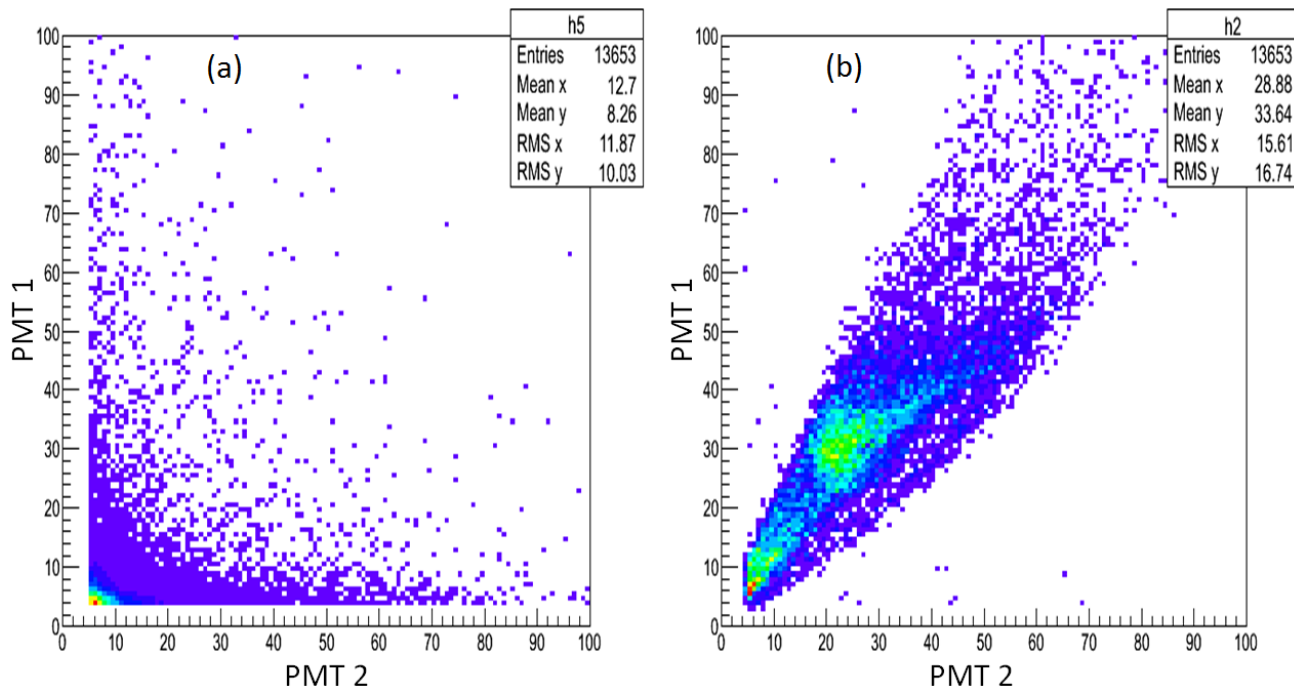
FIGURE 3.11: Two-dimensional plots of events from the 2 PMTs, (a) liquid scintillator and (b) plastic scintillator.

propagation to the opposite end PMT is limited. In the case of plastic scintillators, Fig. 3.11(b), more light is propagated from the middle of the scintillator bar and as such signals are approximately equal to both PMTs.

3.4   Gamma Ray Detection

For γ ray spectroscopy good energy resolution and efficiency are essential. Electromagnetic radiation interacts with matter by transferring all or part of its energy to the atomic electrons of the material. In the energy range from $\sim$10 keV to a few MeV, there are mainly three methods of γ ray interaction that are important in gamma spectrometers: photoelectric effect, Compton scattering and pair production.

Photoelectric effect: This is the process whereby the γ ray interacting with an atom, results in the disappearance of the photon and the displacement of an electron from the atom. The kinetic energy of the outgoing photo-electron is given by

$$E_{e^-} = E_\gamma - E_b, \qquad (3.3)$$

where E_b is the binding energy of the electron and $E_\gamma = hv$. Usually, the interacting electron originates from the most tightly bound K-shell of the atom. The vacancy left in the atomic shell is filled through electron rearrangement and the excitation energy is carried away in the form of a characteristic X-ray (of that particular atom) or *Auger* electrons. The photoelectric effect is the dominant interaction method for low-energy photons (up to 200 keV for Germanium). From theoretical calculations in the expression below 3.4, the cross-section for photoelectric absorption is larger for higher Z materials and it decreases as the γ ray energy increases. This makes high Z materials more desirable when manufacturing γ ray detectors and shields.

$$\sigma_{photon} = constant \times \frac{Z^n}{E^{3.5}}, \tag{3.4}$$

where n is a number between 4 and 5.

Compton scattering: Compton scattering also takes place between a γ ray entering an atom and interacting with any of the orbital electrons in the absorbing material. In this process the incoming γ ray photon is deflected through an angle θ while transmitting some of its energy to the electron, which is called the *recoil electron*. The recoiling electron has the energy of the initial γ ray less the final γ ray energy. The final γ ray energy E', is dependent on the angle of interaction and is derivable from energy and momentum conservation laws to give the well known Compton formula

$$\frac{1}{E'} - \frac{1}{E} = \frac{1}{m_0 c^2}(1 - cos\theta), \tag{3.5}$$

where $m_0 c^2$ is the rest-mass energy of the electron (0.511 MeV) and E is the initial γ ray energy. The probability of Compton scattering per atom of the absorber depends on the number of electrons available in the interaction atom and as such increases linearly with Z_{target}. Compton scattering is the predominant interaction mechanism between $\sim$200 keV and 5 MeV.

In γ ray spectroscopy Compton scattering is not always the most preferable method of interaction. Unlike photoelectric absorption, which deposits its full energy on interaction, in Compton scattering, the γ ray deposits a portion of its energy into the detected electron.

Pair production: This method of interaction can only take place if the γ ray has an energy of at least twice the rest mass of an electron (i.e. $2 \times m_0 c^2 = 1.022$ MeV). Therefore, pair production is strictly confined to high-energy γ ray interactions. The primary photon disappears in the Coulomb field of the nucleus, and its energy goes into rest-mass energy and the kinetic energy of the electron e^- and positron e^+ pair produced. The energy balance of the process is

$$E_\gamma = 2m_0 c^2 + T_{e^+} + T_{e^-}, \tag{3.6}$$

where T_{e^+,e^-} is the kinetic energy given to the positron/electron. In the above expression 3.6 the recoil energy of the atom is neglected. The cross-section for pair production, σ_{pair}, increases rapidly with energy and becomes dominant at energies greater than 5 MeV.

3.4.1 Suppression of Compton scattered γ ray events

In nuclear spectroscopy, the interactions that are of paramount importance are those for which there is complete absorption of the incident γ ray energy. This gives rise to a full energy peak. However, some interactions only result in the partial absorption of the incident photon's energy in the detector. This gives rise to a continuous background in the energy spectrum referred to as the *Compton continuum* and it obscures the useful data, especially weak transitions. Therefore the germanium crystal is normally sheathed in a second detector that can detect these events and can be set to electronically suppress the partial energy pulse and thus veto them.

Bismuth Germanate ($Bi_4 Ge_3 O_{12}$), commonly referred to as BGO, is a scintillation material that is most commonly used as Compton-suppression shielding. Each BGO scintillator element is viewed by an individual photomultiplier tube. The Bi element has a large proton number Z = 83 and high density of 7.13 g/cm^3, which are excellent features for a good quality Compton-suppression shield. The effectiveness of Compton-suppression is generally measured by the peak-to-total (or P/T) ratio which compares the number of counts in well-known photo-peaks versus the total counts collected, see Fig. 3.12. Without the Compton rejection the peak/total ratio is $\sim 20\%$, and for the suppressed spectrometer it is $\sim 50\%$.
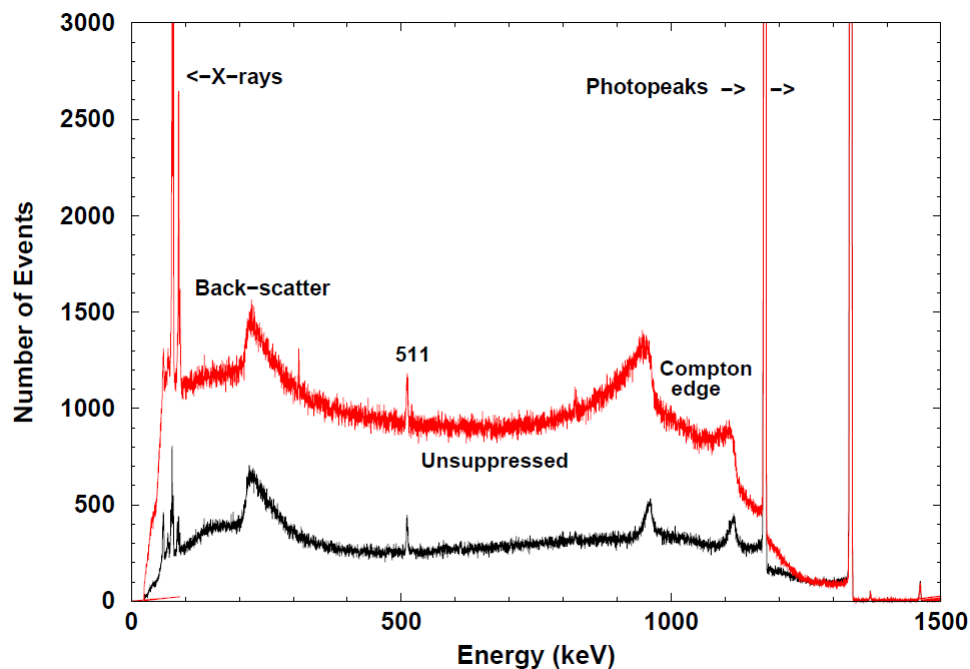
FIGURE 3.12: Spectra from a ^{60}Co γ rays source showing the comparison between the unsuppressed and the suppressed spectrum measured with a clover detector vetoed by a BGO suppression shield [10–12].

3.4.2 Semiconductors

Hyper Purity Germanium detectors (HPGe) are semiconductors. Semiconductors are solid-state materials that possess the properties of crystallinity with a band structure that is neither totally insulating nor conducting. They consist of a periodic atom lattice, with the electrons in the crystal forming *energy bands*. The outermost band in which the electrons are in a bound state is called the *valence band*. In the *conduction band* electrons are freely migrating across the crystal. In between the valence and the conduction band is a forbidden region, *band gap* or *energy gap*. Semi-conductor materials typically have band gaps with energies of about 1-3 eV and ionization energies just slightly greater.

By applying an electric field, the electrons in the conduction band drift to the cathode and the resulting current can be measured. The current depends on the number of electrons in the conduction band. At low temperatures, most electrons are confined to the valence band, they are bound in a covalent bond between the atoms of the semiconductor. Electrons can jump from the valence band to the conduction band by thermal excitation. The current created by thermal excitations is referred to as *leakage current* and it is a major drawback for HPGe detectors as it requires that these detectors be always kept cool to cryogenic temperatures of 77

K. Electrons can also be excited by particles like γ rays interacting with semiconductor. Electrons that jump from the valence to the conduction band leave a hole. A hole can move in the crystal by accepting a bound electron from a neighbouring atom. The movement of the electron-hole pairs through the medium, under the influence of the electric field, (electrons moving toward the positive electrode and holes toward the negative electrode), creates a signal which corresponds to the energy of the interaction that took place.

In reality, semiconductor materials are never infinitely pure. The operation of a semiconductor detector depends on its having either an excess of electrons or an excess of holes. This is achieved through the addition of small amounts of impurities called *dopants* into the semiconductor material such as the germanium. *Acceptor* atoms are impurities with one fewer electron in their valence band, the group III elements of the periodic table. If they are inside a semiconductor crystal such as germanium (a group IV element), this electron is missing in the covalent bond with the semiconductor atoms. This deficiency of one electron is a hole, and a *p*-type semiconductor is formed. Conversely, *donor* impurities have an extra electron, being group V elements of the periodic table. The fifth electron from the dopant is an excess electron and is free to move about in the crystal and hence participate in the flow of electric current. This type of semiconductor is referred to as *n*-type.

3.4.3   Semiconductors for γ ray spectrometry

A *p-n junction* results when *n*-type and *p*-type semiconductors are brought together into appropriate thermal contact, see Fig. 3.13. Electrons diffuse from the *n*-type material migrating across the junction into the *p*-type material and combine with holes, and the holes vice-versa.

As the electrons diffuse from the *n* region they leave behind positively charged donor atoms. Similarly, holes diffusing from the *p* region leave behind negatively acceptor atoms. The net positive charge in the *n* region and net negative charge in the *p* region will induce an electric field near the junction, in the direction from the *n* to the *p* region. The magnitude of this field increases as the charges migrate through the junction and eventually reaches the value (about 0.4 V high in germanium) preventing further charge diffusion. The action of diffusion of both
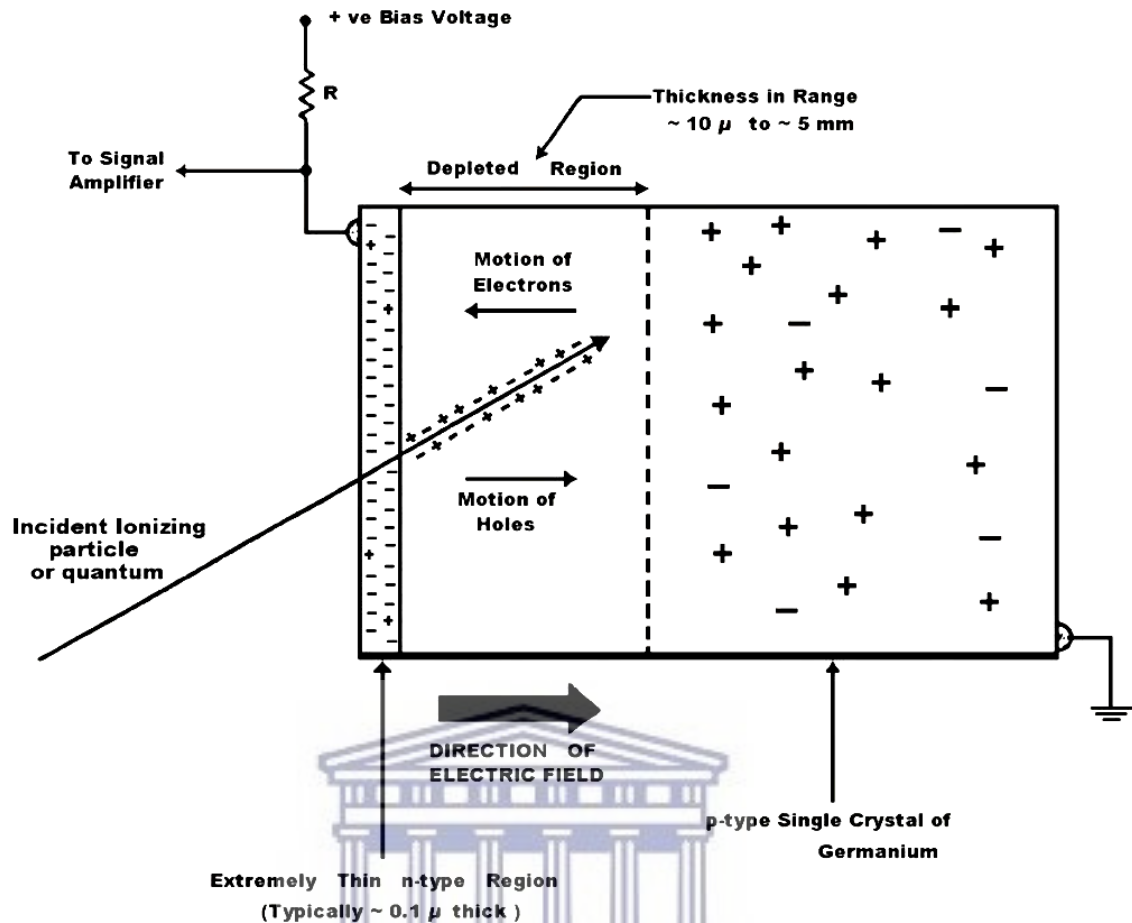
FIGURE 3.13: Cross-section of a typical reverse biased *p-n* junction radiation
detector. Modified from [9].

charge carriers creates a region surrounding the junction with no mobile charge
carriers referred to as a *depleted region*; this is the active element of the detector.

The depletion region can be effectively increased if a positive voltage (few kilovolts)
is connected to the *n* side of the junction. Because the positive voltage is connected
to the *n* type semiconductor, this is called *reverse biased junction*. The *p − n*
junction will conduct very little current when biased in the "reverse" direction. A
p−n junction operates like a *diode*. The fundamental property of a diode is that it
has low resistance to current in one direction but has a very high resistance in the
other direction. Since electrons and holes are present in abundance in the *n* and
p regions, respectively, the conductance is greatly enhanced across the junction
when biased in "forward" direction.

Semiconductor detectors like germanium, require that a bias is placed across them.
A bias is required so that full charge collection can occur. The bias is typically of
the order of ∼3000 V and is created by having a positive bias contact in the centre
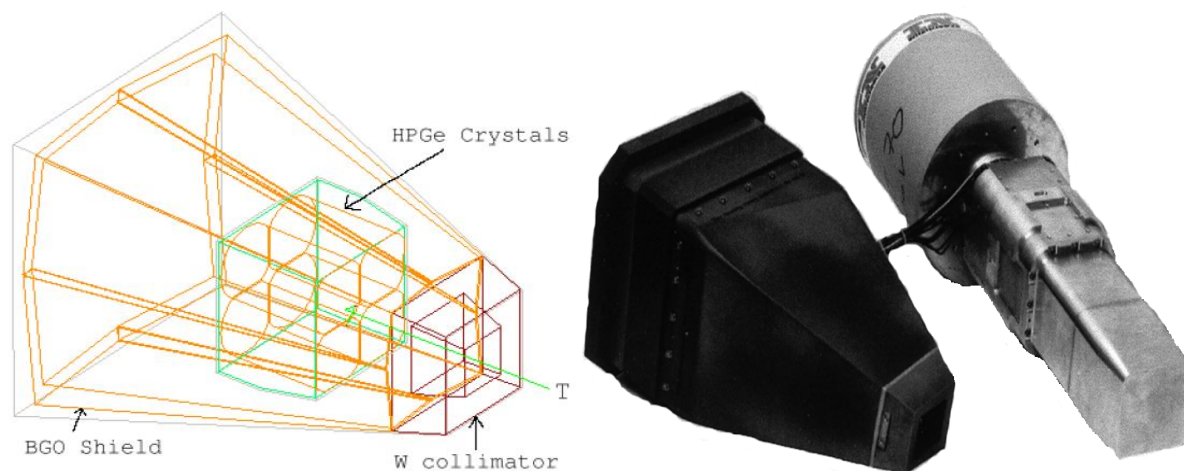
FIGURE 3.14: Clover detector showing a 3 dimensional-CAD view (left side) and an exploded view (right side) [10]. Gamma rays are produced at the target position (T) to the front face of the clover detector.

of the crystal and a negative bias contact on the outer surface. This creates an electric field in the detector. When an interaction happens, by any of the methods explained in the previous sections, an energetic electron is displaced. This electron is slowed down to a halt by interactions with other electrons creating electron-hole pairs. The movement of electron-hole pairs through the medium, under the influence of the electric field, (electrons toward the positive electrode and holes toward the negative electrode), creates a signal which corresponds to the energy of the interaction that took place.

3.4.3.1 Clover detectors

A clover detector consists of four individual *n*-type germanium crystals closely packed together in the configuration of a four-leaf clover, see Fig. 3.14. These four germanium segments are housed in a single cryostat. Each crystal is tapered at one end to allow better positioning of the detector to the reaction center thereby improve the overall efficiency of the detector. The clover detector is then coupled to an automatic liquid nitrogen filling system which top up the dewars with liquid nitrogen from the storage tank.

Some γ rays are Compton scattered from one segment to another, of the clover detector. The energy detected in both segments can be added to obtain the full energy of the γ ray. This enhances the photo-peak efficiency of the clover detectors especially for the γ rays with high energy. The process is called "addback".

3.4.4 The AFRODITE array
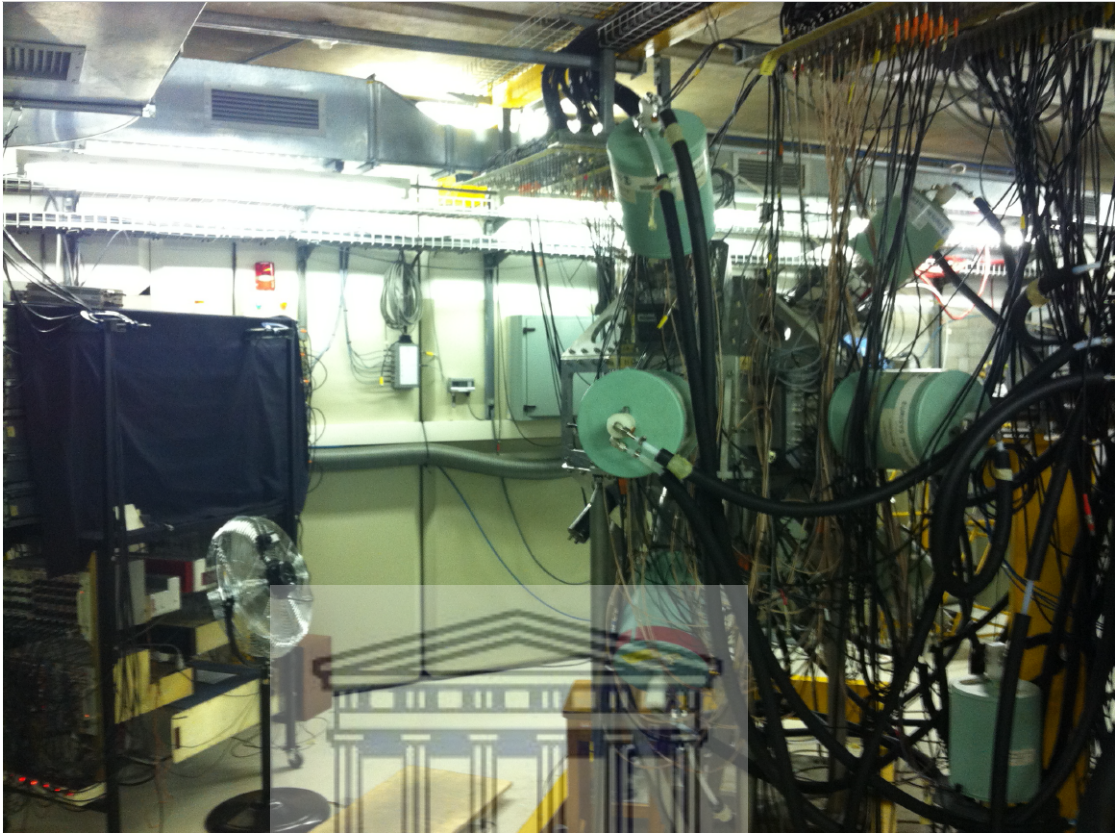
FIGURE 3.15: The AFRODITE array coupled to the neutron detector wall comprising a 2×6 set of plastic scintillators. The neutron wall, which is placed 2 m away from the target, is covered with a black fabric to prevent the ambient light disturbance of the pulse signal generated.

In this experiment γ rays were detected in coincidence with neutrons (detected with neutron wall) using an array of 8 HPGe Clover detectors, the AFRican Omnipurpose Detector for Innovative Techniques and Experiments (AFRODITE) array [85], Fig. 3.15. Each detector is surrounded by its own Compton suppression bismuth germanate, BGO shield. These detectors are mounted in a rhombicuboctahedron frame made of aluminium. The frame was originally designed to accommodate a maximum of 16 detectors. The two square facets at 0° and 180° with respect to the beam direction accommodate the beam line. The topmost square facet supports the target mechanism. For this experiment the 8 detectors were arranged such that, four of them were placed at 90° and the other four were at 135° to the beam direction.

The efficiency of the AFRODITE spectrometer is of order 1%. Typical energy resolution of each crystal is realistically about 3 keV full-width-half-maximum (FWHM) at 1 MeV.

3.4.5 Detector efficiency of the AFRODITE γ ray spectrometer

Gamma ray intensity, I_γ, is one of the most important experimental results of γ ray spectroscopy. In order to compare the intensity of detected γ rays it is important to understand the detection efficiency of the AFRODITE array as a function of detected γ ray energy. The intensity of a γ ray is a measure of the probability of the transition between two nuclear states. The intensity can be determined by using the formula

$$I_\gamma = \frac{A_\gamma}{\epsilon_\gamma},$$

(3.7)

where A_γ is the fitted area of a γ ray (using EFFIT radware program[88]), and ϵ_γ is the calculated efficiency of the corresponding peak. The relative detection efficiency of a γ ray in a single germanium detector is a function of the energy of the transition. The γ ray detection efficiency as a function of γ ray energy was measured using a calibrated source ^{152}Eu. The activity of the source was measured to be 367.15 kBq on 06 January 2004.

The activity on the day of efficiency calibration measurement, 29 April 2013, is projected from the activity measured in 2004, which is a period of about 3341.25 days. The half-life of ^{152}Eu source is known and is 13.33 y. The decay constant, λ is calculated utilizing Equation 3.8. The activity on the future date can then be calculated with Equation 3.9

$$\tau_{mean} = \frac{t_{\frac{1}{2}}}{ln(2)},$$

(3.8)

$$A = A_0 \cdot e^{-\frac{t}{\tau}}.$$

(3.9)

From the known activity, the number of decay events per second for the source can be simply calculated. By adjusting the expected number of decays for acquisition live time, the number of decay events which are expected to occur during the time period of the run is determined. The number of counts expected in each of the

calibration peaks, assuming a 100% detection efficiency, can thus be calculated. By dividing the number of counts detected during the calibration for each γ ray by the total number of counts expected for each γ ray; a measure of absolute detection efficiency of the AFRODITE array is obtained at the γ ray energies used. The efficiency at each energy measured is shown in Fig. 3.16. The array has a maximum efficiency around 150 keV. The efficiency curve decreases at higher energies, as the probability of absorption decreases due to the limited detector size. Below this energy, the efficiency drops rather rapidly due to absorption in the aluminium casing of the germanium detector.
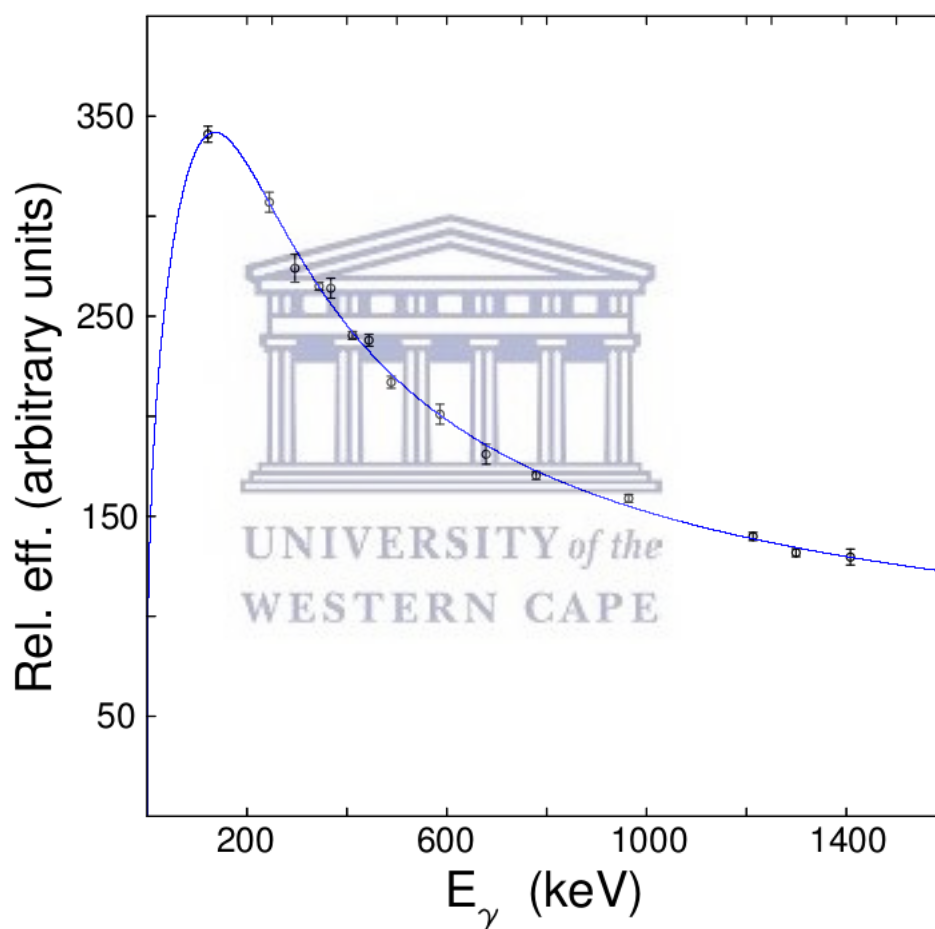
FIGURE 3.16: Efficiency curve for the AFRODITE γ ray spectrometer. The experimental data obtained using the known intensities of transitions in a ^{152}Eu calibration source.

Chapter 4

DATA ANALYSIS AND RESULTS

The aim of the experiments is to make high-resolution experiments to measure the relative strength of two-proton transfer to excited 0_n^+ states in ^{110}Cd, ^{112}Cd and ^{116}Sn, and excited $\frac{9}{2}^+$ states in ^{117}Sb. The beam energy of 25 MeV for the (^{3}He, n) reaction has been chosen so that high-resolution data can be compared with the low-resolution time-of-flight data of Fielding *et al.* [2] and Alford *et al.* [3] taken at the same energy. The targets used in the experiments were isotopically separated foils of ^{108}Pd (5.0 mg/cm^2), ^{110}Pd (1.3 mg/cm^2), ^{114}Cd (3.0 mg/cm^2) and ^{115}In (3.6 mg/cm^2) with the average beam intensity of $\sim$1 nA.

Immediately following the experiment, calibration data were collected using a ^{152}Eu source. The energies and intensities of the decaying γ ray peaks present in the coincidence spectra were measured by the fits to the spectra. Peak centroids and areas were determined by employing the Radware program [88]. The peak areas were converted into counts. During the analysis, the time width for data sampling was done at a period of 2 μs. The data were sorted into 1 and 2-dimensional histograms using the MTsort sorting program. Direct reactions are characterized by low multiplicities so that level schemes cannot be usefully constructed for the one neutron channels. However, all decay schemes are well known for the residual nuclei being studied here.

4.1 ^{108}Pd(^{3}He, n)^{110}Cd

Fig. 4.1 shows the total singles projection spectrum generated through the ^{108}Pd(^{3}He, xn)$^{111-x}$Cd fusion evaporation reactions. About 8×10^9 events were generated over a beam time period of $\sim$106 hr during this reaction. The spectrum is dominated by fusion evaporation channels, which have high cross sections as shown by the PACE4 cross section calculation in the inset, Fig. 4.1(b). The fusion evaporation reaction channel ^{108}Pd(^{3}He, $3n$)^{108}Cd is the most dominant with the ground-state band showing yrast states up to spin 6^+.

Time-correlation gates were placed on the time spectra shown in Fig. 4.2, to re-move random events. A narrow time-window gate of about 20 ns width was further placed on the time-of-flight spectrum, Fig. 4.3, to select γ rays that are coincident with fast-neutrons. This generated a γ ray spectrum with approximately 2×10^6 $n-\gamma$ coincident events. A high neutron energy gate at $E_n > 10.0$ MeV was placed on the spectrum to select γ rays in coincident with high-energy neutrons, see Fig. 4.4. Taking the ratio of counts for a peak in the direct reaction channel to fusion evaporation channel such as the 656.5 keV in ^{110}Cd to the 633.1 keV in ^{108}Cd, show an increase in the ratio of the yields as you increase the neutron energy gate. That is consistent with what is expected that for an increase in the energy of the gated neutrons; the fusion evaporation channel should decrease relative to the direct reaction channel. The spectrum in Fig. 4.5 is gated with time-of-flight and high-energy neutrons, and a background spectrum in coincidence with low energy neutrons normalised to the 634.0 keV peak from the fusion evaporation channel ^{108}Pd(^{3}He, $3n$)^{108}Cd, was subtracted. This has removed the fusion evaporation channels to get a relatively clean spectrum, which show two dominant peaks at 204.0 and 656.5 keV.

In spite of the geometry only favouring $L = 0$ transfer, the data is showing an $L > 0$ transition; a weak 656.5 keV $2^+ \rightarrow 0^+$ transition is from the direct reaction channel ^{108}Pd(^{3}He, n)^{110}Cd. A strong peak at 204.0 keV has been observed in the spectrum. This γ ray is the second excited state with spin $\frac{7}{2}^+$ in ^{109}Cd. It has been populated through the (^{3}He, $2n\gamma$) reaction channel. The $2n$ channel is more favoured than the $4n$ channel (as this γ ray appears in both ^{107}Cd and ^{109}Cd nuclei) in terms of the PACE4 calculations, see inset in Fig. 4.1(b). There are no $L = 0$ transitions observed in the spectrum, Fig. 4.5. The measured photo-peak areas of the 204.0 and 656.5 keV transitions are given in Table 4.1.
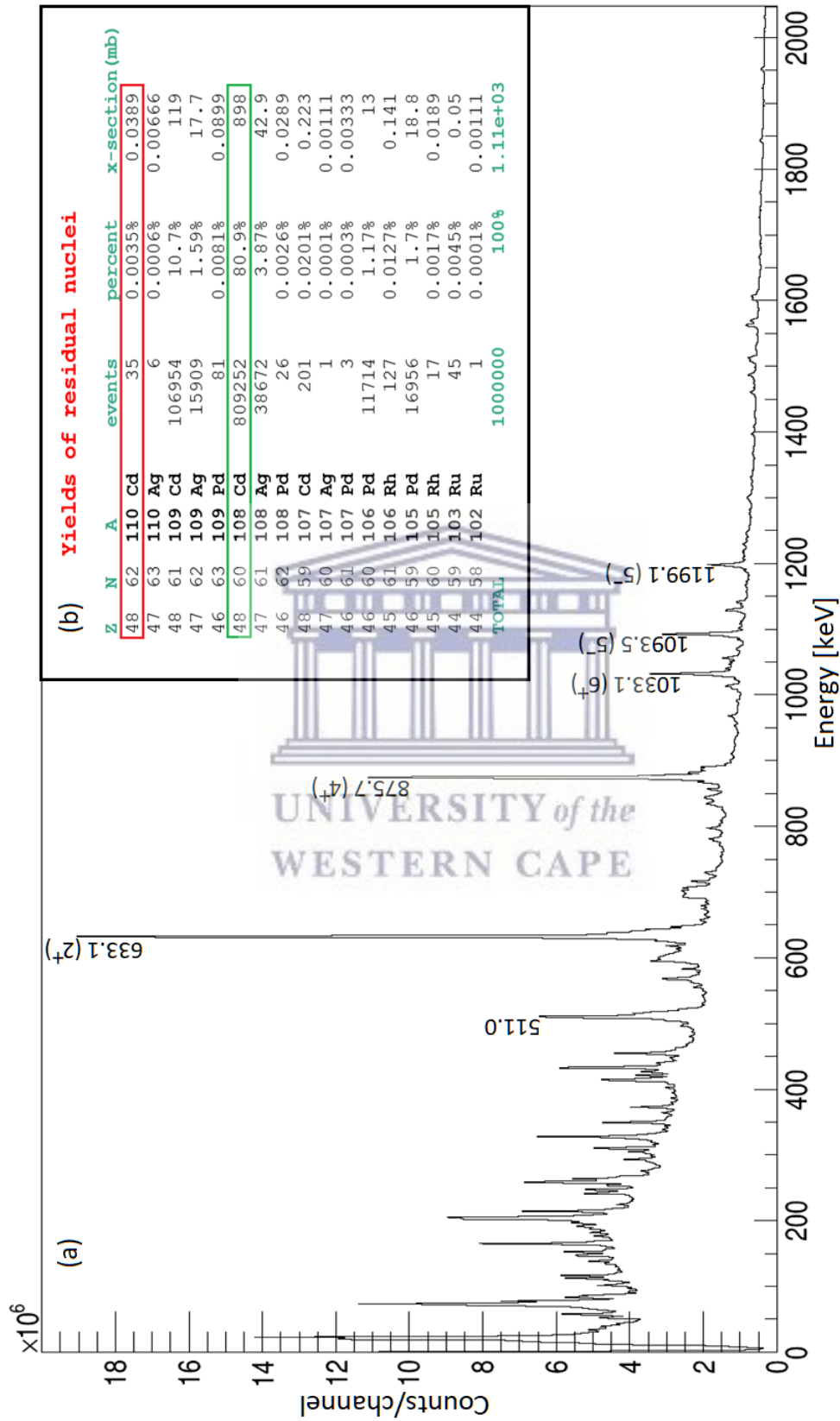
FIGURE 4.1: (a) A total singles γ ray spectrum generated during the ^{108}Pd(^{3}He, n)^{110}Cd reaction. The spectrum is dominated by the high cross section fusion evaporation channels, with ^{108}Pd(^{3}He, $3n$)^{108}Cd being the most dominant channel as also confirmed by the PACE4 calculation in the inset (b).
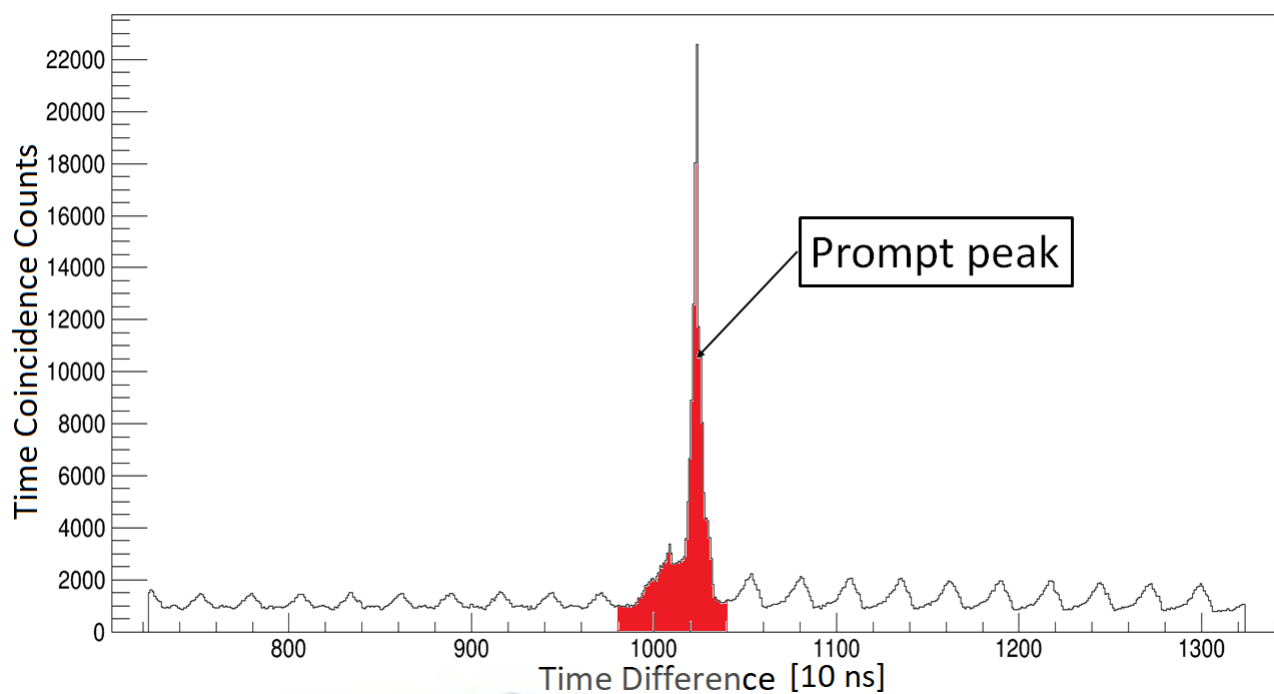
FIGURE 4.2: Time-correlated spectrum from time-stamp differences between neutron and clover detectors generated during the ^{108}Pd(^{3}He, n)^{110}Cd reaction.
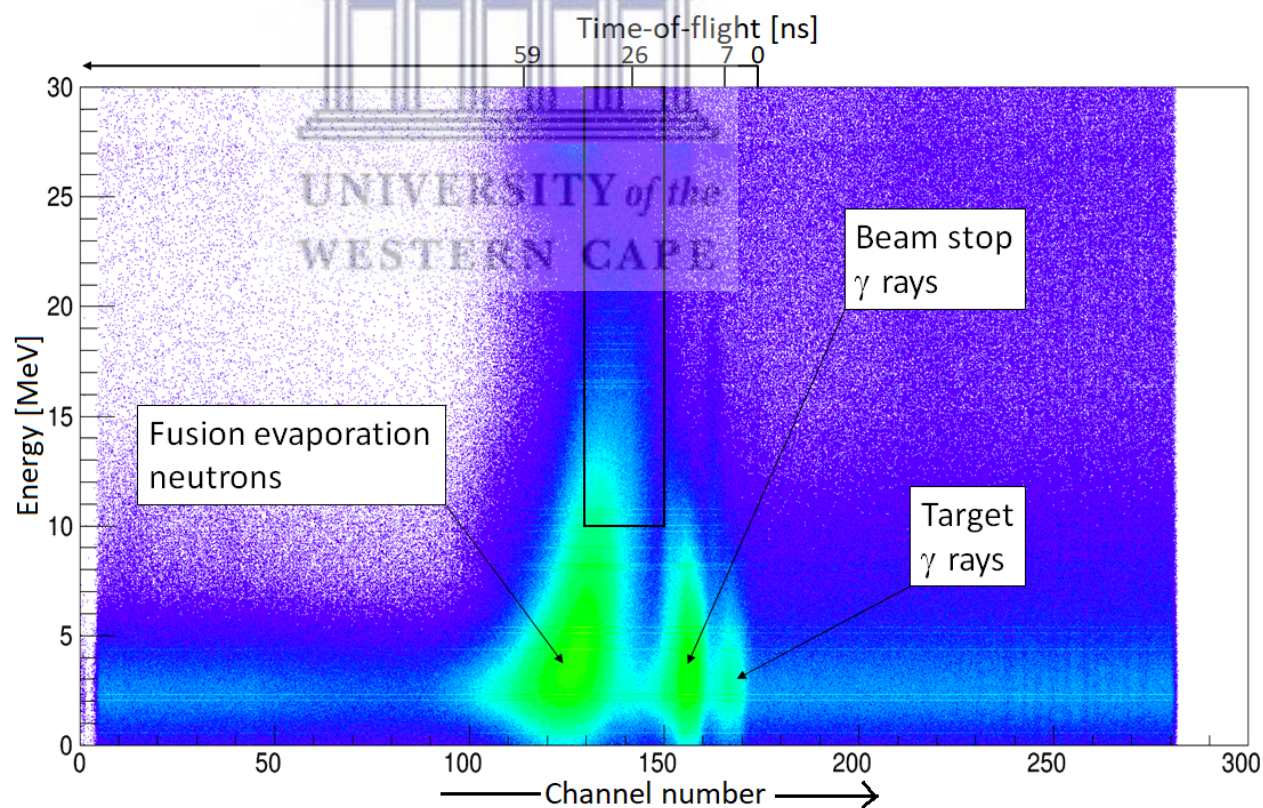
FIGURE 4.3: A scatter plot of the time-of-flight mapped against the energy of the particles generated in the ^{108}Pd(^{3}He, n)^{110}Cd reaction. The rectangular box is used for gating on the fast neutrons.

FIGURE 4.4: (a) A spectrum gated with time-of-flight and high-energy neutrons, $E_n > 10$ MeV. Shown in the inset (b) is a decay level scheme for the dominant fusion evaporation channel, ^{108}Pd(^{3}He, $3n$)^{108}Cd.
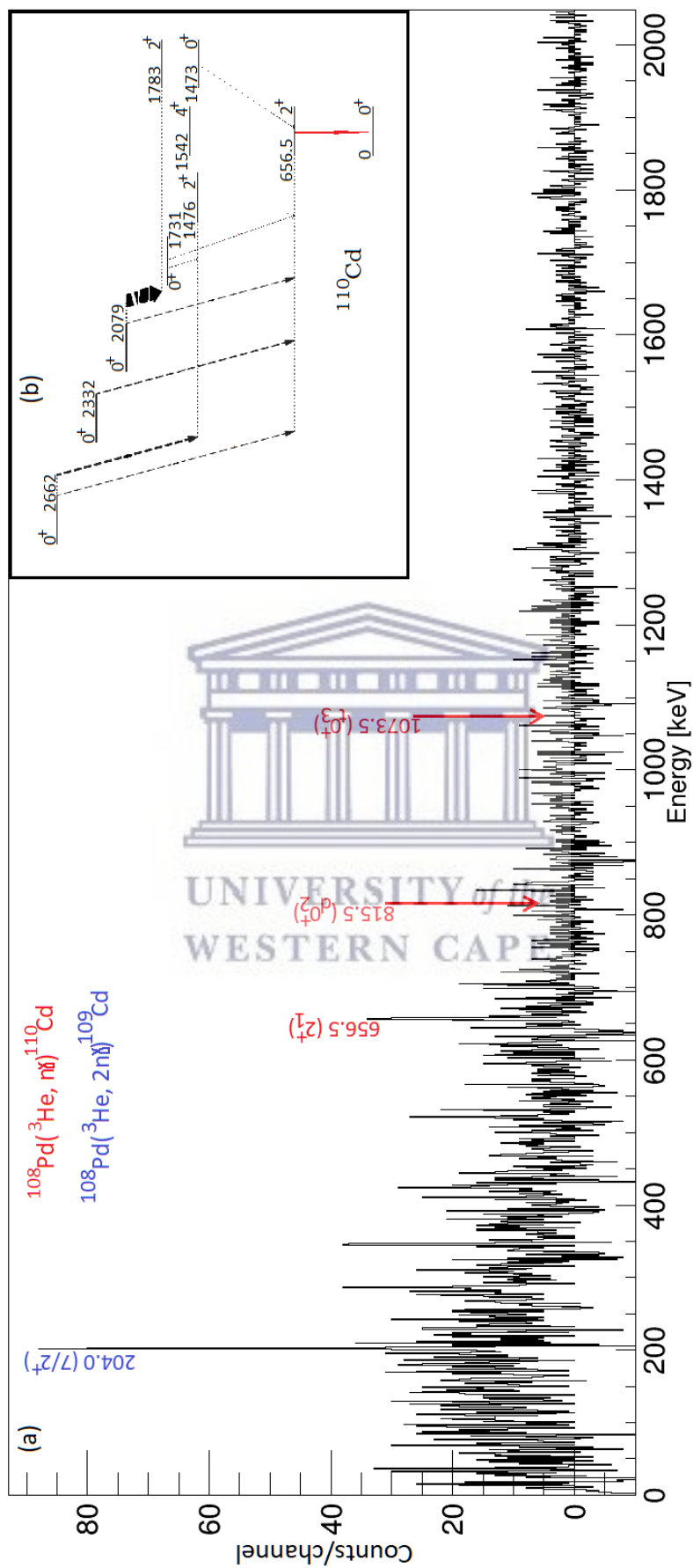
FIGURE 4.5: A γ ray spectrum gated with time-of-flight and high-energy neutrons, $E_n > 10$ MeV, normalized to the 633.1 keV peak for background subtraction. Shown in the inset (b) is a decay level scheme for the ^{110}Cd nucleus.

TABLE 4.1: Extracted γ ray counts for a peak in ^{110}Cd. The other properties of the states are included for completeness, and are taken from [13].

E_{level} (keV)	J_i^π	E_{trans} (keV)	J_f^π	γ-peak area (Counts)	Multi-polarity
656.5	2_1^+	656.5	0_1^+	346	$E2$
†204.98	$\frac{7}{2}^+$	204.0	$\frac{5}{2}^+$	762	$M1$

† The state has been identified to be originating from (^{3}He, $2n$) channel

FIGURE 4.6: A scatter plot of the time-of-flight mapped against energy of the particles generated in the experiment ^{110}Pd(^{3}He, n)^{112}Cd. The rectangular box is used for gating on the fast neutrons.

4.2 ^{110}Pd(^{3}He, n)^{112}Cd

The target nucleus has two more neutrons than ^{108}Pd and the residual nucleus populated in the direct reaction channel ^{110}Pd(^{3}He, n)^{112}Cd has a slightly lower excitation energy of the first 2^+ state than in the ^{110}Cd nucleus. Fig. 4.7(a) shows a γ ray singles spectrum generated in the reactions ^{110}Pd(^{3}He, xn)$^{113-x}$Cd. The spectrum is dominated by the fusion evaporation channels, with the 3n channel being the most dominant one, as also shown by the PACE4 calculation in the inset, see Fig. 4.7(b). The yrast band states in the fusion evaporation channel can be seen up to the spin 6^+ level. A total of approximately 6×10^9 counts were generated over a beam time of $\sim$77 hr in this experiment.

A 2-dimensional scatter plot of the time-of-flight as function of neutron energy is shown in Fig. 4.6. The spectrum in Fig. 4.8 was generated using a time difference spectrum of the neutron and clover detectors and gating on high-energy neutrons, with $E_n > 10$ MeV. A total of 9×10^5 $n - \gamma$ coincident events were generated in the time gated spectrum. A weak 617.2 keV $2^+ \rightarrow 0^+$ state is populated in the direct reaction ^{110}Pd(^{3}He, n)^{112}Cd channel of interest. A background spectrum (in coincident with low-energy neutrons) was subtracted from the spectrum, normalized to the strongest peak 657.7 keV in the fusion evaporation channel. The
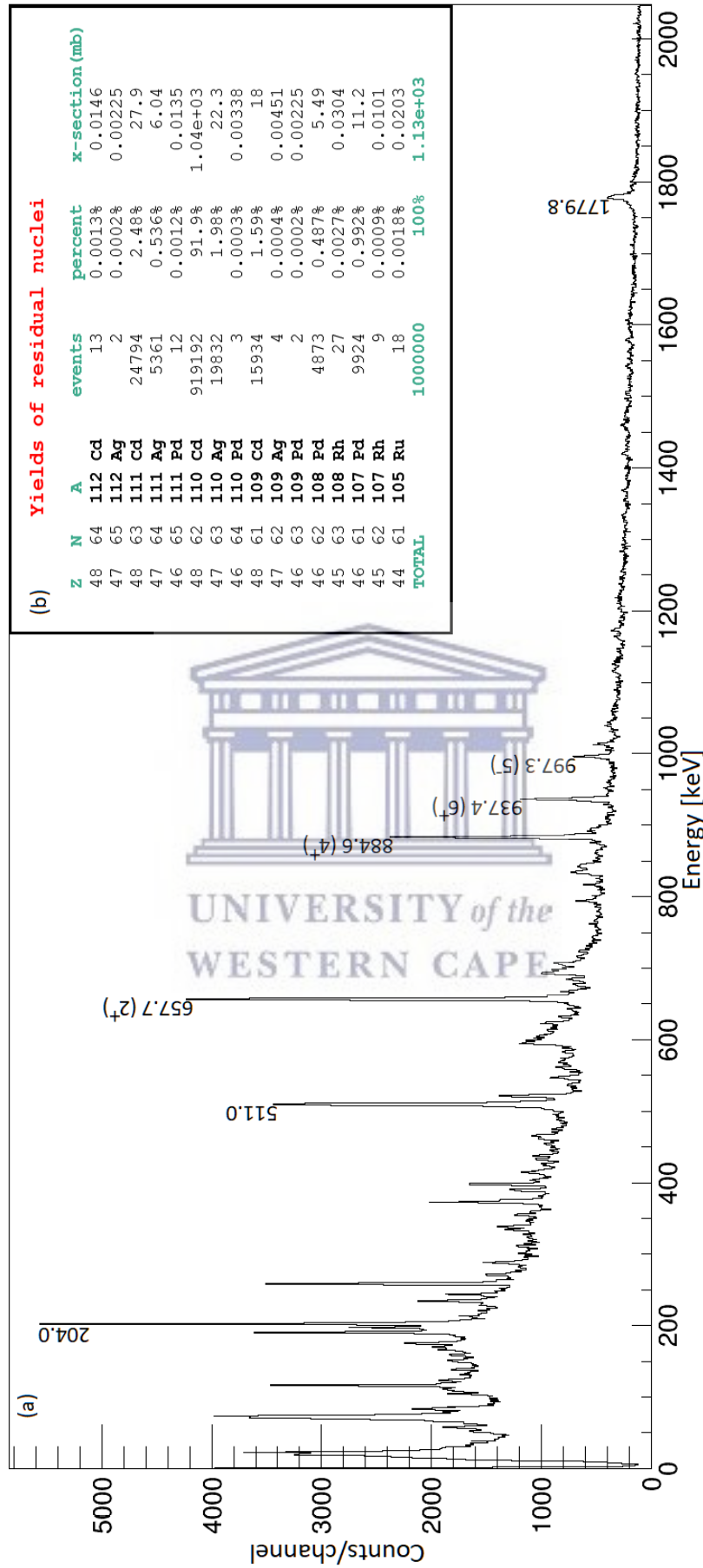
FIGURE 4.7: (a) A total projection spectrum dominated by the ^{110}Pd(^{3}He, $3n$)^{110}Cd channel. Shown in the inset (b) is a PACE4 calculation for the different reaction channels populated in the reaction.

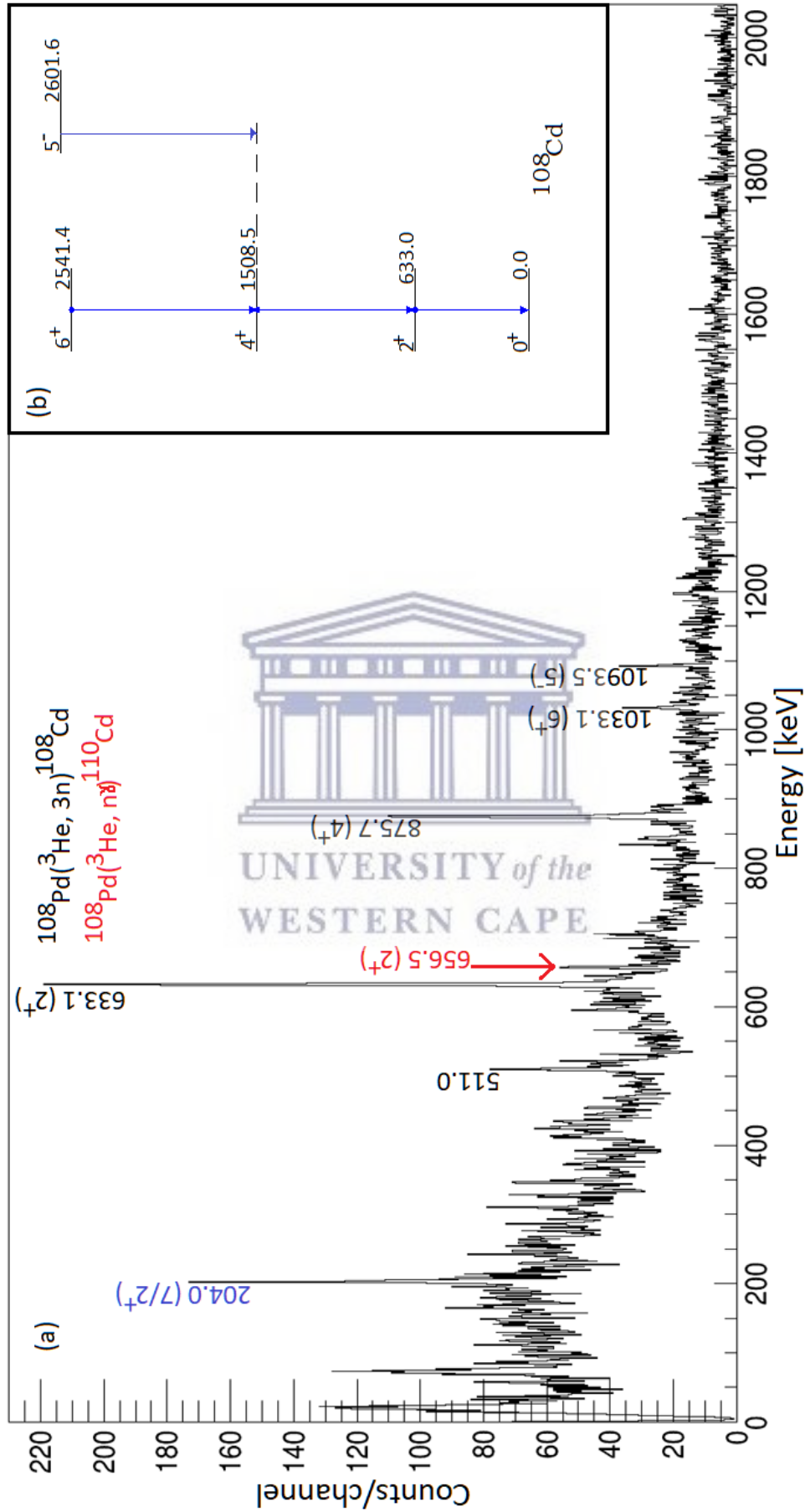FIGURE 4.8: (a) A γ ray spectrum gated with time-of-flight and high-energy neutrons, $E_n > 10$ MeV. Shown in the inset (b) is a decay level scheme for the dominant fusion evaporation channel, ^{110}Pd(^{3}He, $3n$)^{110}Cd.

TABLE 4.2: Extracted γ ray counts for a peak in ^{112}Cd. The other properties of the transition are taken from [13] for completeness.

E_{level} (keV)	J_i^π	E_{trans} (keV)	J_f^π	γ-peak area (Counts)	Multi-polarity
617.2	2_1^+	617.2	0_1^+	43	$E2$

obtained spectrum after gating and background subtraction is shown in Fig. 4.9. The measured photo-peak area for the 617.2 keV transition is given in Table 4.2.
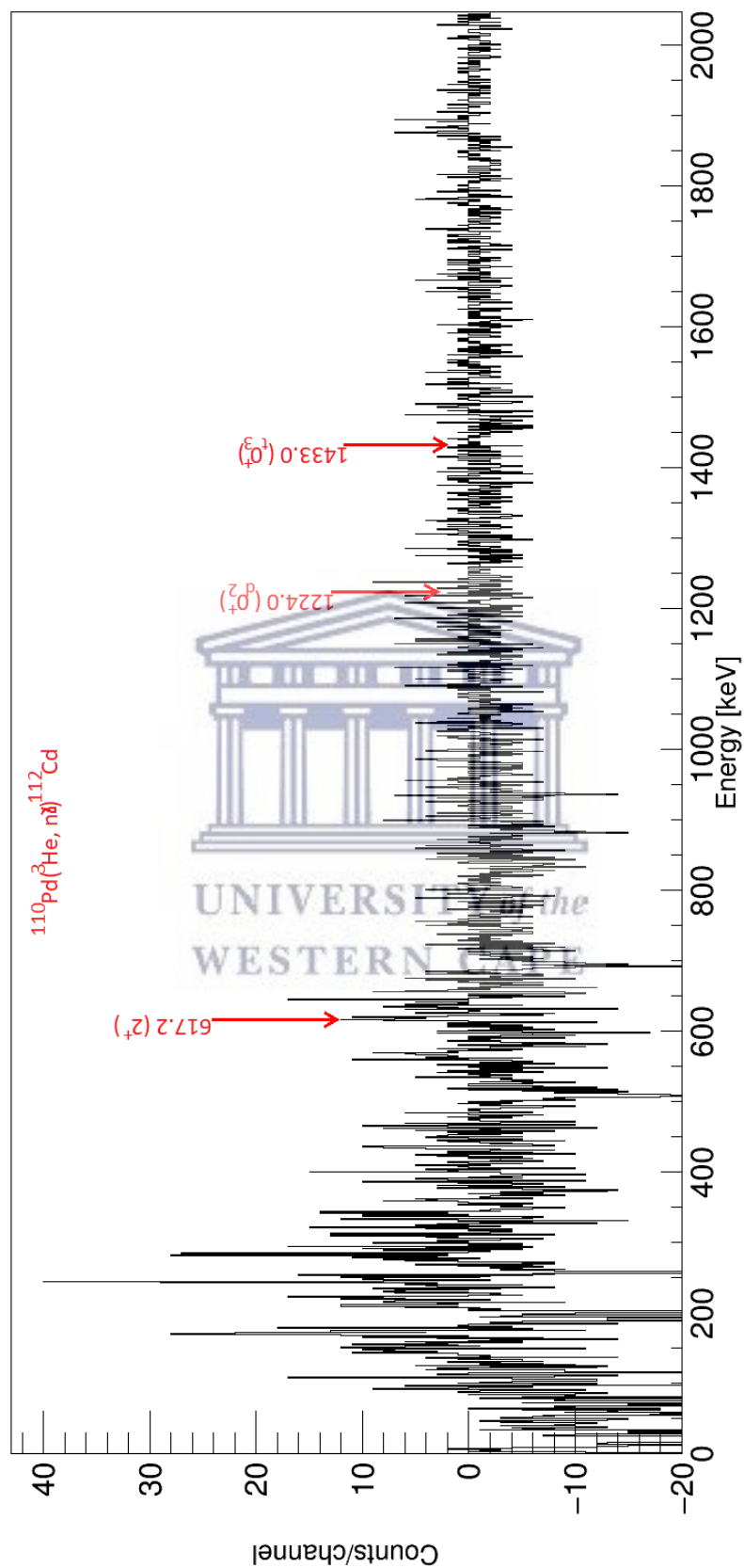
FIGURE 4.9: A γ ray spectrum gated with time-of-flight and high-energy neutrons $E_n > 10$ MeV, normalized to the 657.7 keV peak for background subtraction.
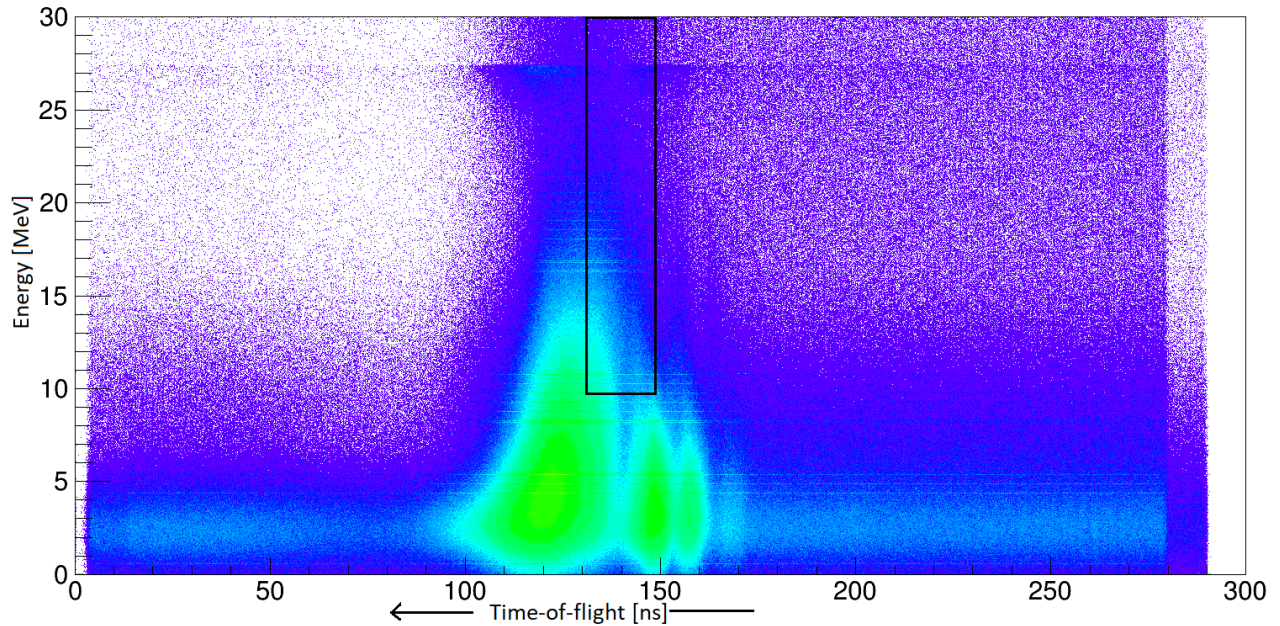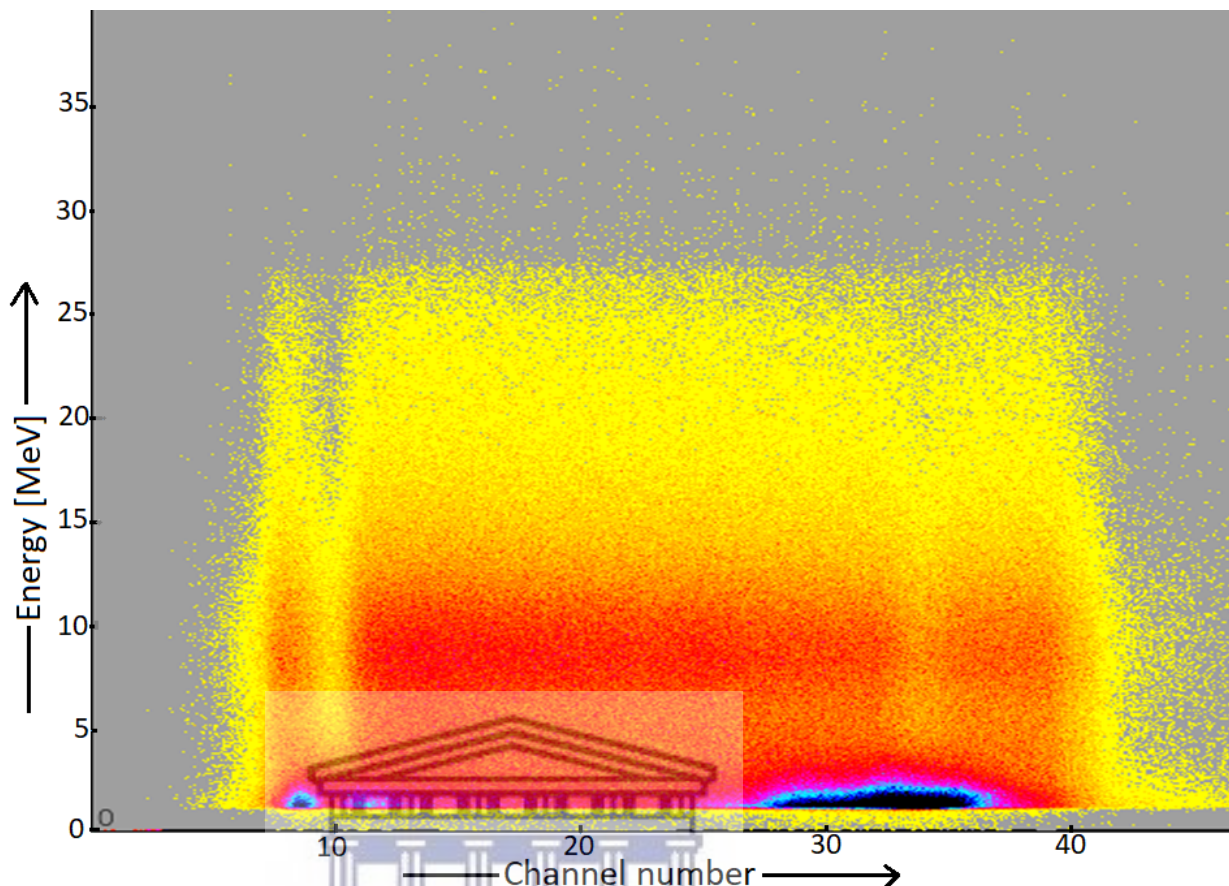
FIGURE 4.10: A scatter plot of the time-of-flight mapped against the energy of the particles generated in the ^{114}Cd(^{3}He, n)^{116}Sn reaction.

4.3 ^{114}Cd(^{3}He, n)^{116}Sn

The target nucleus ^{114}Cd is 2 protons away from the closed Z = 50 proton shell, the residual nucleus populated in the direct transfer has a closed proton shell, Z = 50. The 2-dimensional scatter plot shows no separation of the expected centroids of the target γ rays, the beam dump γ rays or fusion evaporation neutrons due to the poor timing structure of the spectrum, see Fig. 4.10. A γ ray singles spectrum generated in the reactions ^{114}Cd(^{3}He, xn)$^{117-x}$Sn is shown in Fig. 4.12(a). The spectrum is dominated by the fusion evaporation channel ^{114}Cd(^{3}He, $3n$)^{114}Sn, with the yrast band members seen up to 4^+ spin. A total of about 4×10^9 events were generated in the total projection spectrum. The data was taken over a beam time of $\sim$40 hr.

A time-correlation spectrum, shown in Fig. 4.11 was used to remove the dominant fusion evaporation channels. The generated γ ray spectrum had approximately
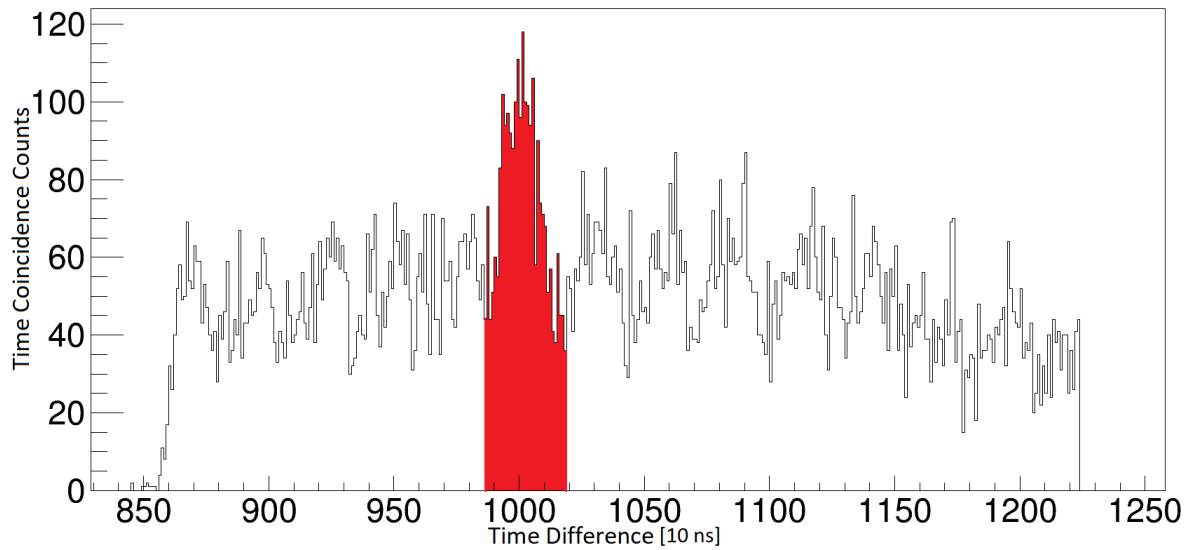
FIGURE 4.11: A time difference spectrum between the RF and clover detectors generated in the ^{114}Cd(^{3}He, n)^{116}Sn reaction.

2×10^4 $n - \gamma$ coincident events. This is a fairly low statistics data set. There are no peaks in the channel of interest in the normalized background subtracted spectrum shown in Fig. 4.13.
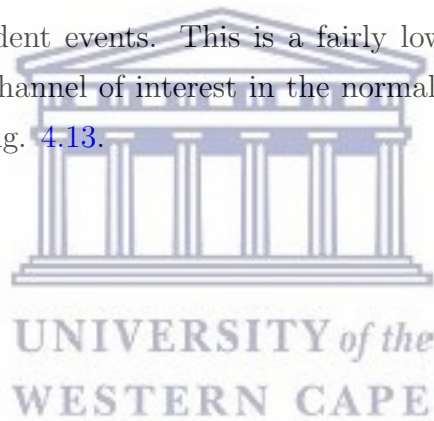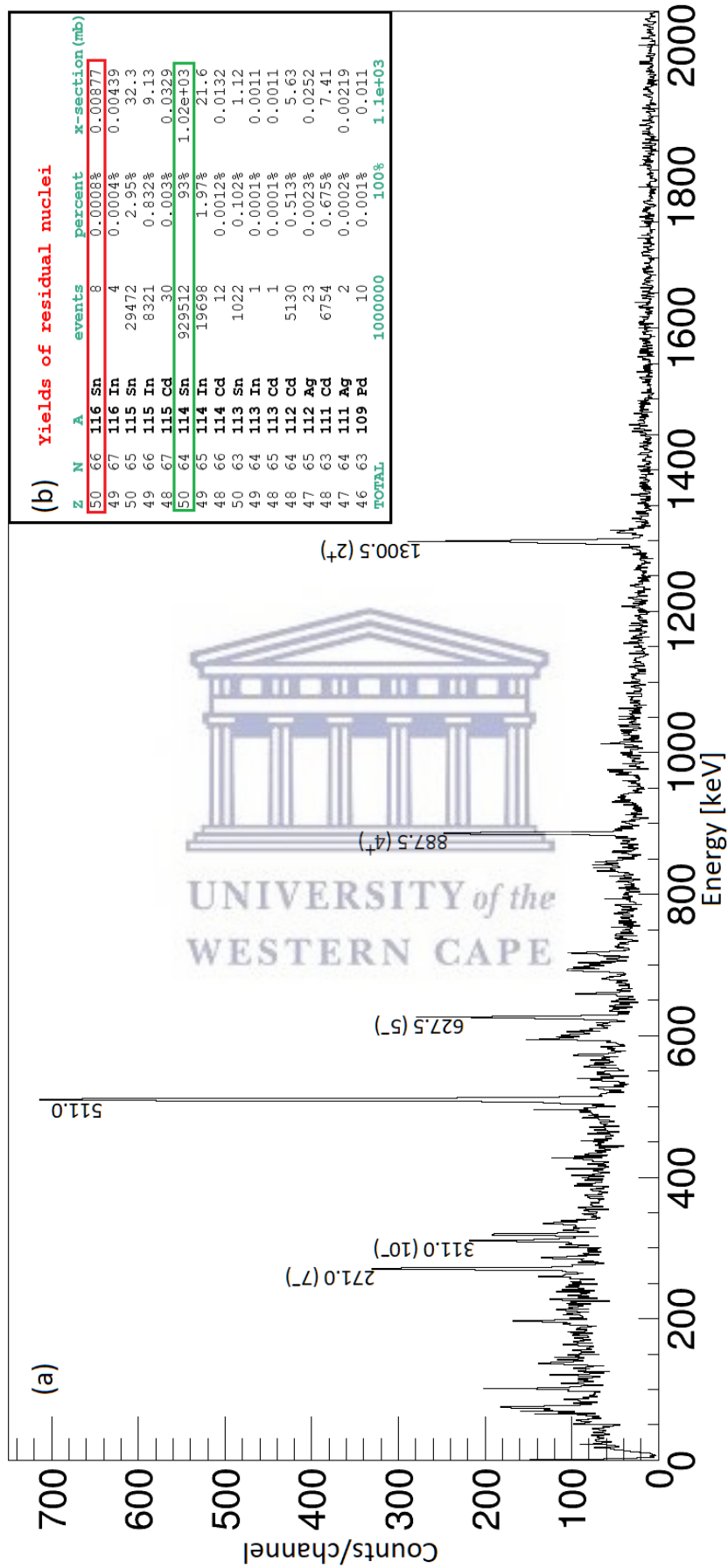
FIGURE 4.12: (a) A total projection spectrum dominated by ^{114}Cd(^{3}He, $3n$)^{114}Sn channel. Shown in the inset (b) is the PACE4 calculations for the different reaction channels populated in the reaction.
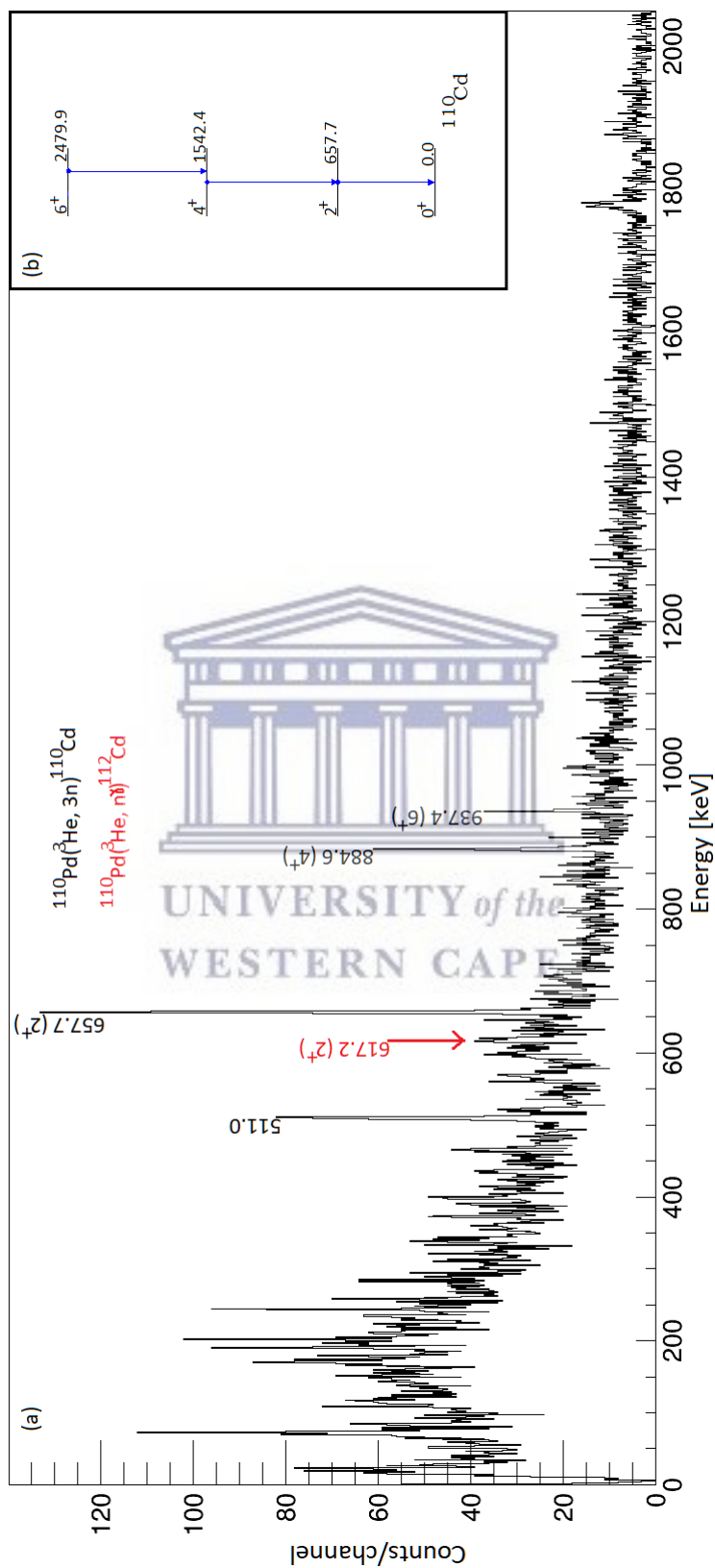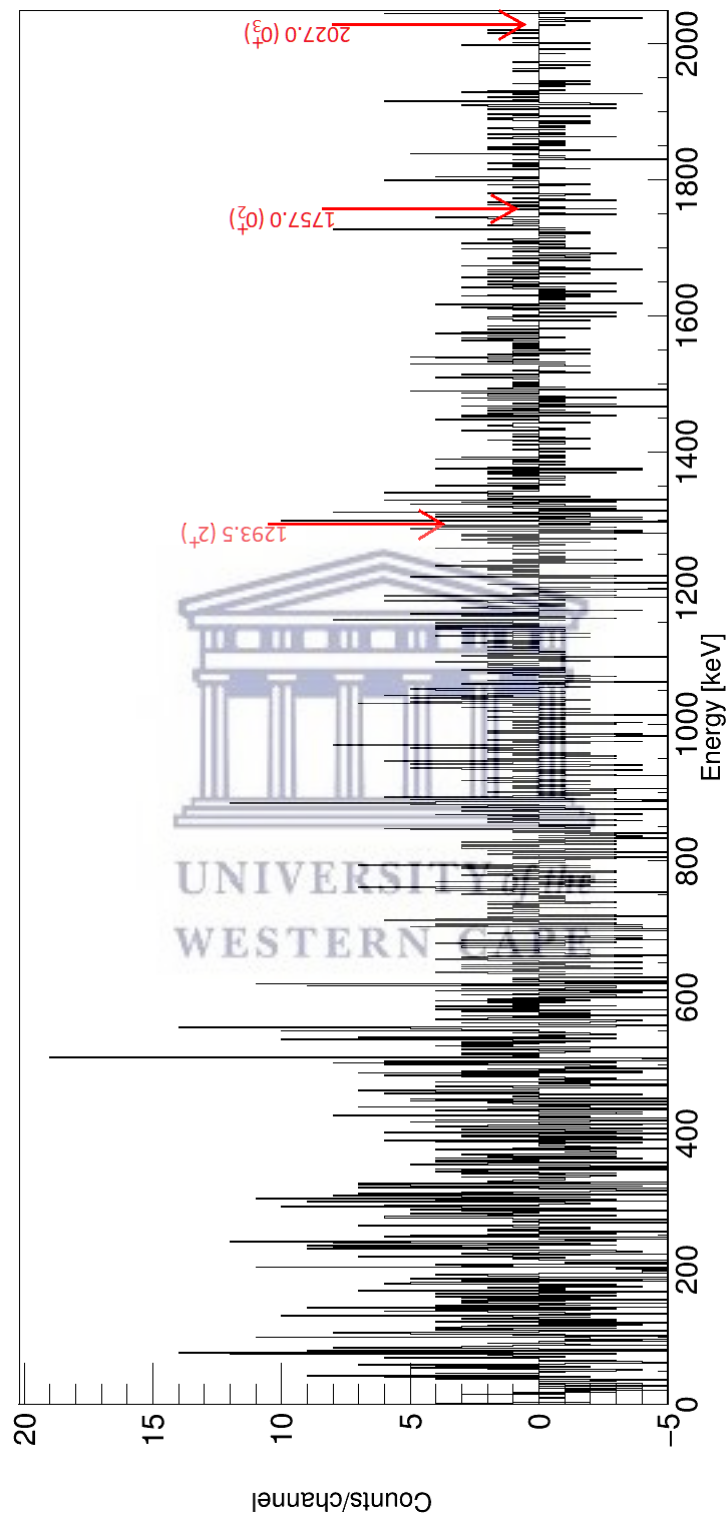
FIGURE 4.13: A γ ray spectrum gated by time-of-flight and high-neutron energy, $E_n > 10$ MeV. A background spectrum normalized to 627.5 keV peak has been used for background subtraction.

TABLE 4.3: Extracted γ ray counts for peaks in ^{117}Sb. The other properties of the transitions are taken from [13] for completeness.

E_{level} (keV)	J_i^π	E_{trans} (keV)	J_f^π	L	γ peak area (Counts)	Multi-polarity
527.2	$\frac{7}{2}^+$	527.2	$\frac{5}{2}^+$	2	398	$M1(+E2)$
1535.0	$\frac{11}{2}^+$	374.5	$\frac{9}{2}^+$	2	104	$M1, E2$
1160.7	$\frac{9}{2}^+$	1160.0	$\frac{5}{2}^+$	0	212	$E2$
1488.0	$\frac{9}{2}^+$	960.9	$\frac{7}{2}^+$	0	37	$E2$
1312.0	$\frac{9}{2}^+$	1312.0	$\frac{5}{2}^+$	0	47	$E2$
*3377.4	4^+	1489.8	2^+	2	167	$E2$
*1887.6	2^+	1887.6	0^+	2	127	$E2$

* The peaks are from the contamination by ^{18}O(^{3}He, n)^{18}Ne reaction.

4.4 ^{115}In(^{3}He, n)^{117}Sb

Fig. 4.14 shows a γ ray singles spectrum showing transitions of γ rays from a wide range of fusion evaporation channels in the ^{115}In(^{3}He, xn)$^{118-x}$Sb reactions. These reactions have high cross sections compared to the direct reaction channel. A PACE4 calculation, in the inset Fig. 4.14(b) predicts ^{115}Sb to have the highest cross section of about 719 mb at 67% relative to all other channels. Approximately 8×10^9 events were generated in the total projection spectrum. The data was taken over a beam time of $\sim$53 hr.

A time window gate was placed on the prompt peak of the time difference spectrum, see Fig. 4.15, in order to generate a spectrum of $n - \gamma$ correlated events, and to remove the dominant fusion evaporation channels. This generated a total of about 2×10^6 $n - \gamma$ coincidence events, Fig. 4.14(a). A further gate using high-energy fast neutrons $E_n > 10$ MeV, was used and the spectrum was normalized (to the 497.0 keV γ ray peak) with a spectrum tagged with slow neutrons for background subtraction. This lead to an improved peak to background noise ratio in the spectrum, shown in Fig. 4.17. Due to the poor time structure of the time-of-flight spectrum shown in Fig. 4.16, no gates were placed on the time-of-flight.

The target nucleus ^{115}In (an odd-even nucleus) is one proton hole in the g$_{\frac{9}{2}}$ closed shell, which is an intruder orbit at the top of the major shell below Z = 50. Its ground state spin is $\frac{9}{2}^+$. In terms of the shell model, the orbitals above Z = 50 are
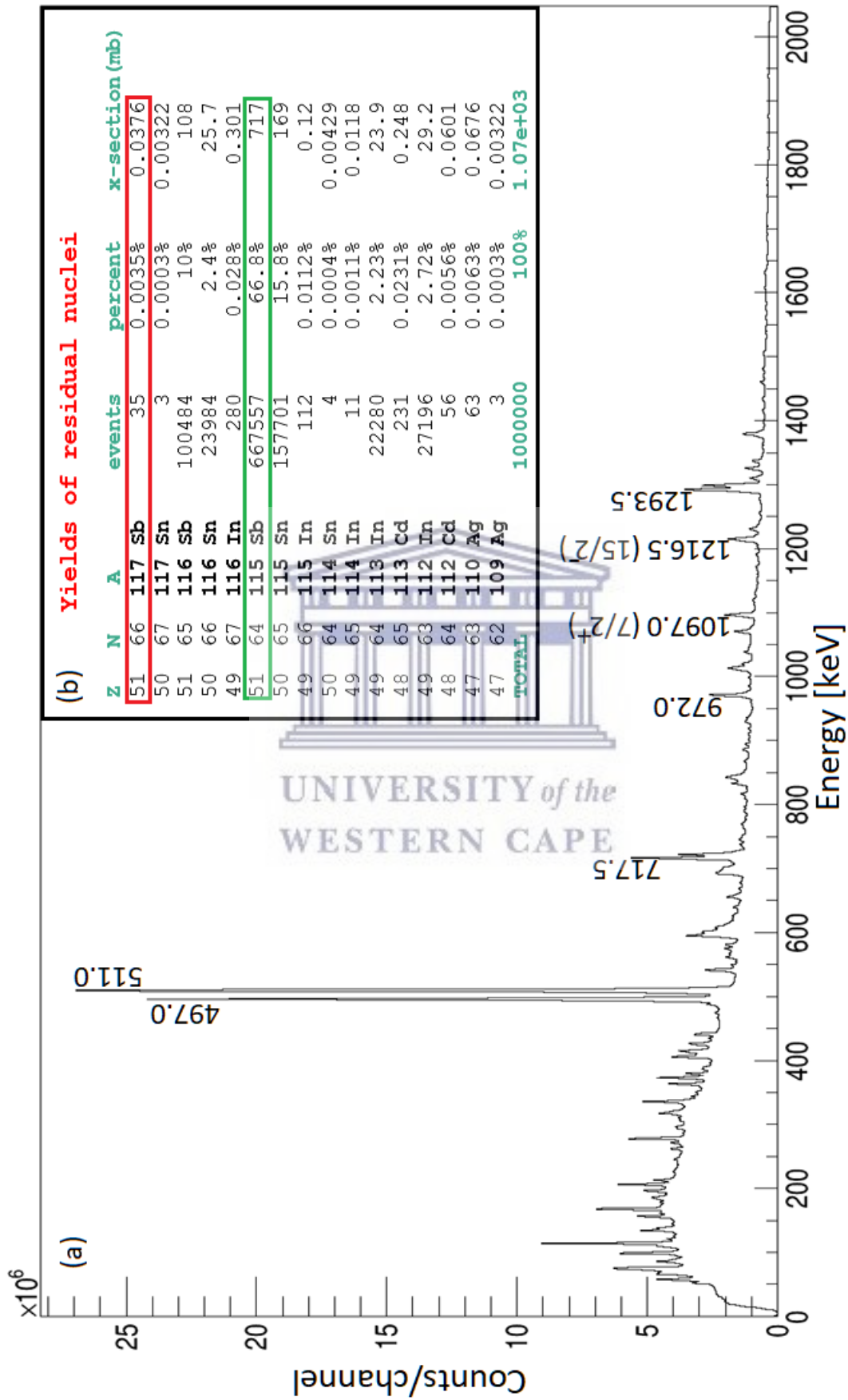
FIGURE 4.14: (a) A γ ray singles spectrum dominated by fusion evaporation $^{115}\text{In}(^3\text{He}, xn)^{118-x}\text{Sb}$ channels. Shown in the inset (b) is a PACE4 calculation for the different fusion evaporation reaction channels populated in this reaction.
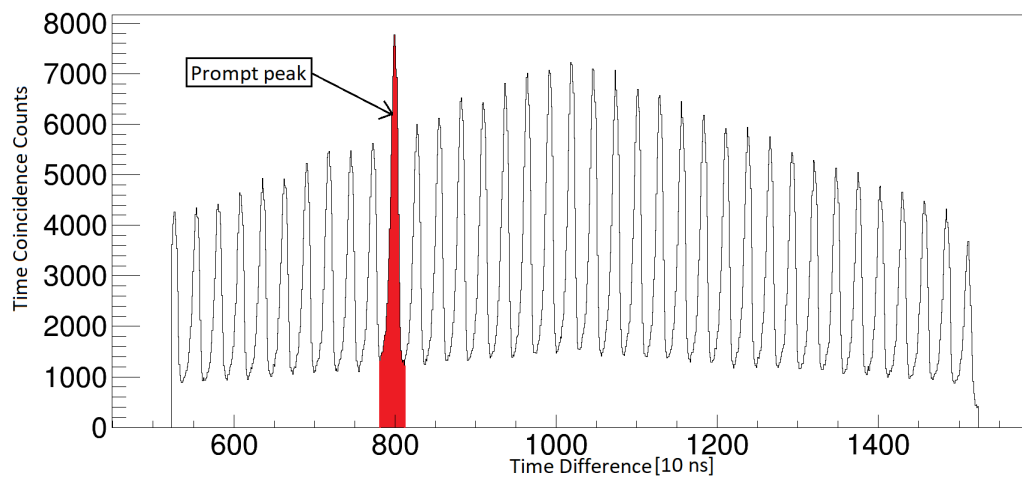
FIGURE 4.15: Time difference spectrum between the time-stamp of neutron and clover detectors generated in the ^{115}In(^{3}He, n)^{117}Sb experiment.
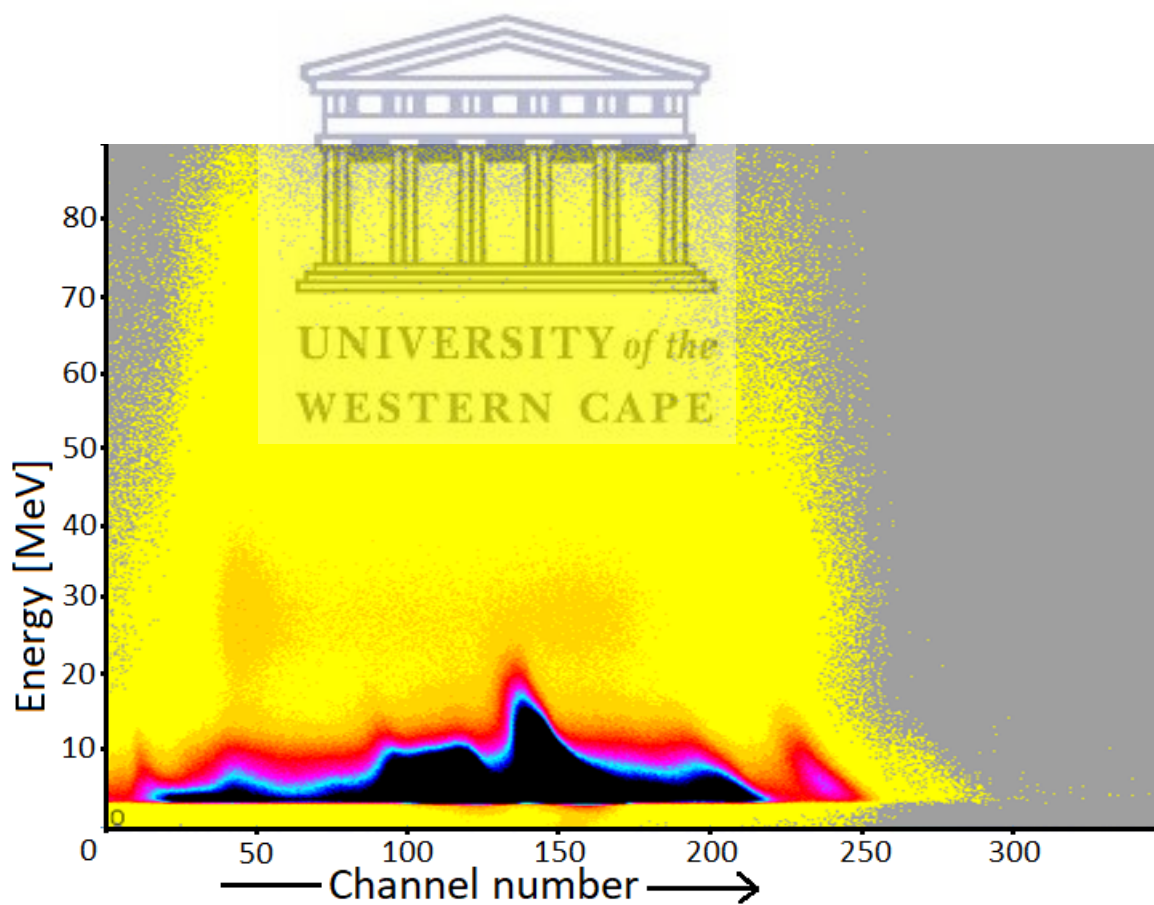
FIGURE 4.16: A scatter plot of the time-of-flight mapped against the energy of the particles generated in the ^{115}In(^{3}He, n)^{117}Sb reaction. The neutron energy gate was set at $E_n > 10$ MeV.

the $1\mathrm{g}_{\frac{7}{2}}$, $2\mathrm{d}_{\frac{5}{2}}$, $1\mathrm{h}_{\frac{11}{2}}$, $2\mathrm{d}_{\frac{3}{2}}$ and $3\mathrm{s}_{\frac{1}{2}}$. The correlated pair of protons stripped onto ^{115}In target can only pick orbitals above Z = 50 mainly states with spin $\frac{9}{2}^+$ as there is no angular momentum being transferred in the process for $L = 0$ transitions.

The 1534.0 keV State

The 1534.0 keV with spin $\frac{11}{2}^+$ is the highest energy level that has been populated in this reaction. This is an $L > 0$ proton transfer, which is less favoured by this experimental set-up. The population of this state may be attributed to Coulomb or inelastic interactions of the incoming ^{3}He and/or outgoing neutron with the target and/or residual nucleus [89]. This state depopulates by a 374.2 keV transition to the 1160.0 keV $\frac{9}{2}^+$ level, which is the band head of a deformed $K^\pi = \frac{9}{2}^+$ band.

The 1160.7 keV State

The shell structure of the target nucleus ^{115}In with Z = 49 is 1 proton short to the closed Z = 50 shell. In terms of its proton configuration, it has a hole in its deformation upsloping $\pi[404]9/2^+$ Nilsson orbital intruding from below the Z = 50 proton shell. The two protons that are transferred to the target can only be placed in the orbitals above the Z = 50 closed shell, thereby creating a 2p-1h configuration. The 1160.7 keV level is the lowest of these $\frac{9}{2}^+$ states that were populated in this reaction, ^{115}In(^{3}He, n)^{117}Sb. Only 50% of the strength of the 1160.7 keV peak comes from contributions of the 374.0 keV γ ray transition. The rest of the strength could be from the direct 2-proton transfer population as there are no other evident transitions feeding this state in the spectrum, see Fig. 4.17.

The 1488.0 keV state

This is the other $\frac{9}{2}^+$ state that has been populated through a direct reaction transfer method. The 1488.0 keV level is the highest of the $\frac{9}{2}^+$ states that were populated through an $L = 0$ two proton transfer in this spectrum. This state depopulates by a 960.9 keV transition to the 527.2 keV level.
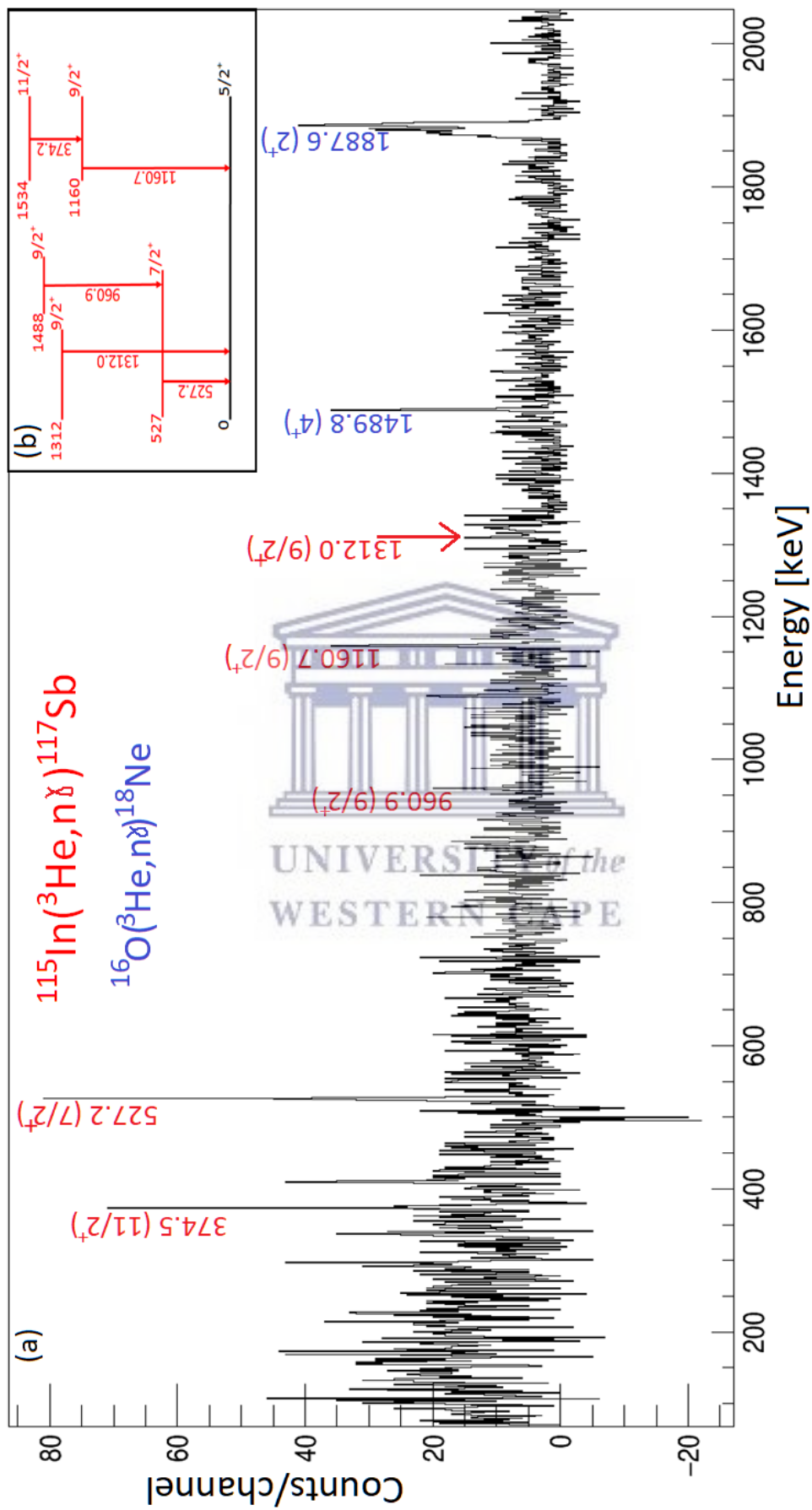
FIGURE 4.17: (a) A γ ray spectrum gated by the high-energy neutrons, $E_n > 10$ MeV, and normalised to the 497 keV peak for background subtraction. The red labelled peaks are from the direct reaction channel, ^{115}In(^{3}He, n)^{117}Sb. (b) The level scheme for the ^{117}Sb identified peaks is shown in the inset. The peaks labelled blue are from an oxygen contaminant of the target, causing the reaction ^{16}O(^{3}He, n)^{18}Ne.

The 1312.0 keV state

There is also a direct reaction population of the 1312.0 keV state with spin $\frac{9}{2}^+$ possible through an $L = 0$ two proton transfer. The band configuration for this state is formed by the coupling of the 2p-2h deformed structure known in the ^{116}Sn core to the single particle low-K valence $\pi d_{\frac{5}{2}}$ orbital [90, 91]. The population strength of this state is not strong. It decays directly to the ground state.

The 527.2 keV state

The 527.2 keV state with spin $\frac{7}{2}^+$ is an $L > 0$ two proton transfer. Part of the strength of this state is from contributions from feeding through the 960.9 keV γ ray transition which possible contribute about 10% of the strength. Also this state may have been populated via the Coulomb or inelastic interaction of the beam with the target and/or residual nucleus as the yields are significantly large to have contribution from only the 960.9 keV decay. There are no other observable feeding transitions to this state in the spectrum.

All the extracted γ ray yields for the transitions in the spectrum Fig. 4.17 are given in Table 4.3.

^{16}O(^{3}He, n)^{18}Ne.

Another reaction channel observed in this reaction was the ^{16}O(^{3}He, n)^{18}Ne, the level scheme is given in Fig. 4.18. The two transitions observed are the 1489.8 keV $4^+ \rightarrow 2^+$ and 1887.6 keV $2^+ \rightarrow 0^+$. The 1489.8 keV state has a relatively longer half-life ($t_{\frac{1}{2}} = 3.0$ ps) compared to the lower level state 1887.6 keV with a half-life, $t_{\frac{1}{2}} = 0.46$ ps. Their photo-peaks are labelled in blue colour in the spectrum, see Fig. 4.17. These states have possibly been excited through Coulomb or inelastic interactions of the beam with the target ^{16}O and/or the residual nucleus ^{18}Ne as these are $L > 0$ transfer. The peak 1887.6 keV has an asymmetric distribution, being broader to the left low energy tail end, possibly due to the *Doppler shift* of the peak. Clover detectors were placed at 90° and 135°, thus some γ rays decay from this 4^+ state as the target recoils, causing the shift in energy (to low energy) for the clover detectors at 135°. The 4^+ state also has a longer half-life. Some γ
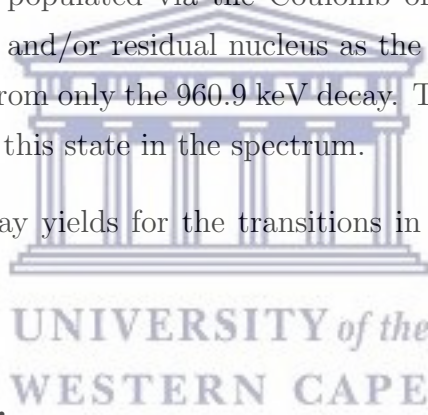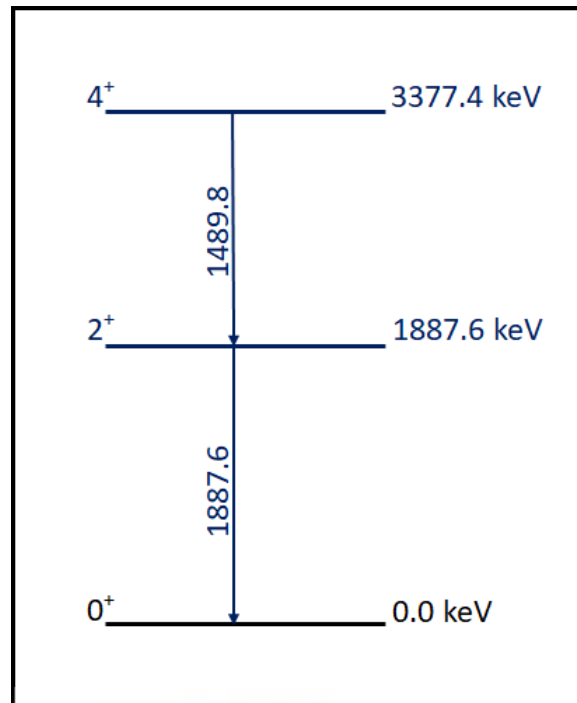
FIGURE 4.18: The level scheme of ^{18}Ne populated through the direct reaction channel, ^{16}O(^{3}He, n)^{18}Ne from the contamination of the target by oxygen.

ray events produced after the target recoil will not be energy shifted. Extracted γ ray yields in this channel are given in Table 4.3 (marked in asterisk).

Chapter 5

DISCUSSION

The (^{3}He, n) reactions allow the two protons to be added to the target nuclei and compliments the much more common experiments using two neutron transfer (t, p) and (p, t) reactions. It provides an important probe for the study of nuclear shell structure. The (^{3}He, n) direct reaction channel has a low cross-section compared to fusion-evaporation reactions. Its cross section is nearly 1000th of the main fusion evaporation channels making the experiments very challenging.

The Nuclei ^{110,112}Cd

A wide range of experimental probes have been used to study the cadmium nuclei over the years; the fusion evaporation reactions [39, 43–45, 92, 93], transfer and inelastic scattering reactions [94–102], β-decay [92, 93, 103–105] and (n, $n'\gamma$) reaction [106–114]. This has enabled the development of comprehensive level schemes of the stable Cd isotopes. The data here seek to complement these previous efforts by looking at the 2 proton parentage of the ^{110,112}Cd levels especially of the low-lying excited 0^+ states. The nature of these low-lying excited 0^+ states is key in determining the nature of collectivity that characterises this nucleus. The $B(E2)$ values for the decay excited 0^+ states to the one-phonon 2_1^+ state show some discrepancies. The $B(E2; 0^+ \rightarrow 2_1^+)$ values for the decay from 0_3^+ are extremely lower than expected for a possible two-phonon candidate. Instead, this state show enhanced $B(E2)$ decay values to one of its two-phonon 2_2^+ triplet members. However, for the intruder band head, the 0_2^+ show enhanced $E2$ decay strength to the one-phonon state. In all cases, the collective strength for the decay of an excited

87
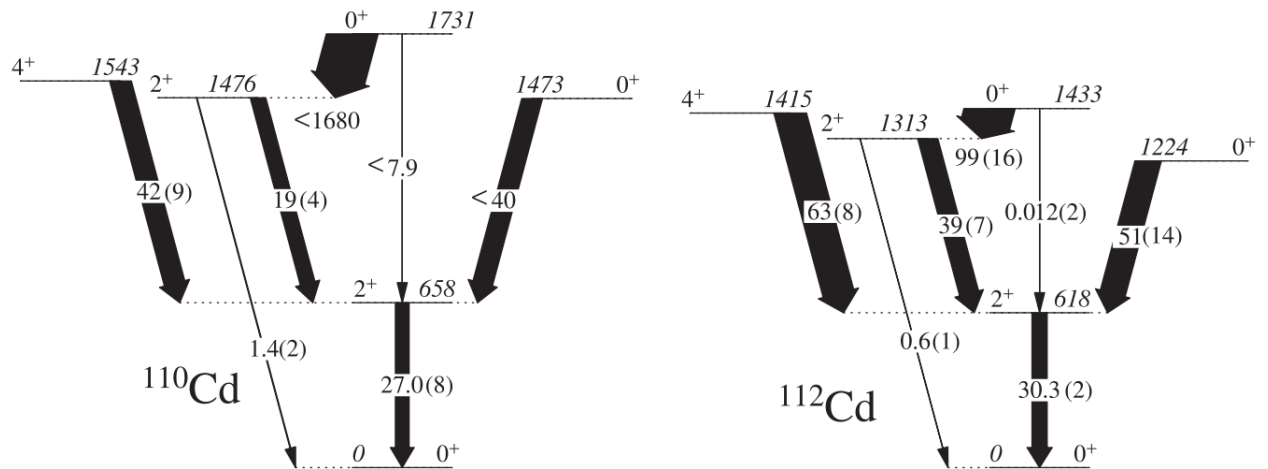
FIGURE 5.1: Low-lying levels in ^{110,112}Cd isotopes. The arrows represent $B(E2)$ transitions labelled in W.u. with the uncertainties given in parentheses [41, 42].

0^+ state to the one-phonon $2_1{}^+$ state appears to be concentrated in the intruder band head rather than the two-phonon $0_3{}^+$ state, see Fig. 5.1. It is these facts that have required further investigation of these states.

Previous data on the ^{110}Cd nucleus populated through the two-proton stripping (^{3}He, n) reaction was collected by Fielding *et al.* [2] using a 9 m time-of-flight baseline. About 5 excited 0^+ states were identified in that measurement albeit with poor energy resolution of greater than 400 keV, see Fig. 5.2. The 1440 keV 0^+ state should decay to the 656.5 keV 2^+ state, however there is no evidence of this peak in the spectrum. Unlike in Fielding's measurement, the ground-state transition cannot be populated in this measurement as it cannot decay by γ rays. Only the first excited 2^+ state at 656.5 keV has been populated in the present experiment, see Fig. 4.5. The positions of the peaks at 816.0 and 1074.0 keV, the first and second excited 0^+ states, respectively, have been indicated in the spectrum and it is clear that neither of these is present in this data. This is in direct contrast with Fielding's measurement which show strong strengths for the populated 0^+ state at 1.44 MeV. The 656.5 keV state populated is an $L = 2$ transfer, which shows relatively low strengths compared to the 1.44 MeV 0^+ in Fielding's measurement. If the two states were collective phonon states, the expectation is that the 2^+ (in our measurement) as the first phonon state would at least be comparable in terms of population strengths to the 2 phonon state in [2]. There are no high lying states observable in the data that would decay into this lower state. If the population of $2_1{}^+$ state is through the direct reaction process, it must be through the coupled

FIGURE 5.2: A time-of-flight spectrum from Fielding *et al.* [2], generated during the ^{108}Pd(^{3}He, n)^{110}Cd reaction.

channel method, as this is an $L = 2$ transfer prohibited by the selection rules for this experiment set-up.

Similarly, the ^{110}Pd(^{3}He, n)^{112}Cd direct reaction has populated only the 617.2 keV 2_1^+ state with even weaker strengths than the ^{110}Cd data. There are no high-lying peaks observable in the spectrum that would decay into this lower state. The only possible conclusion is that the population of this peak is through the same reaction mechanism as in the data of ^{110}Cd, which is an $L = 2$ transfer which possible take place through Coulomb or inelastic interaction of the ^{3}He beam with the target. In the previous ^{110}Pd(^{3}He, n)^{112}Cd measurement, also done by Fielding *et al.* [2], they populated 4 excited 0^+ states, see Fig. 5.3. There is no peak at 617.2 keV in those data. The 2 neutron transfer measurement, ^{110}Cd(t, p)^{112}Cd reaction done by Medsker *et al.* [115], they achieved high yields for the populated states. They populated about 5 low lying excited 0^+ states at 1223, 1431, 1873, 2640 and 2829 keV with most of them at fairly large population strengths. They did not observe the excited 0^+ at 2640 keV. The population of the 1223 keV state believed to be the possible candidate for the 2p-4h proton intruder band suggests the importance of mixing of the normal g.s. and intruder $^+0$ states in ^{112}Cd. The 617 keV 2^+ state in that measurement shows a relatively large population strength.

It is rather surprising that in both measurements, ^{108,110}Pd(^{3}He, n)^{110,112}Cd the
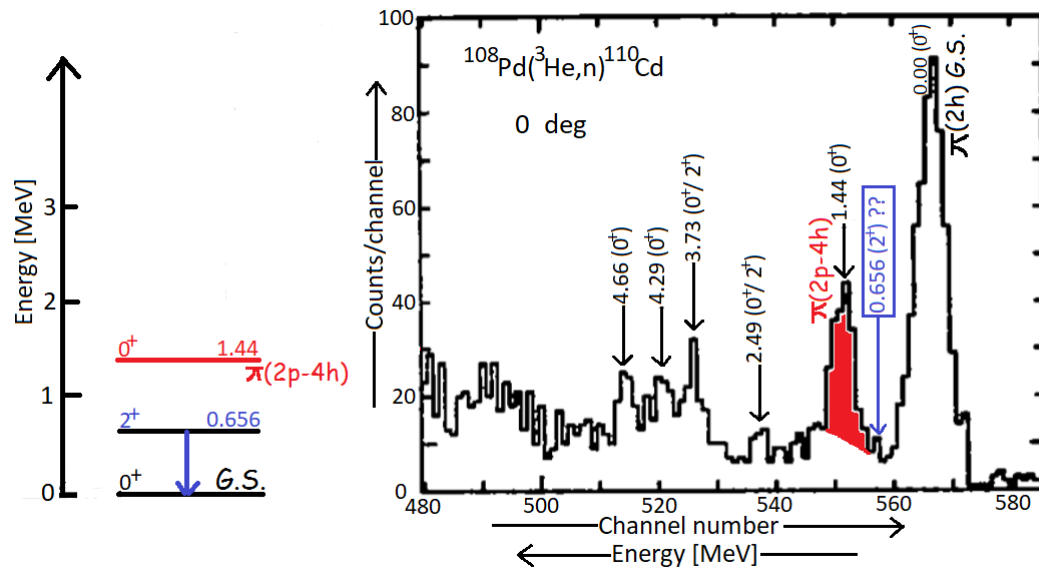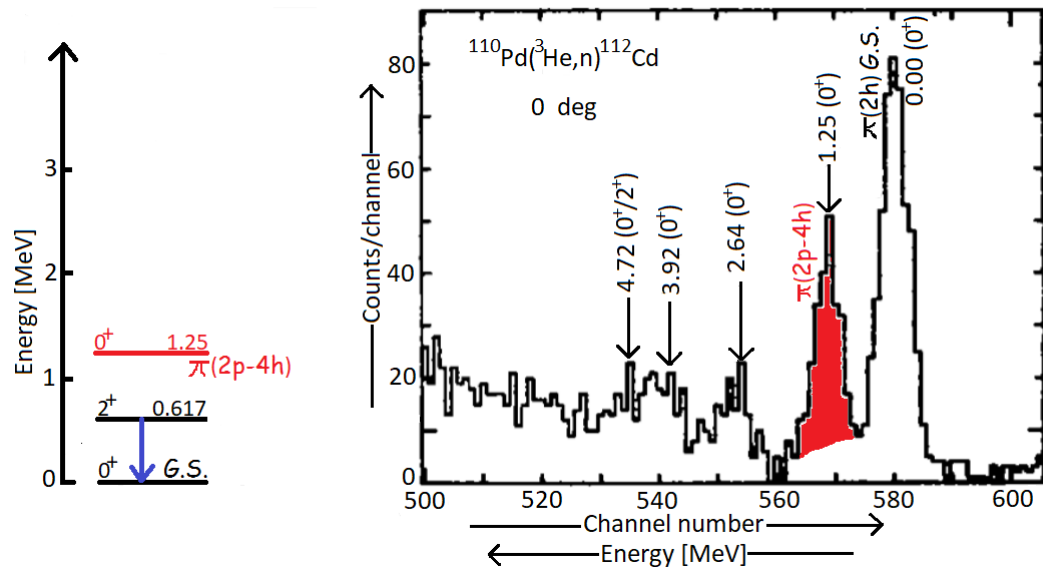
FIGURE 5.3: A time-of-flight spectrum from Fielding *et al.* [2] generated during the ^{110}Pd(^{3}He, n)^{112}Cd reaction.

excited 0^+ is not populated, especially the intruder states with a proton configuration of 2p-4h structure.

The Nucleus ^{116}Sn

The results obtained in this measurement show no states in the direct reaction channel of interest. It is possible that there were bad timing coincidence settings with the electronics. The 2-dimensional scatter plot, Fig. 4.10, shows no structure of the different centroids from the target, beam dump γ rays and the fusion evaporation neutrons.

The Nucleus ^{117}Sb

With the odd-spin target nucleus, all the transfer strength should go to the excited $\frac{9}{2}^+$ states, as the ground state of the residual nucleus has a different spin to that of the target nucleus in the direct reaction channel. Just as with the cadmium isotopes measurements, some states in this odd nucleus have been populated through $L > 0$ transfer. There are 5 states identified in the ^{115}In(^{3}He, n)^{117}Sb reaction channel with better yields relative to the even nuclei data measured here. The better energy resolution in this measurement has made it possible to resolve a number of states that could not possibly be distinguished in Alford's time-of-flight low-energy resolution experiment. The 374.0 keV γ ray peak that feeds the 1160.0 keV level has been clearly identified. The energy spacing between states, does indeed prove the assignment of this band as a deformed rotational band.

In the previous (^{3}He, n) reaction measurement for ^{117}Sb done by Alford *et al.* [3], they identified 3 excited $\frac{9}{2}^+$ states, see Fig. 5.4. In this measurement the 1160 keV state has been populated, however the other two $\frac{9}{2}^+$ states at 2280 and 3000 keV cannot be identified. The enhanced population of the deformed 2p-1h band head state at 1160 keV suggests that the wave function of the ground state of ^{115}In has a deformed component.
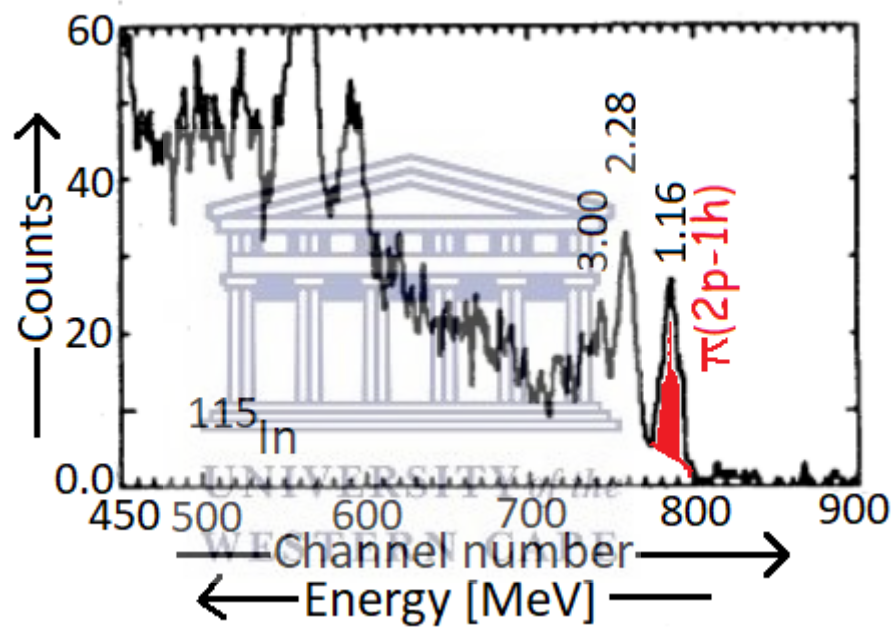
FIGURE 5.4: A time-of-flight spectrum from Alford *et al.* [3] generated during the ^{115}In(^{3}He, n)^{117}Sb reaction.

Chapter 6

CONCLUSIONS

All four of the experiments reported on here were carried out before I started on my Ph.D. My task has been to treat the raw data and analyse the outcomes. Further development of the liquid scintillator detector was stopped, as the results were not encouraging with low light output from the PMTs possible due to high attenuation of light by the scintillator material. Neither the shortening of the length of the detector cylinder made any significant improvements in the spectrum. A time-of-flight measurement using the (^{3}He, n) two-proton stripping reaction has been addressed by combining a high resolution γ ray spectrometer and coupling it with a neutron detector array placed at small angles less than 10%. The four series of measurements have been performed at iThemba LABS, some with good results produced from the measurement such as the data from ^{115}In(^{3}He, n)^{117}Sb reaction and also the data (of ^{29}P, ^{61}Cu, ^{162}Dy, ^{100}Ru and ^{150}Sm) from previous measurements [89, 116]. However, the ^{116}Sn data seems to have had timing problems with the electronics, as there appears to be no observed states in the direct reaction channel. Synchronization of the neutron and γ ray detectors is necessary in order to have a good time correlation of the events coming from the same reaction event in these measurements. Quite frequently, it is reported in the run-book that there were issues with the RF stability during the experiment, especially with the ^{114}Cd(^{3}He, n)^{116}Sn measurement.

The population of the $L = 2$ states in both even and odd target nuclei is confirmation that the ^{3}He beam is inelastically exciting the target nucleus. In the ^{110,112}Cd only the 2_1^+ states were populated with relatively low yields. With the odd target nucleus ^{115}In, spin $J = J_{target}$ have selectively been populated with

93

fairly high yields. The yields for each reaction have been extracted by measuring the peak areas of state populated. These type of measurements have challenges, the $n - \gamma$ discrimination ability still needs to be improved. Systematics of two-proton stripping reactions across the nuclear chart is still one of the areas not yet fully explored in nuclear physics. For future development, a proper neutron wall with better γ shielding is needed and also with an array of neutron detectors capable of $n - \gamma$ discrimination. This should also include upgraded flash ADCs with high sampling rates at 500 MHz.

References

[1] A. Bohr and B. Mottelson. *Nuclear Structure Volume II: Nuclear Deformations.* World Scientific Publishing Co, 1975.

[2] H. W. Fielding, R. E. Anderson, C. D. Zafiratos, D. A. Lind, F. E. Cecil, H. H. Wieman, and W. P. Alford. 0^+ states observed in Cd and Sn nuclei with the (^{3}He, n) reaction. *Nuclear Physics A*, 281:389–404, 1977.

[3] W. P. Alford, R. E. Anderson, R. A. Emigh, P. Craig, D. A. Lind, T. Masterson, J. Ullmann, and C. D. Zafiratos. Coupling of particles and holes with proton pairing vibrations near Z= 50. *Physical Review C*, 30(1):67–71, 1984.

[4] F. Corminboeuf, T. B. Brown, L. Genilloud, C. D. Hannant, J. Jolie, J. Kern, N. Warr, and S. W. Yates. Structures and lifetimes of states in ^{110}Cd. *Physical Review C*, 63(014305):1–11, 2000.

[5] A Savelius, S. Juutinen, K. Helariutta, P. Jones, R. Julin, P. Jämsen, M. Muikku, M. Piiparinen, J. Suhonen, S. Törmänen, R. Wyss, P. T. Greenlees, P. Simecek, and D. Cutoiu. Coexisting structures in ^{115}Sn and ^{116}Sn. *Nuclear Physics A*, 637:491–519, 1998.

[6] W. E. Burcham. *Nuclear Physics: An Introduction.* Longmans, 1963.

[7] L. Fortunato. Solutions of the Bohr Hamiltonian, a compendium. *The European Physical Journal A*, 26:1–30, 2005. doi: 10.1140/epjad/i2005-07-115-8.

[8] R. F. Casten. *Nuclear Structure from a Simple Perspective.* Oxford University Press, 2nd edition, 2000.

[9] Glenn F. Knoll. *Radiation Detection and Measurement.* Wiley, 2011.

[10] G. Duchene, F.A. Beck, P.J. Twin, G. De France, D. Curien, L. Han, C.W. Beausang, M.A. Bentley, P.J. Nolan, and J. Simpson. The Clover : a New

Generation of Composite Ge Detectors. *Nucl. Instrum. Meth. Phys. Res. A*, 432:90–110, 1999.

[11] W. H. Trzaska. "Recommended data on selected gamma-ray and conversion-electron calibration sources". *Nucl. Instrum. Meth. Phys. Res. A*, 297:223 – 229, 1990.

[12] C. W. Beausang and J. Simpson. Large arrays of escape suppressed spectrometers for nuclear structure experiments. *J. Phys. G: Nucl. Part. Phys.*, 22:527–558, 1996.

[13] Data extracted from the National Nuclear Data Center. URL `https://www.nndc.bnl.gov`.

[14] D. Evers, W. Assmann, K. Rudolph, S. J. Skorka, and P. Sperr. The (^{3}He, n) reaction on even (f, p) shell nuclei at 18 and 21 MeV (I). *Nuclear Physics A*, 198:268–288, 1972.

[15] D. Evers, W. Assmann, K. Rudolph, S. J. Skorka, and P. Sperr. The (^{3}He, n) reaction on even (f, p) shell nuclei at 15, 18, and 21 MeV (II). *Nuclear Physics A*, 230:109–140, 1974.

[16] W. P. Alford, R. A. Lindgren, D. Elmore, and R. N. Boyd. $J^\pi = 0^+$ states in the (fp) shell excited in the (^{3}He, n) reaction. *Nuclear Physics A*, 243: 269–297, 1975.

[17] H. W. Fielding, R. E. Anderson, D. A. Lind, C. D. Zafiratos, and W. P. Alford. Two-proton transfer near Z = 40. *Nuclear Physics A*, 269:125–137, 1976.

[18] W. P. Alford, R. E. Anderson, P. A. Batay-Csorba, D. A. Lind, H. H. Wieman, and C. D. Zafiratos. Structure of ^{88}Sr from the ^{86}Kr(^{3}He, n)^{88}Sr reaction. *Nuclear Physics A*, 293:83–91, 1977.

[19] D. Evers, C. Ley, E. Spindler, W. Assmann, K. Rudolph, P. Konrad, and P. Sperr. The (^{3}He, n) reaction on ^{16}O and ^{18}O. *Nuclear Physics A*, 275: 363–380, 1977.

[20] H. W. Fielding, R. E. Anderson, P. D. Kunz, D. A. Lind, C. D. Zafiratos, and W. P. Alford. A study of the (^{3}He, n) reaction on isotopes of tin. *Nuclear Physics A*, 304:520–532, 1978.

[21] W. P. Alford, R. E. Anderson, P. A. Batay-Csorba, R. A. Emigh, D. A. Lind, P. A. Smith, and C. D. Zafiratos. The (^{3}He, n) reaction on N = 82 targets and even isotopes of neodymium. *Nuclear Physics A*, 321:45–61, 1979.

[22] W. P. Alford, P. Craig, D. A. Lind, R. S. Raymond, J. Ullman, C. D. Zafiratos, and B. H. Wildenthal. Structure of ^{22}Mg, ^{26}Si, ^{34}Ar and ^{38}Ca via the (^{3}He, n) reaction. *Nuclear Physics A*, 457:317–336, 1986.

[23] A. Bohr, B. R. Mottelson, and D. Pines. Possible Analogy between the Excitation Spectra of Nuclei and Those of the Superconducting Metallic State. *Physical Review*, 110(4):936–938, 1958.

[24] Aager Bohr. *Mat. Fys. Medd. Dan. Vid. Selsk*, 26(14), 1952.

[25] A. Bohr and B. Mottelson. *Mat. Fys. Medd. Dan. Vid. Selsk*, 27(16), 1953.

[26] D. R. Bes and R. A. Broglia. Pairing vibrations. *Nuclear Physics A*, 80: 289–313, 1966.

[27] J L Wood. The ground states of $^{176-86}$Pt: an example of a shell model intruder state configuration. 1981. URL https://cds.cern.ch/record/878203.

[28] George Gamow. *Proc. Roy. Soc. of London A*, 136(386), 1929.

[29] Lord Rayleigh. *Proc. Roy. Soc. of London*, 29(71), 1879.

[30] Leon van Dommelen. Quantum Mechanics for Engineers. URL www.eng.fsu.edu/~dommelen/quantum/style_a/nt_liqdrop.html.

[31] C. F. von Weizacker. *Zeitschrift für Physik*, 96(420), 1935.

[32] S. Flügge. *Ann. Phys. Lpz.*, 431(373), 1941.

[33] J. Kern, P. E. Garrett, J. Jolie, and H. Lehmann. Search for nuclei exhibiting the U(5) dynamical symmetry. *Nuclear Physics A*, 593(1):21–47, 1995.

[34] K. Heyde, P. Van Isacker, M. Waroquier, G. Wens, and M. Sambataro. Description of the low-lying levels in ^{112,114}Cd. *Physical Review C*, 25(6): 3160–3177, 1982.

[35] K. Heyde and J. L. Wood. Shape coexistence in atomic nuclei. *Reviews of Modern Physics*, 83:1467–1521, 2011.
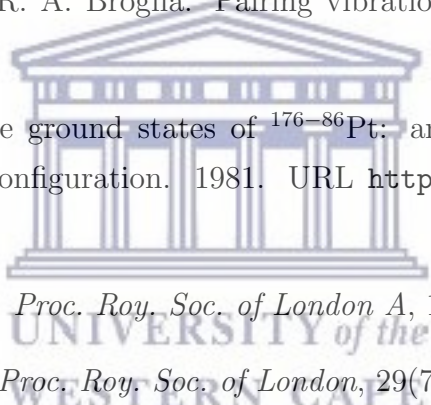
[36] K. Heyde, J. Jolie, J. Moreau, J. Ryckebusch, M. Waroquire, P. van Duppen, M. Huyse, and J. L. Wood. A Shell-Model Description of 0^+ Intruder States in Even-Even Nuclei. *Nuclear Physics A*, 466:189–226, 1987.

[37] J. L. Wood, K. Heyde, W. Nazarewicz, M. Huyse, and P. van Duppen. Coexistence in even-mass nuclei. *Physics Reports*, 215(3 & 4):101–201, 1992.

[38] R. A. Meyer and L. Peker. Evidence for the Coexistence of Shapes in Even-Mass Cd Nuclei. *Zeitschrift für Physik A*, 283:379–382, 1977.

[39] J. Kern, A. Bruder, S. Drissi, V. A. Ionescu, and D. Kusnezov. Study of ^{110}Cd by the ^{108}Pd(α, 2nγ) reaction. *Nuclear Physics A*, 512:1–45, 1990.

[40] P. E. Garrett, K. L. Green, and J. L. Wood. Breakdown of Vibrational motion in the isotopes $^{110-116}$Cd. *Physical Review C*, 78(044307):1–17, 2008.

[41] K. L. Green, P. E. Garrett, A. E. Austin, G. C. Ball, D. S. Bandyopadhyay, S. Colosimo, D. Cross, G. A. Demand, G. F. Grinyer, G. Hackman, W. D. Kulp, K. G. Leach, A. C. Morton, C. J. Pearson, A. A. Phillips, M. A. Schumaker, C. E. Svensson, J. Wong, J. L. Wood, and S. W. Yates. Degeneracy at 1871 keV in ^{112}Cd and implications for neutrinoless double electron capture. *Physical Review C*, 80(032502(R)):1–5, 2009.

[42] P. E. Garrett, J. Bangay, A. Diaz Varela, G. C. Ball, D. S. Cross, G. A. Demand, P. Finlay, A. B. Garnsworthy, K. L. Green, G. Hackman, C. D. Hannant, B. Jigmeddorj, J. Jolie, W. D. Kulp, K. G. Leach, J. N. Orce, A. A. Phillips, A. J. Radich, E. T. Rand, M. A. Schumaker, C. E. Svensson, C. Sumithrarachchi, S. Triambak, N. Warr, J. Wong, J. L. Wood, and S. W. Yates. Detailed spectroscopy of ^{110}Cd: Evidence for weak mixing and the emergence of γ-soft behavior. *Physical Review C*, 86(044304):1–9, 2012.

[43] J. Kumpulainen, R. Julin, J. Kantele, W. H. Passoja, Trzaska, E. Verho, J. Väärämäki, D. Cutoiu, and M. Ivascu. Systematic study of low-spin states in even Cd nuclei. *Physical Review C*, 45(640):640–661, 1992.

[44] M. Deleze, S. Drissi, J. Kern, P. A. Tercier, J. P. Vorlet, J. Rikovska, T. Otsuka, S. Judge, and A. Williams. Systematic study of the mixed ground-state and "intruder" in ^{110,112,114}Cd. *Nuclear Physics A*, 551:269–294, 1993.

[45] M. Deleze, S. Drissi, J. Jolie, J. Kern, and J. P. Vorlet. The ^{112}Cd nucleus: A laboratory for the study of collective excitations. *Nuclear Physics A*, 554: 1–44, 1993.

[46] J. Bron, W. H. A. Hesselink, A. van Poelgeest, J. J. A. Zalmistra, M. J. Uitzungler, H. Verheul, K. Heyde, M. Waroquier, H. Vincx, and P. van Isacker. Collective Bands in Even Mass Sn Isotopes. *Nuclear Physics A*, 318:335–351, 1979.

[47] A. Bäcklin, N. G. Jonsson, R. Julin, M. Kantele, J. Luontama, A. Passoja, and T. Poikolainen. 0^+ States and E0 and E2 Transition Rates in Even Sn Nuclei. 351:490–508, 1981.

[48] N. G. Jonsson, A. Bäcklin, J. Kantele, R. Julin, M. Luontama, and A. Passoja. Collective States in Even Sn Nuclei. *Nuclear Physics A*, 371:333–348, 1981.

[49] P. Van Isacker, M. Waroquier, H. Vincx, and K. Heyde. The $J^\pi = \frac{9}{2}^+$ Bands in Odd-Mass Sb and I Isotopes: Evidence for Deformed States? *Nuclear Physics A*, 292:125 − 143, 1977.

[50] R. E. Shroy, A. K. Gaigalas, G. Schatz, and D. B. Fossan. High-spin states in odd-mass $^{113-119}$Sb: $\Delta j = 1$ bands on $\frac{9}{2}^+$ proton-hole states. *Physical Review C*, 19(4):1324–1343, 1979.

[51] J. M. Blatt and V. F. Weisskopf. *Theoretical Nuclear Physics*. John-Wiley & Sons, 1958.

[52] K. S. Krane. *Introductory Nuclear Physics*. John-Wiley & Sons, 1988.

[53] R. Woods and D. S. Saxon. Diffuse Surface Optical Model for Nucleon-Nuclei Scattering. *Physical Review*, 95:577–578, 1954.

[54] M. G. Mayer. Nuclear Configuration in the Spin-Orbit Coupling Model. I. Empirical Evidence. *Physical Review*, 78(1):16–21, 1950.

[55] O. Haxel, H. D. Jensen, and H. E. Suess. On the "Magic Numbers" in nuclear structure. *Physical Review*, 75(1766), 1949.

[56] M. G. Mayer. Nuclear Configuration in the Spin-Orbit Coupling Model.II.Theoretical Considerations. *Physical Review*, 78(1):22–23, 1950.

[57] K. Alder, A. Bohr, T. Huus, B. Mottelson, and A. Winther. Study of Nuclear Structure by Electromagnetic Excitation with Accelerated Ions. *Reviews of Modern Physics*, 28(4), 1956.

[58] S. G. Nilsson and I. Ragnarsson. *Shapes and Shells in Nuclear Structure.* Cambrdge University Press., 1st edition, 1995.

[59] A. Bohr and B. R. Mottelson. Rotational States in Even-Even Nuclei. *Physical Review*, 90:717–719, 1953.

[60] A. Bohr and B. R. Mottelson. Interpretation of Isomeric Transitions of Electric Quadrupole Type. *Physical Review*, 89:316–317, 1953.

[61] P. Ring and P. Schuck. *The Nuclear Many-Body Problem.* Springer-Verlag, New York, 1980.

[62] Pierre Marmier and Eric Sheldon. *Physics of Nuclei and Particles*, volume I. Academic press, inc., 1969.

[63] V. F. Weisskopf. Radiative Transition Probabilities in Nuclei. *Physical Review*, 83:1073, 1951.

[64] A. Bohr. Pair correlations nuclei and double transfer reactions. In *Nuclear Structure Dubna Symposium*, pages 179–189. IAEA, 1968.

[65] J. Bardeen, L. N. Cooper, and J. R. Schrieffer. Theory of superconductivity. *Physical Review*, 108(5):1175–1204, 1957.

[66] J. D. Rowe and J. L. Wood. *Fundamentals of Nuclear Models.* World Scientific, 2010.

[67] J. L. Wood, E. F. Zganjar, C. D. Coster, and K. Heyde. Electric monopole transitions from low energy excitations in nuclei. *Nuclear Physics A*, 651: 323–368, 1999.

[68] Norman Austern. *Direct Nuclear Reaction Theories*, volume XXV. John Wiley & Sons, 1970.

[69] S. T. Butler. On Angular Distributions from (d, p) and (d, n) Nuclear Reactions. *Physical Review*, 80(6):559–579, 1950.

[70] H. B. Burrows, W. M. Gibson, and J. Rotblat. Angular Distributions of Protons from the Reaction O^{16}(d, p)O^{17}. *Physical Review*, 80(6):1095, 1950.

[71] Norman K. Glendenning. *Direct Nuclear Reactions*. Academic press, inc., 1983.

[72] N. K. Glendenning. Nuclear Spectroscopy with Two-Nucleon Transfer Reactions. *Physical Review*, 137(1B):102–113, 1965.

[73] N. K. Glendenning. The Two-Nucleon Stripping Reaction. *Nuclear Physics*, 29:109–119, 1962.

[74] J. M. Bang, F. G. Gareev, W. T. Pinkston, and J. S. Vaagen. One- and two-nucleon overlap functions in nuclear physics. *Physics Reports*, 125(6): 253–399, 1985.

[75] S. T. Butler, N. Austern, and C. Pearson. Semiclassical Treatment of Direct Nuclear Reactions. *Physical Review*, 114(4):1227–1238, 1958.

[76] H. Feshbach. *Theoretical Nuclear Physics: Nuclear Reactions*. John-Wiley & Sons, 1992.

[77] Shiro Yoshida. Note on the Two-Nucleon Stripping Reaction. *Nuclear Physics*, 33:685 – 692, 1962.

[78] P. E. Hodgson. The Deuteron-Nucleus Optical Potential. *Advances in Physics*, 15(59), 1966.

[79] H. Feshbach, C. E. Porter, and V. F. Weisskopf. The formation of a compound nucleus in neutron reactions. *Physical Review*, 90:166–167, 1953.

[80] D. Y. Pang, P. Roussel-Chomaz, H. Savajols, R. L. Varner, and R. Wolski. Global optical model potential for A= 3 projectiles. *Physical Review C*, 79 (024615):1–21, 2009.

[81] G. R. Satchler. The Distorted-Waves Theory of Direct Nuclear Reactions with Spin-Orbit Effects. *Nuclear Physics*, 55:1–33, 1964.

[82] I. S. Towner and J. C. Hardy. Direct two-nucleon transfer reactions and their interpretation in terms of the nuclear shell model. *Advances in Physics*, 18 (401):401–488, 1969.

[83] R. J. Ascuitto and N. K. Glandenning. Inelastic Processes in Particle Transfer Reactions. *Physical Review*, 181(4):1396–1403, 1969.

[84] N. Bohr. Neutron Capture and Nuclear Constitution. *Nature*, 137(344): 344–348, 1936.

[85] R. T. Newman, J. J. Lawrie, B. R. S. Babu, M. S. Fetea, S. V. Fortsch, S. Naguleswaran, J. V. Pilcher, D. A. Raave, C. Rigollet, J. F. Sharpey-Schafer, C. J. Stevens, F. D. Smit, G. F. Steyn, C. V. Wikner, D. G. Aschman, R. Beetge, R. W. Fearick, G. K. Mabala, S. Murray, D. G. Roux, W. Whittacker, and N. J. Ncapayi. High-spin studies with the AFRODITE array. *Balkan Physics Letters*, Special Issue:182–190, 1998.

[86] Jeng-Wei Lin, Yen-Fu Chen, Rong-jiun Sheu, and Shiang-Huei Jiang. Measurement of angular distribution of cosmic-ray muon fluence rate. *Nucl. Instrum. Meth. Phys. Res. A*, 619:24–27, 2010.

[87] Ronald Edler. Cocktails for Liquid Scintillation Counting. Technical report, Perkin-Elmer Inc., 2015. URL `https://www.perkinelmer.com/lab-solutions/resources/docs/APP_Cocktails-for-Liquid-Scintillation-Counting-011940_01.pdf`.

[88] D. C. Radford. URL `http://radware.phy.ornl.gov/rw/esclev/esclev.html`.

[89] J. F. Sharpey-Schafer, P. Papka, P. M. Jones, P. Vymers, R. A. Bark, T. D. Bucher, S. P. Bvumbi, T. S. Dinoko, J. L. Easton, M. S. Herbert, B. V. Kheswa, E. A. M. A. Khaleel, N. Khumalo, E. A. Lawrie, J. J. Lawrie, S. N. T. Majola, J. Ndayishimye, M. R. Nchodu, D. Negi, S. P. Noncolela, J. N. Orce, O. Shirinda, P. Sithole, and M. Wiedeking. Coulomb and Inelastic Excitations of Target Nuclei in In (^{3}He, n) Two Proton Stripping Reactions on ^{27}Al, ^{59}Co, ^{48}Nd and ^{160}Gd. In *Proceedings Of Science*. 52 International Winter Meeting On Nuclear Physics (Bormio2014), 2014.

[90] D. LaFosse, D. B. Fossan, J. R. Hughes, Y. Liang, P. Vaska, M. P. Waring, and J. y Zhang. New Deformed States near the Z = 50 Closed Shell: ^{117}Sb$_{66}$. *Physical Review Letters*, 69(9):1332–1335, 1992.

[91] D. R. LaFosse, D. B. Fossan, J. R. Hughes, Y. Liang, H. Schnare, P. Vaska, M. P. Waring, and J. -j. Zhang. Particle-hole induced intruder bands in ^{117}Sb and ^{119}Sb. *Physical Review C*, 56(2):760–771, 1997.

[92] A. Gade, J. Jolie, and P von Brentano. First observation of the intruder band in ^{108}Cd. *Physical Review C*, 65(041305):1–5, 2002.

[93] A. Gade, A. Fitzler, C. Fransen, J. Jolie, S. Kasemann, H. Klein, A. Linnemann, V. Werner, and P. von Brentano. Reaction states of ^{108}Cd: Investigation with complementary $\gamma\gamma$-spectroscopic methods. *Physical Review C*, 66(034311):1–26, 2002.

[94] Mashiro Koike. Elastic and inelastic scattering of 14 MeV protons from ^{111}Cd, ^{112}Cd and ^{113}Cd. *Nuclear Physics A*, 98:209–227, 1967.

[95] Masahiro Koike, Itaru Nonaka, Jun Kokame, Hiromichi Kamitsubo, Yohko Awaya, Takeshi Wada, and Hitoshi Nakamura. Collective states of ^{110}Cd, ^{114}Cd and ^{116}Cd excited in inelastic scattering of 55 MeV protons. *Nuclear Physics A*, 125:161–170, 1969.

[96] M. Pignanelli, S. Micheletti, E. Cereda, M. N. Harakeh, S. Y. van der Werf, and R. de Leo. Proton scattering on ^{100}Mo and ^{112}Cd and the interacting boson approximation. *Physical Review C*, 29(2):434–440, 1984.

[97] R. De Leo, N. Blasi, S. Micheletti, M. Pignanelli, W. T. A. Borghols, J. M. Schippers, S. Y. van der Werf, G. Maino, and M. N. Harakeh. Multipole strength distribution in ^{112}Cd. *Nuclear Physics A*, 504:109–129, 1989.

[98] N. Blasi, S. Micheletti, M. Pignanelli, R. de Leo, R. Hertenberger, F. J. Eckle, H. Kader, P. Schiemenz, and G. Graw. Study of ^{112}Cd via the ^{113}Cd($\vec{d}$, t) reaction. *Nuclear Physics A*, 511:251–268, 1990.

[99] M. Pignanelli, N. Blasi, S. Micheletti, R. De Leo, M. A. Hofstee, J. M. Schippers, S. Y. van der Werf, and M. N. Harakeh. Octupole excitations in vibrational nuclei and *sdf* interacting boson model. *Nuclear Physics A*, 519: 567–601, 1990.

[100] M. Pignanelli, N. Blasi, S. Micheletti, R. De Leo, L. LaGamba, R. Perrino, J. A. Bordewijk, M. A. Hofstee, J. M. Schippers, S. Y. van der Werf, J. Wesseling, and M. N. Harakeh. Hexadecapole strength distributions of vibrational nuclei in the A = 100 mass region. *Nuclear Physics A*, 540:27–56, 1992.

[101] N. Blasi, S. Micheletti, M. Pignanelli, R. De Leo, R. Hertenberger, M. Bisemberger, D. Hofer, H. Kader, P. Schiemenz, and G. Graw. Study of ^{110}Cd via the ^{111}Cd($\vec{d}$, t) reaction. *Nuclear Physics A*, 536:1–19, 1992.

[102] R. Hertenberger, G. Eckle, F. J. Eckle, G. Graw, D. Hofer, H. Kader, P. Schiemenz, Gh. Cata-Danil, C. Hategan, N. Fujiwara, K. Hosono, M. Kondo, M. Matsuoka, T. Noro, T. Saito, S. Kato, S. Matsuki, N. Blasi, S. Micheletti, and R. de Leo. Study of ^{112}Cd via high-resolution $(\vec{d}, \vec{d'})$ and $(\vec{p}, \vec{p'})$ reactions and IBA model calculations. *Nuclear Physics A*, 574: 414–452, 1994.

[103] M. Bertschy, S Drissi, P. E. Garrett, J. Jolie, J. Kern, S. J. Mannanal, J. P. Vorlet, N. Warr, and J. Suhonen. Study of ^{110}Cd from the ^{110}In^{m} β decay. *Physical Review C*, 51(1):103–114, 1995.

[104] Youbao. Wang, P. Dendooven, J. Huikari, A. Jokinen, V. S. Kolhinen, G. Lhersonneau, A. Nieminen, S. Nummela, H. Penttilä, K. Peräjärvi, S. Rinta-Antila, J. Szerypo, J. C. Wang, and J. Äystö. β decay of ^{116}Ag^{m} and the Vibrational Structure of ^{116}Cd. *Physical Review C*, 64(054315):1–8, 2001.

[105] Y. Wang, S. Rinta-Antila, P. Dendooven, J. Huikari, A. Jokinen, V. S. Kolhinen, G. Lhersonneau, A. Nieminen, S. Nummela, H. Penttilä, K. Peräjärvi, J. Szerypo, J. C. Wang, and J. Äystö. β decay of neutron-rich ^{118}Ag and ^{120}Ag isotopes. *Physical Review C*, 67(064303):1–12, 2003.

[106] P. E. Garrett, H. Lehmann, C. A. McGrath, Minfang Yeh, and S. W. Yates. First observation of mixed-symmetry states in a good U(5) nucleus. *Physical Review C*, 54(5):2259–2263, 1996.

[107] P. E. Garrett, H. Lehmann, J. Jolie, C. A. McGrath, M. Yeh, and S. W. Yates. Quadrupole-octupole coupled states in ^{112}Cd. *Physical Review C*, 59 (5):2455–2461, 1999.

[108] P. E. Garrett, K. L. Green, H. Lehmann, J. Jolie, C. A. MacGrath, M. Yeh, and S. W. Yates. Properties of ^{112}Cd from the (n, n'γ) reaction: Lifetimes and transition rates. *Physical Review C*, 75(054310):1–26, 2007.

[109] F. Corminboeuf, T. B. Brown, L. Genilloud, C. D. Hannant, J. Jolie, J. Kern, N. Warr, and S. W. Yates. Characterization of Three-Phonon States in ^{110}Cd. *Physical Review Letters*, 84(18):4060–4063, 2000.

[110] F. Corminboeuf, T. B. Brown, L. Genilloud, C. D. Hannant, J. Jolie, J. Kern, N. Warr, and S. W. Yates. Structures and lifetimes of states in ^{110}Cd. *Physical Review C*, 63(014305):1–11, 2000.

[111] H. Lehmann, P. E. Garrett, J. Jolie, C. A. MacGrath, M. Yeh, and S. W. Yates. On the nature of "three-phonon" excitations in ^{112}Cd. *Physics Letters B*, 387:259–265, 1996.

[112] P. E. Garrett, H. Lehmann, J. Jolie, C. A. MacGrath, Yeh Minfang, W. Younes, and S. W. Yates. Properties of ^{112}Cd from the (n, n′γ) reaction: Levels and level densities. *Physical Review C*, 64(024316):1–27, 2001.

[113] D. Bandyopadhyay, S. R. Lesher, C. Fransen, N. Boukharouba, P. E. Garrett, K. L. Green, M. T. McEllistrem, and S. W. Yates. Investigation of phonon excitations in ^{114}Cd with the (n, n′γ) reaction. *Physical Review C*, 76(054308):1–22, 2007.

[114] M. Kadi, N. Warr, P. E. Garrett, J. Jolie, and S. W. Yates. Vibrational and intruder structures in ^{116}Cd. *Physical Review C*, 68(031306):1–4, 2003.

[115] L. R. Medsker, H. T. Fortune, J. D. Zumbro, C. P. Browne, and J. F. Mateja. ^{112}Cd from ^{110}Cd(t, p). *Physical Review C*, 36(5):1785–1791, 1987.

[116] P. Papka, E. A. M. A. Khaleel, P. Vymers, T. S. Dinoko, W. A. Richter, J. F. Sharpey-Schafer, P. M. Jones, E. A. Lawrie, J. J. Lawrie, S. N. T. Majola, O. Shirinda, M. Wiedeking, M. A. Stankiewicz, and B. A. Brown. High Resolution (^{3}He, n) Two Proton Stripping Reaction to 0^{+} States Populated in 2β Decay. In *Proceedings Of Science*. 51 International Winter Meeting On Nuclear Physics (Bormio2013)038, 2013.